Universität Stuttgart

Institut für Wasser- und Umweltsystemmodellierung

Mitteilungen

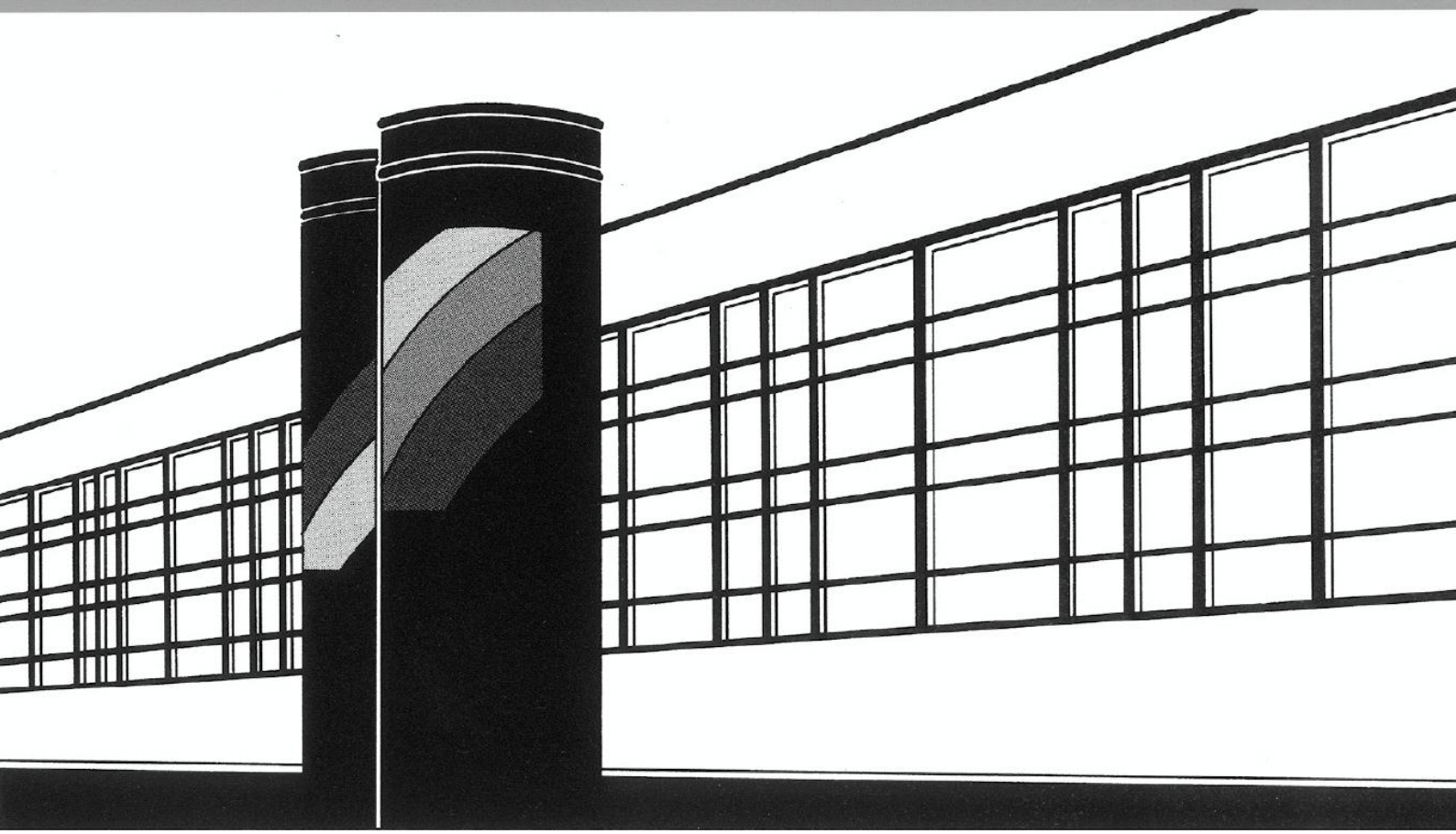

Heft 216 Thomas Pfaff

Processing and Analysis of Weather Radar Data for Use in Hydrology

Processing and Analysis of Weather Radar Data for Use in Hydrology

von der Fakultät Bau- und Umweltingenieurwissenschaften der
Universität Stuttgart zur Erlangung der Würde eines
Doktor-Ingenieurs (Dr.-Ing.) genehmigte Abhandlung

vorgelegt von

Thomas Pfaff
aus Würzburg

Hauptberichter:	Prof. Dr. rer.nat. Dr.-Ing. András Bárdossy
Mitberichter:	Prof. Geoffrey G.S. Pegram, PhD (Lancs), PrEng

Tag der mündlichen Prüfung: 17. Oktober 2012

Institut für Wasser- und Umweltsystemmodellierung
der Universität Stuttgart
2013

Heft 216

Processing and Analysis of Weather Radar Data for Use in Hydrology

von
Dr.-Ing.
Thomas Pfaff

Eigenverlag des Instituts für Wasser- und Umweltsystemmodellierung
der Universität Stuttgart

D93 Processing and Analysis of Weather Radar Data for Use in Hydrology

Bibliografische Information der Deutschen Nationalbibliothek
Die Deutsche Nationalbibliothek verzeichnet diese Publikation in der Deutschen Nationalbibliografie; detaillierte bibliografische Daten sind im Internet über http://www.d-nb.de abrufbar

Pfaff, Thomas:
Processing and Analysis of Weather Radar Data for Use in Hydrology von Thomas Pfaff. Institut für Wasser- und Umweltsystemmodellierung, Universität Stuttgart. - Stuttgart: Institut für Wasser- und Umweltsystemmodellierung, 2013

(Mitteilungen Institut für Wasser- und Umweltsystemmodellierung, Universität Stuttgart: H. 216)
Zugl.: Stuttgart, Univ., Diss., 2013
ISBN 978-3-942036-20-7
NE: Institut für Wasser- und Umweltsystemmodellierung <Stuttgart>: Mitteilungen

Herausgegeben 2013 vom Eigenverlag des Instituts für Wasser- und Umwelt-systemmodellierung

Druck: Document Center S. Kästl, Ostfildern

In Loving Memory

Fridolin Eich

Acknowledgements

First and foremost, I would like to thank Prof. András Bárdossy for the many great things I learned from him, and for his allowing me the utmost freedom to investigate other areas of the hydro-meteorological sciences that I deemed interesting or necessary.
I am also very grateful to Prof. Geoffrey G.S. Pegram for being my second doctoral advisor. His critical, yet always encouraging feedback made the writing process infinitely more pleasant. His advice on the broader subject of just getting research done will be valuable beyond the completion of this thesis.

Above and beyond all the colleagues at the department of hydrology and geohydrology, to whom I am grateful for a friendly and inspiring atmosphere, I would like to additionally highlight a select few:
Claus Haslauer inevitably introduced me to the business of Copulas. His enthusiasm inspired several initially just-for-fun projects, which turned out to become central parts of this thesis.
Ferdinand Beck has been a dependable companion the whole time through. I will always be grateful for the experiences of great team work during the side projects we faced together.
I count myself lucky to have found a true friend in Jochen Seidel whose unswerving cheerfulness together with his never failing motivation to tackle some climbing routes each week helped me keep mind and body in good enough shape to face the challenges necessary to complete this thesis.

Another special set of thanks goes to Maik Heistermann and Stephan Jacobi. Working together with them on matters of radar data correction exceeding our common project, has been an enjoyable and motivating experience.
Mario Böhm and Ingo Haag share my gratitude for encouraging me to start his journey and for their continuous support along the way.

Especially during the less joyful times associated with thesis work, the support of my family and especially my wife Viki has been invaluable beyond words.

Contents

List of Figures

List of Tables

List of Abbreviations

Abbreviation	Meaning
BMBF	German Federal Ministry for Education and Research (Bundesministerium für Bildung und Forschung)
CCI	Censored Copula Interpolation
CCID	Censored Copula Interpolation with Drift (derived from radar data)
DWD	German Meteorological Service (Deutscher Wetterdienst)
DX	Raw Radar Reflectivity product for individual radar sites; 5 minute temporal resolution, polar representation, variable elevations for each azimuth following the radar horizon; published by the DWD
EDK	Kriging with External Drift
MAE	Mean Absolute Error
MAD	Mean Absolute Difference
m.a.s.l.	meters above sea level
NWP	Numerical Weather Prediction
OK	Ordinary Kriging
PIA	Path Integrated Attenuation
ReV	Regionalized Variable
RMSE	Root Mean Squared Error
RMSD	Root Mean Squared Difference
QPE	Quantitative Precipitation Estimation
QPF	Quantitative Precipitation Forecast
QQ	Quantile-Quantile (transformation)
RY	German Composite Radar Rainfall product including basic data correction; 5 minute temporal resolution, spatial resolution 1x1 km^2; published by the DWD

List of Symbols

Symbol	Definition	Unit
A_e	effective antenna cross section	$[m^2]$
A_t	area of a scatterer	$[m^2]$
a	electrical size	[-]
α	linear parameter in reflectivity-attenuation relations	[dB/km]
b	slope parameter of linear regression	[-]
β	exponent parameter in reflectivity-attenuation relations	[-]
C	Copula	
c	covariance function	
D	drop diameter	[mm]
δ	slope change	[-]
G	radar antenna gain	[-]
γ	semivariogram	
h	separation distance	[m]
h_k	k-th iteration of displacement estimate of Lucas & Kanade algorithm	[m]
I	pixel brightness intensity	[-]
k	attenuation	[dB/km]
L	likelihood function	
λ	wavelength	[m]
λ_s	smoothing parameter constraint for Horn & Schunck optical flow algorithm	[-]
m	complex index of refraction	[-]
μ	Mean value	
P_r	radar returned power	[W]
P_t	radar transmitted power	[W]
Φ	cumulative distribution function of the normal distribution	[-]
ϕ	azimuth angle (0 at north, positive clockwise)	[-]
ϕ_Σ	density of a multivariate normal distribution function with correlation matrix Σ	[-]
R	Rain rate	[mm/h]
r	slant range from radar site	[m]
ρ	Pearson correlation coefficient	[-]
Σ	correlation matrix	
σ	scattering cross section	$[m^2]$
τ	travel time	[s]

Symbol	Definition	Unit
θ	elevation angle (0 at horizontal, positive upward)	[-]
V_m	illuminated volume	$[m^3]$
v	velocity in	[m/s]
Z	radar reflectivity factor	$[mm^6/m^3]$
Z_a	apparent radar reflectivity factor	$[mm^6/m^3]$
$Z(x)$	value of regionalized variable at location x	
$z(x_i)$	observed value at location x_i	

Zusammenfassung

Motivation

Mit dem Beginn der Forschungen zur meteorologischen Nutzung von Radar, entstand die Hoffnung zukünftig mit einem Netzwerk weniger Radarstationen, über weite Gebiete hinweg kontinuierlich in hoher zeitlicher und räumlicher Auflösung Niederschlag messen zu können. Qualitativ ist dieses Ziel sicherlich schon seit einiger Zeit erreicht, wie sich z. B. daran erkennen lässt, dass der Link zum "Wetterradar" mit einem animierten Verlauf der letzten Stunden und neuerdings auch einfachen Vorhersagen, zum Standardrepertoire heutiger Wetterwebseiten gehört[1].

Quantitativ zeigt sich eher noch ein gemischtes Bild. Obwohl Wetterradardaten bereits routinemäßig von den Wetterdiensten genutzt werden, um die Vorhersagequalität der numerischen Wettermodelle zu verbessern, fristet die Anwendung des hochaufgelösten, flächendeckenden Niederschlagsinputs in der hydrologischen Modellierung in Deutschland weiterhin ein Schattendasein, das über Forschungsprojekte und gelegentliche, kleinräumige Anwendung nach einem Extremereignis nicht hinauskommt.

Grund hierfür sind zum einen die teils gravierenden systematischen Fehler in der Radarmessung, von denen hier nur einige aufgezählt werden sollen:

- Überschätzungen durch nichtmeteorologische Echos (sog. Clutter)
- Fehlschätzungen durch die Messgeometrie des Radars
  - Überschätzungen im Bereich der Schmelzschicht in weiträumigen Niederschlagsfeldern
  - Unterschätzungen in den Randbereichen durch ein zu großes Messvolumen mit zusätzlichen Effekten durch Schnee in hohen Luftschichten
- Unterschätzungen durch Dämpfung bei intensiven Niederschlagsereignissen.

Zum anderen, finden sich in der aktuellen Literatur Indizien dafür, dass die Kalibration konzeptioneller hydrologischer Modellen nicht nur gebiets- sondern immer auch inputspezifisch ist (Bárdossy and Das, 2008; Cole and Moore, 2008), und es somit sehr wahrscheinlich ist, dass ein Modell, das normalerweise mit interpolierten Bodenniederschlagsdaten betrieben wird und hierauf kalibriert wurde, schlechtere Ergebnisse liefert, wenn dieser Niederschlagsinput durch Wetterradardaten ersetzt wird (Heistermann and Kneis, 2011).

Neben der deterministischen Korrektur der oben genannten Fehler, existieren auch seit einiger Zeit eher pragmatische Ansätze zur Korrektur von Wetterradardaten durch Aneichung an die Werte von Bodenniederschlagsmessungen. Die einfachsten

[1] z. B. http://www.meteox.de, Stand 11.09.2012

Ansätze hierzu korrigieren das gesamte Radarbild mit einem Faktor, der sich aus der mittleren Abweichung der Radarmessungen über den Bodenstationen vom dort gemessenen Niederschlag berechnet. Komplexere Methoden interpolieren entweder Korrekturfaktoren, die durch den Vergleich von Radar und Bodenmessung an Stationen gewonnen wurden (z. B. Brandes (1975)), Stationsdaten unter Hinzunahme der Radarinformation (Velasco-Forero et al., 2009), oder verbinden Stationsinterpolation und Radarfeld auf andere Weise (Ehret, 2003; Todini, 2001), um die räumliche Variabilität aus der Radarmessung zu erhalten, gleichzeitig aber das Feld auf die langfristig als korrekt erachtete Bodenmessung zu korrigieren.

In der vorliegenden Arbeit wurden Untersuchungen zu diesen drei Themengebieten, deterministische Datenkorrektur, Stationsaneichung und hydrologische Auswirkungen durchgeführt, deren Ergebnisse im folgenden kurz zusammengefasst werden sollen.

Deterministische Datenkorrektur

Clutterkorrektur

Nichtmeteorologische Echos stellen eine der größten Fehlerquellen in der quantitativen Niederschlagsschätzung durch Wetterradar dar. Unkorrigiert können die großen Reflektivitäten, die durch die Interaktion des Radarstrahls mit dem Gelände, Gebäuden aber auch Vogel- und Insektenschwärmen, Schiffen, Flugzeugen oder Düppel entstehen, zu starken Überschätzungen von Niederschlagsintensität und -summe führen.

Entsprechend hoch ist die Zahl verschiedener Algorithmen zur Erkennung nichtmeteorologischer Echos. Es existieren allerdings nur wenige Methoden, die ausschließlich auf Basis eines zweidimensionalen Niederschlagsscans eine Detektion durchführen können. Einer dieser Ansätze nach Gabella and Notarpietro (2002) wurde auf seine langfristigen Detektionseigenschaften untersucht. Wie Abb. 0.1 zeigt, hat eine Korrektur mit diesem Algorithmus deutlich positive Auswirkungen auf die Jahressumme des geschätzten Niederschlags. Andererseits verbleiben auch nach der Korrektur noch diverse Artefakte im Bild bestehen, die wahrscheinlich nur über komplexere Methoden entfernt werden können.

Dämpfungskorrektur

Dämpfung in Bereichen intensiven Niederschlags ist ein Problem kürzerer Wellenlängen auf das schon früh hingewiesen wurde (Hitschfeld and Bordan, 1954). Der gleiche Artikel beschreibt neben dem Problem auch einen potentiellen Lösungsansatz, der bei starker Dämpfung aufgrund von Unsicherheiten in der Radarkalibration und der Niederschlags-Dämpfungsbeziehung, instabil wird und zu größeren Fehlern führt als ohne Korrektur.

In der vorliegenden Arbeit wurde deshalb der Ansatz von Krämer (2008), der von Jacobi et al. (2011) um eine weitere stabilisierende Komponente erweitert wurde, verwendet. Die Ergebnisse zeigen eine deutliche Verbesserung der Schätzung intensiver Ereignisse, bei einer gleichzeitigen Überschätzung kleiner bis mittlerer Ereignisse. In

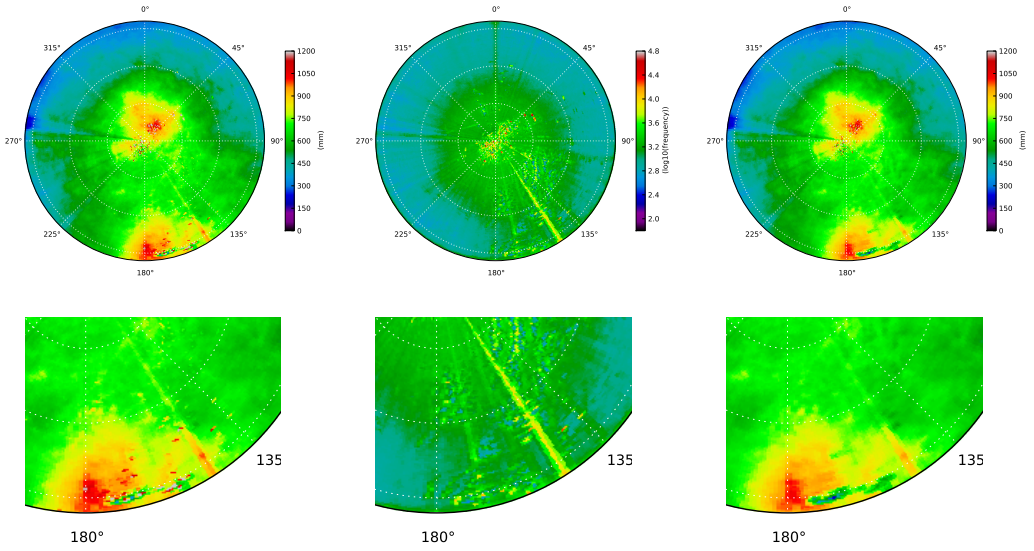

(a) unkorrigiert **(b)** Clutterhäufigkeit **(c)** korrigiert

Abb. 0.1.: Übersicht über die Auswirkungen des Clutterfilters auf die Jahressumme des Niederschlags für das Jahr 2008. Oben: Gesamtansicht des Radars Türkheim, unten: Detailansicht

der Jahressumme ergaben sich ebenfalls keine unplausiblen Werte, was die Stabilität der Methode noch einmal verdeutlicht.

Advektionskorrektur

Aus der zeitlichen Abfolge von Radarbildern lassen sich visuell leicht die Bewegungsrichtungen der einzelnen Niederschlagsfelder erkennen. Algorithmen aus der Computervision ermöglichen es, Betrag und Richtung des scheinbaren Windfelds auf objektive Weise durch den Computer zu ermitteln.

Die Bestimmung des Advektionsfelds ermöglicht eine Vorhersage der weiteren Bewegung des Niederschlagsfelds, kann aber auch direkt zur Korrektur der Radarakkumulation genutzt werden. Bei sich schnell bewegenden Feldern kommt es nämlich aufgrund der intermittierenden Messung des Radars zu wellenähnlichen Mustern, sofern die Bilddaten einfach addiert werden, wie in Abb. 0.2a zu sehen. Hier kann eine Advektionskorrektur, welche die Bewegung des Feldes während des unbeobachteten Zeitraums nachvollzieht und so eine Interpolation zwischen zwei Radarbildern liefert, zu zumindest visuell deutlich besseren Ergebnissen führen (vgl. Abb. 0.2b).

Zunächst wurden zwei bekannte und ein bislang noch unbekannter Algorithmus zur Bestimmung des Advektionsfeldes auf ihre Parametersensitivität und allgemeine Leistungsfähigkeit hin untersucht. Dabei zeigte sich eine bemerkenswerte Robustheit des neuen Algorithmus, dessen Ergebnisse auch in Bezug auf die Genauigkeit des ermittelten Advektionsfeldes, die der beiden Vergleichsalgorithmen übertrafen.

Auf Basis dieser Erkenntnisse, wurde der neue Algorithmus genutzt, um das korrektive Potenzial einer Advektionskorrektur auf die Übereinstimmung zwischen Radar und Bodenakkumulationen zu untersuchen. Je nach betrachtetem Gütemaß

zeigte sich eine teilweise Verbesserung oder eine hauptsächliche Verschlechterung der quantitativen Übereinstimmung zwischen stündlichen Radar- und Bodenakkumulationen.

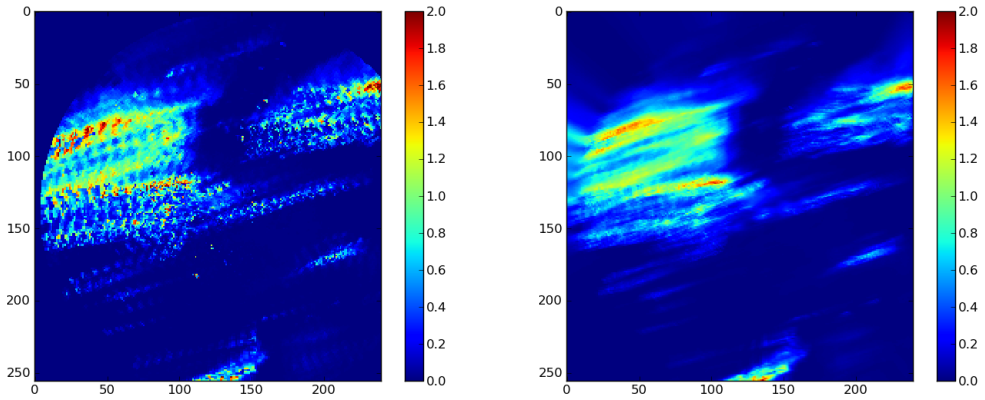

(a) ohne Advektionskorrektur **(b)** mit Advektionskorrektur

Abb. 0.2.: Einfluss der Advektionskorrektur auf die Akkumulation; Radar Dresden, Zeitraum: 23.06.2008 01:50–02:50 UTC; Niederschlagsskala in mm

Geostatistische Analyse von Radardaten

Dieser Teil der Arbeit stellt zwei Untersuchungen vor, die zum Ziel hatten, den Einfluss der räumlichen Mittelung über das Radarmessvolumen auf das Variogramm näher zu bestimmen.

Das Variogramm ist in der klassischen Geostatistik die maßgebende Funktion zur Beschreibung des räumlichen Zusammenhangs der beobachteten Größe und hat großen Einfluss auf die Ergebnisse von Interpolationsmethoden wie Kriging.

Aus der geostatistischen Theorie ist zu erwarten, dass eine räumliche Glättung durch ein gleitendes Mittel, zu einer Verstärkung des scheinbaren Zusammenhangs des Feldes, und somit zu einer Erhöhung der effektiven Reichweite des Variogramms führt. Mittels zweier unterschiedlicher Methoden wurde dieser Effekt für Radardaten nachzuweisen versucht.

Bei der ersten Methode wurden Variogramme ausschließlich aus Daten gebildet, deren Messvolumen identisch groß war. Im Falle von Radar sind dies alle Volumina mit gleichem Abstand zur Antenne. Da die resultierenden Variogramme für ein einzelnes Bild zu instabil waren, wurden die Variogramme mehrerer Bilder gemittelt. Dabei war zu beachten, dass sich das Feld in dieser Zeit nicht wesentlich veränderte. Die Analyse der effektiven Reichweite der an die gemittelten empirischen Variogramme angepassten theoretischen Funktionen, zeigte tatsächlich einen Anstieg für wachsendes Messvolumen. Allerdings ist dieser Anstieg um eine Größenordnung stärker als durch die Theorie zu erwarten wäre. Des Weiteren zeigte sich, dass bereits ein Niederschlagsgebiet mit etwas größerer Ausdehnung als die übrigen, einen Einfluss auf das Variogramm hat, der wesentlich größer ist, als der untersuchte Regularisierungseffekt.

Die zweite Methode ermöglichte über einen Maximum-Likelihood Ansatz zwar im Prinzip die Bestimmung des Regularisierungseffekts für ein einzelnes Bild, al-

lerdings zeigten sich auch hier Widersprüche zwischen den ermittelten und den aus der Theorie zu erwartenden effektiven Reichweiten. Darüber hinaus eignet sich diese Methode, aufgrund ihres hohen Rechenaufwands, nicht für eine Bearbeitung größerer Datensätze.

Aneichung von Radar- an Bodendaten mittels eines Copulainterpolationsansatzes

Interpolationen auf Basis von Copulas zeigen in verschiedenen Veröffentlichungen eine Verbesserung der eigentlichen Interpolationsgüte sowie der Schätzung der damit verbundenen Unsicherheit gegenüber klassischen geostatistischen Methoden wie Kriging. Durch die Trennung von Randverteilung und Abhängigkeitsstruktur erlauben Copulas eine wesentlich flexiblere Beschreibung eines stochastischen Prozesses bei weitgehender Unabhängigkeit von Annahmen zur Verteilung der Ausgangsdaten.

Nachdem bislang noch keine Untersuchungen zu Aneichungen von Radar- an Stationsdaten mittels Copulas vorliegen, wurde in diesem Teil der Arbeit ein solcher Ansatz entwickelt und mit anderen Methoden zur Stationsinterpolation bzw. -aneichung verglichen.

Annahme von Niederschlag als kontinuierlicher Prozess mit einem Schwellwert

Ein Problem bei der stochastischen Modellierung von Niederschlag ist dessen Intermittenz. Die Beschränkung auf strikt positive Werte führt zu einer schiefen Verteilung, die Tatsache, dass Niederschlag nicht überall auftritt, führt zu einem überproportional hohen Anteil an Nullwerten, die nicht durch eine einfache Verteilungsfunktion beschrieben werden können.

Um dieses Problem zu lösen werden im Allgemeinen zwei Ansätze verfolgt. Der erste nutzt zwei Verteilungsfunktionen um Auftreten und Menge separat zu modellieren. Für räumliche Interpolationen entspricht dies häufig einer Indikatorinterpolation, die die Orte bestimmt, an denen Niederschlag auftritt, während eine nachgeschaltete Interpolation die Niederschlagsmenge ermittelt.

Der zweite Ansatz, der hier verfolgt wurde, betrachtet den Niederschlag als Ergebnis eines latenten Prozesses, bei dem Niederschlag tatsächlich nur auftritt, wenn der latente Prozess einen bestimmten Schwellwert überschreitet. Interpretiert man den latenten Prozess als den in einer Luftmasse vorhandenen Wasserdampf mit vollständiger Sättigung als Schwelle ab der Niederschlag auftreten kann, lässt sich sogar eine physikalische Erklärung für diese Annahme finden, die aber durch konkrete Untersuchungen noch zu erhärten wäre.

Dennoch ermöglicht dieser Ansatz die Modellierung des Niederschlags mit nur einer Verteilungsfunktion, was die weiteren Berechnungen erleichtert. Die Schätzung der räumlichen Struktur wurde ebenfalls auf diese Annahme angepasst, wodurch Gebiete ohne Niederschlag weniger Einfluss erhalten als bei herkömmlichen Schätzmethoden.

Berücksichtigung der Übereinstimmung zwischen Radar- und Bodenmessung

Eine weitere Innovation stellt die Berücksichtigung der Radardaten direkt während der Interpolation dar, indem der Wert der Radarmessung über dem Interpolationsort als zusätzliche Information mit in die Berechnung der bedingten Verteilung einbezogen wird. Dadurch entfallen störanfällige Kombinationsmethoden wie z. B. im Falle des Mergings (Ehret, 2003). Des weiteren wird die Radarinformation nur in dem Maße berücksichtigt, wie sie mit den Stationsmessungen übereinstimmt. Hierzu wird, ebenfalls unter Zuhilfenahme des Ansatzes einer zensierten latenten Variablen, die Korrelation zwischen Stations- und Radarmessungen bestimmt und das Gewicht der Radardaten um diesen Faktor vermindert. Dies führt zu einer deutlichen Verbesserung der Ergebnisse im Vergleich zur vollständigen Hinzunahme oder dem Weglassen der Radarinformation.

Ergebnisse der Aneichung

Zusätzlich zu den oben erwähnten Vorzügen, zeigte sich auch, dass die Aneichung sehr robust gegenüber den Eingangsdaten ist. So erkennt man in Abb. 0.3 (a) und (b), dass die zensierte Copulainterpolation mit Drift (CCID) zu ähnlichen Ergebnissen (copula expect.) kommt, unabhängig davon ob als Radarinformation nur clutterkorrigierte (Abb. 0.3a) oder die clutter- und dämpfungskorrigierten Daten aus dem vorangehenden Kapitel verwendet wurden (Abb. 0.3b).

Es soll aber nicht unerwähnt bleiben, dass auch andere Methoden (in diesem Beispiel Kriging mit Radar als externer Drift (EDK); Abb. 0.3c) zu guten und in der Kreuzvalidierung teilweise auch besseren Ergebnissen führen.

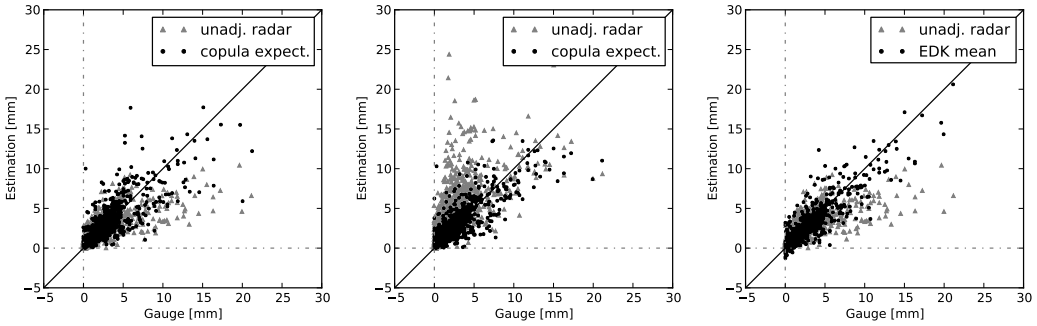

(a) CCID **(b)** CCID_A **(c)** EDK

Abb. 0.3.: Vergleich des Effekts der Aneichung für verschiedene Methoden und Radardatensätze; (a) zensierte Copulainterpolation mit clutterkorrigierten Radardaten als Zusatzinformation, (b) zensierte Copulainterpolation mit clutter- und dämpfungskorrigierten Radardaten als Zusatzinformation, (c) External Drift Kriging mit clutterkorrigierten Radardaten als Zusatzinformation

Unsicherheitsanalyse

Ein Vorteil der neu entwickelten Copulainterpolation gegenüber bekannten Methoden ist eine genauere Quantifizierung der mit der Interpolation verbundenen Unsicher-

heit. Dies wird insbesondere dann wichtig, wenn nicht nur Interpolationen sondern auch stochastische Simulationen des Niederschlags durchgeführt werden sollen, wie sie z. B. für Studien zu Unsicherheiten der Abflussvorhersage aufgrund der Fehler in der Niederschlagsschätzung benötigt werden.

Für gewöhnlich werden in der Kreuzvalidierung spezifische Schätzwerte mit einer Referenz verglichen. In diesem Falle ist die Referenz eine Bodenmessung und die Schätzung entweder, im Falle einfacher Interpolationen der Wert der Interpolation am Ort der Bodenmessung, oder, im Falle der Copulainterpolation, deren Ergebnis eine vollständige bedingte Verteilung an dem Ort ist, der Erwartungswert der Verteilung.

Für die Unsicherheitsanalyse wurde nun während der Kreuzvalidierung zusätzlich das Quantil der Bodenmessung in der bedingten Verteilung bestimmt. Für die betrachteten Kriging-Varianten war eine Quantilsbestimmung ebenfalls möglich, unter der Annahme, dass Kriging-Schätzung und Schätzvarianz die Parameter einer Normalverteilung bilden. Falls die Unsicherheit korrekt abgeschätzt wurde, sollten die Quantile gleichverteilt zwischen 0 und 1 sein.

Ein Ergebnis für die hydrologisch relevanten Niederschlagssummen größer 1 mm/h ist in Abb. 0.4 zu sehen. Es zeigt sich, dass die Copulainterpolation (CCID) das Kriterium der Gleichverteilung wesentlich besser erreicht als z. B. Kriging mit externer Drift (EDK), da die Bodenmessung bei EDK häufiger in den besonders hohen und niedrigen Quantilen vorzufinden sind, was auf eine Unterschätzung der Unsicherheit durch EDK hineweist. Auch bei CCID ist eine höhere Anzahl hoher Quantile zu verzeichnen.

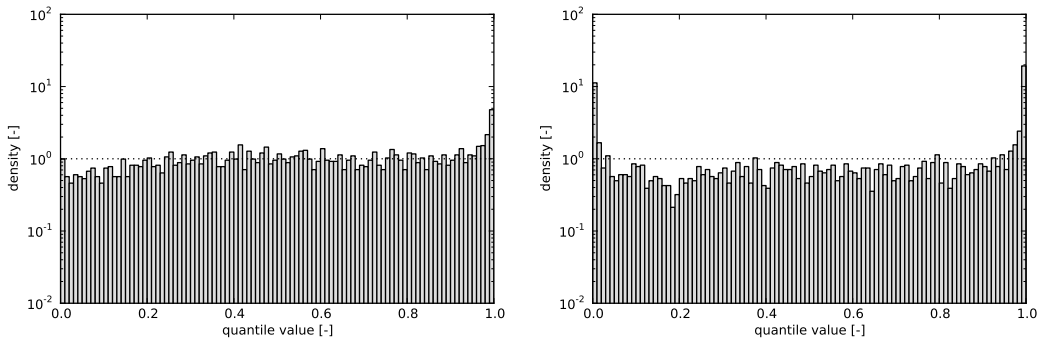

(a) CCID **(b)** EDK

Abb. 0.4.: Verteilung der Quantile der Stationsmessung in den geschätzten bedingten Verteilungen während der Kreuzvalidierung für Niederschlagswerte größer 1 mm/h; Zeitraum Mai-August 2008

Auswirkungen auf die Hydrologische Modellierung

Zum Abschluss der Arbeit wurde untersucht, inwieweit sich die einzelnen vorgestellten Niederschlagsschätzmethoden über verschiedene Skalen hinweg unterscheiden. Die Skalenanalyse wurde gewählt, da sie dem Prozess der flächenhaften Integration des Niederschlags über ein Einzugsgebiet ähnelt. Hiermit lässt sich zwar keine

vollständige hydrologische Verifikation erreichen; diese ist, nach Ansicht des Autors, aufgrund der oben erwähnten Kalibrationsproblematik, ohnehin derzeit kaum möglich. Allerdings lassen sich Unterschiede zwischen den einzelnen Niederschlagsschätzungen aufzeigen, sowie Skalen ermitteln, ab denen diese Unterschiede nach und nach verschwinden und somit auch hydrologisch keine Unterschiede in der Abflussantwort eines Einzugsgebiets zu erwarten sind.

Dazu wurden alle zuvor betrachteten Niederschlagsschätzungen auf ein gemeinsames Raster transferiert, über Flächen von 1x1 km^2 bis 256x256 km^2 aggregiert und anschließend mittels verschiedener Übereinstimmungsmaße miteinander verglichen.

Erwartungsgemäß bestehen die geringsten Unterschiede zwischen reinen Stationsinterpolationen. Diese erscheinen bis zu einer Aggregationsstufe von 100 km^2 sogar nahezu skaleninvariant. Des Weiteren verschwinden die Unterschiede zwischen verschiedenen Kriging-Varianten schneller als zwischen Kriging und der Copulainterpolation mit Zusatzinformation. Die Unterschiede sind ebenfalls für die kleinste Skala am größten, nehmen aber erst bei Aggregierungen über 1.000 km^2 deutlich ab.

Für die hydrologische Modellierung lässt sich hieraus schließen, dass, sofern man nur am Abfluss am Gebietsauslass interessiert ist, Stationsinterpolationen für Einzugsgebiete größer 1.000 km^2 den gleichen Zweck erfüllen können wie höher aufgelöste Daten. Ob, um die weit höhere räumliche Variabilität der radarbasierten Niederschlagsschätzungen angemessen berücksichtigen zu können, verteilte Modelle mit ähnlich hoher räumlicher Auflösung notwendig sind, müssen tatsächliche Modellierungen klären. Dabei ist jedoch die Problematik zu berücksichtigen, dass während einer zunächst für jeden Niederschlagsinput separat durchzuführenden Modellkalibrierung deutlich unterschiedliche Parametersätze ermittelt werden können, die verschiedene systematische Fehler der einzelnen Niederschlagsschätzungen ausgleichen. Dies sollte in die abschließende Bewertung der Güte der modellierten Abflüsse mit einfließen.

Schlussfolgerungen

Ziel dieser Arbeit war es, Wetterradardaten besser für die hydrologische Anwendung nutzbar zu machen. Hierzu wurden deterministische Methoden verwendet, die spezifische Fehler identifizieren bzw. korrigieren sollten. Für alle drei vorgestellten Ansätze konnten Korrekturerfolge aber auch weiter bestehende Probleme aufgezeigt werden. Einige Fehlerquellen, die hauptsächlich mit der vertikalen Struktur des Niederschlags zusammenhängen, konnten aufgrund der vorhandenen Daten nicht bearbeitet werden, obwohl ihr langfristiger Einfluss sehr groß ist. Dies sollte ein Fokus weiterführender Arbeiten sein.

Nachdem alle deterministischen Korrekturen ausgeschöpft wurden, erhofft man sich von Aneichmethoden eine letzte Verbesserung der Radardaten im Vergleich mit Bodenmessungen. Die hier erstmalig vorgestellte Aneichung auf Basis von Copulas bietet mit den vorgestellten Erweiterungen Lösungsansätze zu zwei grundsätzlichen Problemen bei der Verbindung von Radar- und Bodenmessung: Zum einen erlaubt die Annahme des Niederschlags als Schwellwertprozess eine gemeinsame Betrachtung von Niederschlagsfeldern und niederschlagsfreien Gebieten; zum anderen erlaubt die Berücksichtigung der Korrelation zwischen den Bodenmessungen und der Radarin-

formation am gleichen Ort, eine Anpassung der Aneichung an die Übereinstimmung zwischen Radar und Stationen, was grobe Fehlkorrekturen verhindern kann. All diese Erweiterungen führen zu einer besseren Abschätzung der Unsicherheit der Anpassung im Vergleich zu anderen Methoden.

Inwieweit derart korrigierte Daten zu besseren Ergebnissen in der hydrologischen Modellierung führen, wird erst abschließend geklärt werden können, wenn geeignete Methoden gefunden wurden, die Wechselwirkungen zwischen Niederschlagsinput und Modellkalibrierung zu quantifizieren oder zu reduzieren. Die großen Unterschiede zwischen radarbasierten Niederschlagsschätzungen und Stationsinterpolationen lassen eine verteilte Modellierung in hoher räumlicher Auflösung nötig erscheinen, die wiederum mit ihren eigenen Unsicherheiten behaftet ist.

1. Introduction

In one of the earliest publications on meteorological uses of radar, Marshall et al. (1947) made the following statement about the potential of weather radar observations:

> *It may be possible therefore to determine with useful accuracy the intensity of rainfall at a point quite distant (say 100 km) by the radar echo from that point.*

This was the starting point for intensive research on measuring precipitation using weather radar systems, in the hopes to be able to remove the costly gauge stations by a network of a few radars, which would, in addition, cover the whole area instead of just measuring at a certain point.

In 1979, however, Wilson and Brandes summarized the state of use of radar precipitation estimates as follows:

> *Radar can produce detailed precipitation information for large areas from a single location in real time. Although radar has been used experimentally for nearly 30 years to measure rainfall, operational implementation has been slow. Today we find that data are underutilized and both confusion and misunderstanding exist about the inherent ability of radar to measure rainfall, about factors that contribute to errors ...*

Another 30 years later, it must be said that at least in Germany the situation has not changed much. All major flood forecast centers still exclusively use gauge data for operational water balance modeling and flood forecasting. Weather radar data is used either only for pilot studies or not at all. Also, the majority of research in hydrology is still using interpolated gauge data for driving models.

Although the potential of precipitation data with high spatial as well as temporal resolution, which modern radar systems offer on a routinely basis, is generally acknowledged, it still remains underutilized. Few studies, like those of Zoccatelli et al. (2011) show the benefits of using weather radar data for flood modeling but only in hindsight. A few operational systems exist like, for example, the flood forecasting for the Goldersbach catchment operated by the city of Tübingen, which had been developed and presented by Ehret (2003), but these are local solutions and are usually installed only *after* some flooding had occurred.

Floods represent one of the most important type of natural disaster in Germany. Large scale flooding like the Oder flood in 1997 or the Elbe flood in 2002 cause large damages ranging from € 330M (Oder, Germany only) to approx. € 9B (Elbe, Germany only) and around 20 human casualties. The Elbe flood is also an example of a mixture between large scale and flash flood. Intense rainfall in the Ore Mountains led to flash floods in the Elbe tributaries, Weisseritz, Müglitz and Mulde, laying

waste to many towns along these rivers (IKSE, 2004). The large scale flood of the following days was mainly fed by waters coming from the Czech part of the Elbe catchment. Another flash flood hit the Starzel catchment, a small tributary of the Neckar in the south-west of Germany with an area of 123 km^2 in June 2008. A thunderstorm led to an increase of discharge from an average flow of approx. 1 m^3/s to approx. 125 m^3/s within a few hours, causing € 3.4M in damages and 3 lives lost. Unfortunately, the only rain gauge in this area did not report any data during the time of the most intense precipitation. And even if it had, as the data is usually only gathered in hourly intervals, there would not have been enough time to issue a warning.

The weather radar network of the German Weather Service provides a complete volume scan every 15 minutes and a low level precipitation scan every 5 minutes for each of its 16 weather radar stations. This data can be made available shortly after it has been recorded.

What may be the reasons for the reluctant use of weather radar for flood forecasting?

Fig. 1.1 shows an accumulation over the year 2009 for the German composite, based on the quality corrected RY product. This product is generated every 5 minutes from the low-level precipitation scans, which have been screened beforehand for a number of common radar errors and converted to rain rates.

In the long accumulation, error correction seems not to have happened at all. Instead of a smoothly varying field, the individual radar umbrellas are clearly visible. Large accumulations rarely coincide with mountainous regions, where high precipitation amounts would be expected in this climatic region. Instead it seems like it is dependent on the radar site, whether large accumulations occur or not. A few mountain tops in the south are visible but only because of greatly reduced accumulations, which are most probably due to oversuppression due to a Doppler clutter filter. The two mountain ranges of the Vosges Mountains and the Black Forest are faintly visible in the accumulations in the south west, but not with the amount that would be expected. This may be attributed to the observing radar being situated on the Feldberg, the highest mountain of the Black Forest, at about 1500 m.a.s.l. It is to be expected that most of the time, the radar will measure in the snow layer above any liquid precipitation, which may fall at lower altitudes. To the north, ship routes can be seen as well as bright band influences, leading to regions of high accumulations that appear circularly around a radar. Most radars show a decrease in precipitation amount with range, which is mostly due to the increased height and size of the beam with distance. In several places residual clutter and partial as well as total beam blockages can be observed. To the south-east and east, shadowing effects due to the Alps, the Bavarian Forest and the Ore Mountains obscure the rainfall at their far side. In short, these radar observations do not properly represent the rainfall regime over the covered area. Several other errors, like anomalous propagation and attenuation only occur at specific times or during periods of intensive precipitation and usually cannot be identified in long-term accumulations. Nevertheless they strongly and negatively affect the precipitation estimates from radar and thus reduce its quality for hydrological modeling and forecasting even further.

Another obstacle for the adoption of weather radar data in operational hydrological forecasting is the fact that the models in use at the Federal flood forecasting agencies

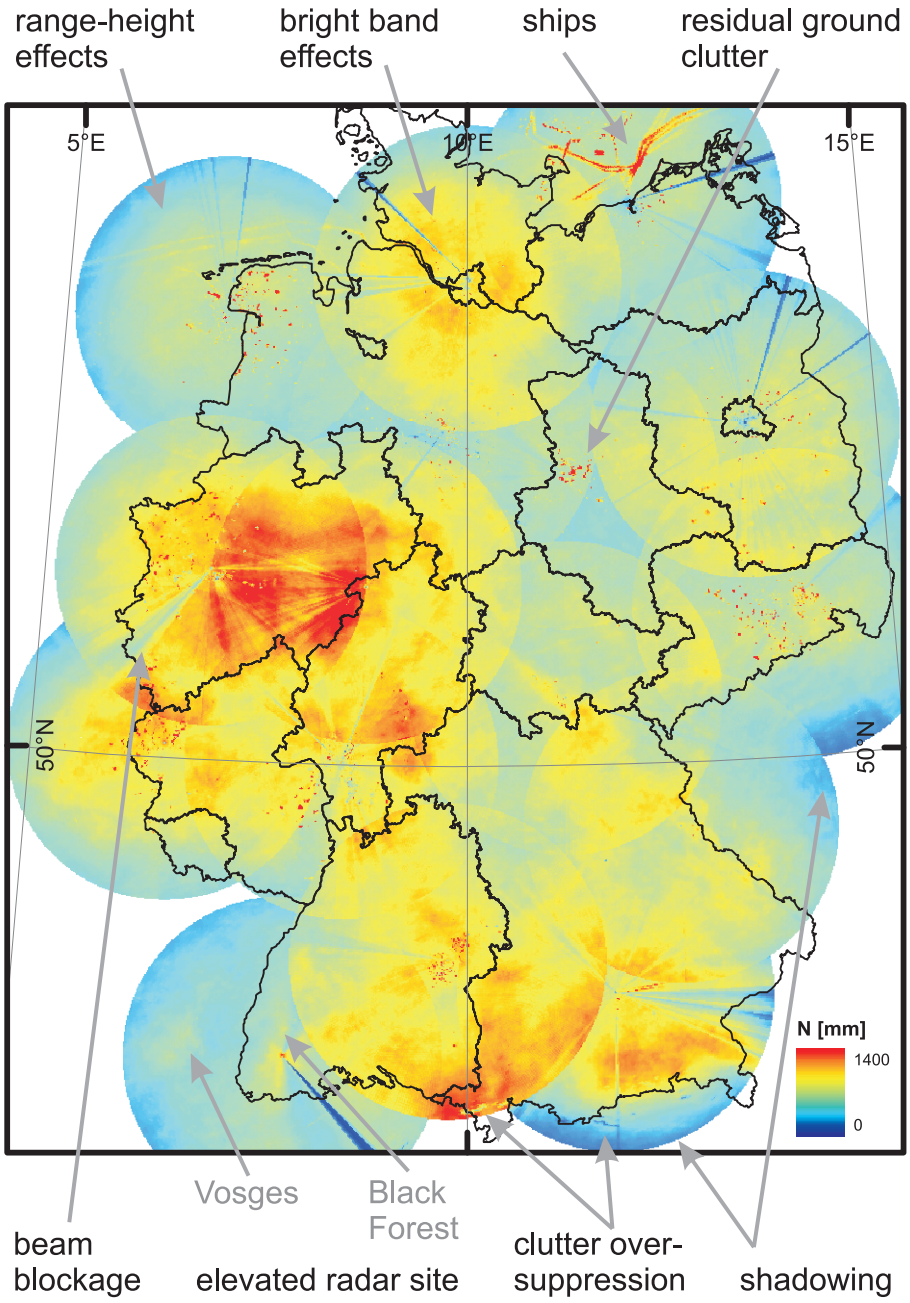

Figure 1.1.: Accumulation of quality corrected precipitation estimates from radar data (DWD RY-product, German composite) for the year 2009

are rather complex pieces of software, which are still often calibrated manually. As will be explained later, feeding radar precipitation estimates to a model calibrated to gauge interpolations is almost inevitably doomed to provide bad results. Initially bad results coupled with high costs of recalibration and the aforementioned problems with data quality make the reluctance of flood forecasters to adopt this data source understandable.

Nevertheless, it is the author's opinion that weather radar provides unprecedented possibilities to observe precipitation at high resolution over a large area and that just the goal of 'useful accuracy' has not been reached, yet. This thesis, therefore, is intended to contribute a few further steps towards improving the quality and understanding about the properties of weather radar data to increase its usefulness for hydrological applications. In chapter 2 three methods to correct for some of the errors mentioned above will be presented. They were developed as part of the OPAQUE[1] project. This project, funded by the Federal Ministry of Education and Research (BMBF), aimed at improving operational flood forecasts in small catchments like the Weisseritz and the Starzel, including but not limited to improvements in radar precipitation estimates. The radar data for this project, on which this thesis builds was kindly provided by the German Weather Service, which is most gratefully acknowledged.

In order to mitigate some of the errors presented in fig. 1.1, the DWD project RADOLAN[2] implemented several gauge adjustment techniques including difference and factor interpolation as well as the merging method developed by Ehret (2003). Based on the interpolation method Kriging and with the help of a multiplicative combination scheme, this method has shown good performance when compared with other gauge adjustment techniques. A more detailed review as well as a new method, which may overcome a few problems of the former as well as other approaches will be presented in chapter 3.

In the last chapter, some analyses will be presented showing the differences between different gauge adjusted precipitation estimates and their behavior across different scales. Awareness of these properties should help in better understanding different outcomes of hydrological model simulations when driven by the different inputs.

With the exception of the algorithm comparison in section 2.4, which used data from the DWD radar Dresden in the east of Germany, all other analyses were conducted on data from the DWD radar Türkheim. The radar is located in the eastern part of the Federal state of Baden-Württemberg (whose outline is given in fig. 1.2) in the south-west of Germany. Its umbrella with a radius of 128 km, covers most of Baden-Württemberg and the entire Neckar catchment. It also covers the aforementioned Starzel catchment at an almost ideal distance of 60-70 km. A geographical overview of the relative locations is given in fig. 1.2.

[1] http://brandenburg.geoecology.uni-potsdam.de/projekte/opaque; accessed 2012-08-30
[2] http://www.dwd.de/RADOLAN; accessed: 2012-08-30

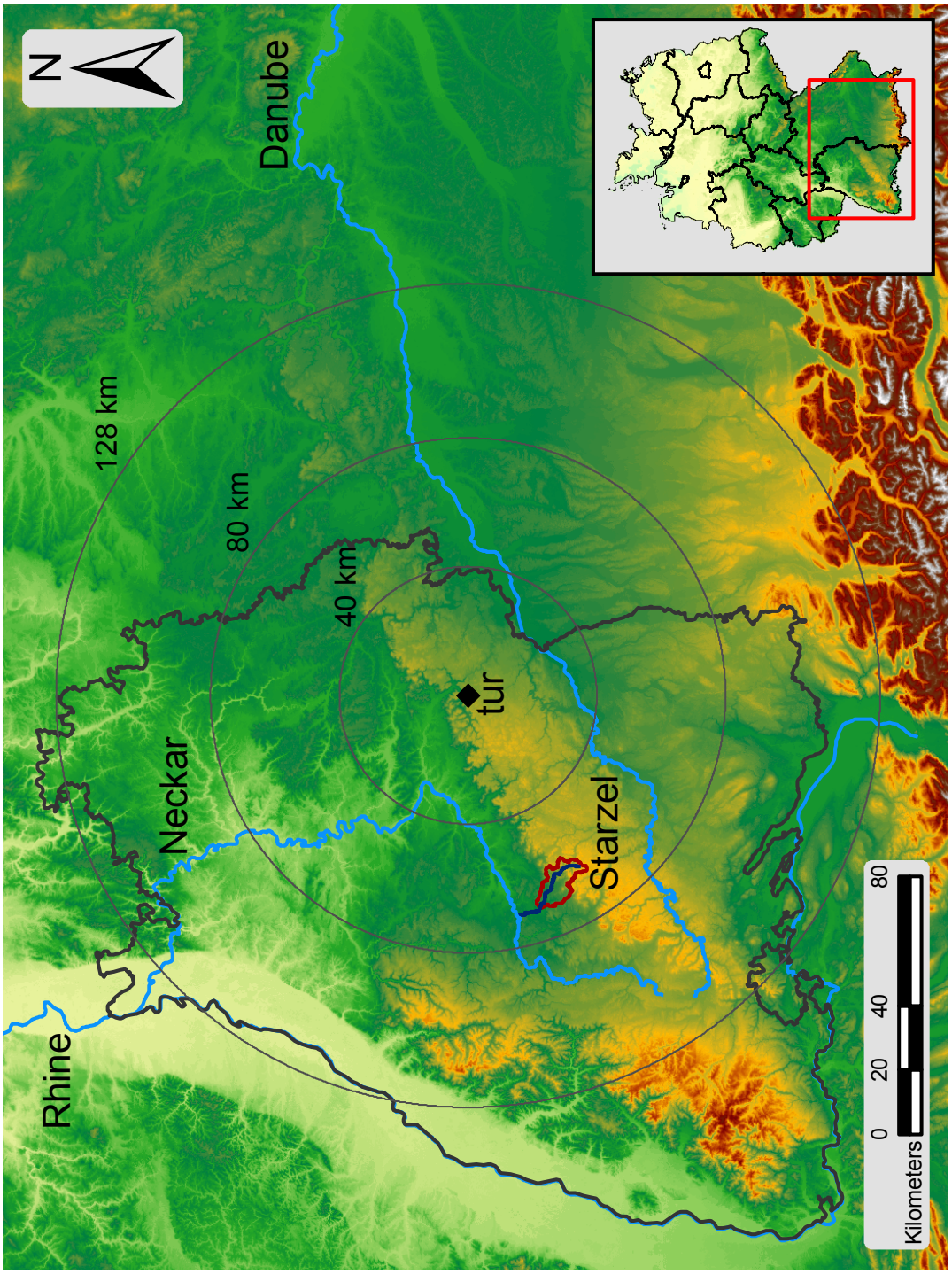

Figure 1.2.: Location of Radar Türkheim (marked 'tur') and the Starzel catchment

2. Deterministic Data Correction

2.1. Introduction

2.1.1. Historic Development of Weather Radar

The foundations of radar were laid by Heinrich Hertz in 1886, when he discovered that electromagnetic waves would be reflected by metallic objects. In 1904 Christian Hülsmeyer obtained a patent for a 'Telemobiloskop', a device which could detect ships by measuring the travel time of an electromagnetic wave. The development of radar technology started about 1930 as a means to track aircraft. Before and during the Second World War, secret developments took place in many countries including the UK, the U.S. and Germany, in order to provide early warning against air raids, and to guide flak and fighter planes towards incoming bombers.

According to Hitschfeld (1986), the first meteorological features may have been observed by radar as early as 1938. From 1944, the U.S. Air Force started training radar-weather officers. In the UK, researchers were given disused Royal Air Force stations to start meteorological observations. Since the 1950's dedicated radar systems were developed for meteorological observations and operational weather radar networks were installed by national weather services. Between 1980 and 2000 these networks were upgraded with coherent transmitters, which allowed the measurement of the velocity of the hydrometeors relative to the radar. After 2000 research has been conducted on further improving operational weather radar estimates by equipping the networks with dual polarization capabilities. The German Weather Service (DWD) is currently upgrading its network with dual polarization, which is planned to be completed by the end of 2014. A more detailed overview of the history of weather radar, for example in the U.S., can be found in Whiton et al. (1998).

2.1.2. Physical Principles of Radar

Radar is an acronym for **Ra**dio **D**etection **a**nd **R**anging. In the following, the core physical principles will be summarized and the reasons for the necessity of data correction explained. More detailed information can be found in textbooks on the matter by Collier (1996), Battan (1973), Atlas and Battan (1990), Skolnik (1990), Doviak and Zrnić (1993) and Bringi and Chandrasekar (2001).

Radio - The Electromagnetic Spectrum

A Radar system emits electromagnetic radiation with frequencies close to the highest radio frequencies, hence the first part of the acronym. The left part of fig. 2.1 shows the overall position of radar frequencies and associated wavelengths inside the whole electromagnetic spectrum. There it can be seen that radar frequencies are much lower than the visible or infrared radiation. Radiation of these wavelengths may

pass through clouds and rainfall more or less undisturbed making long range observations of weather possible in the first place. The right part gives more detail on the individual frequency bands, which are currently used for meteorological observations of the atmosphere. S-Band radars are operated mainly in regions with strong convec-

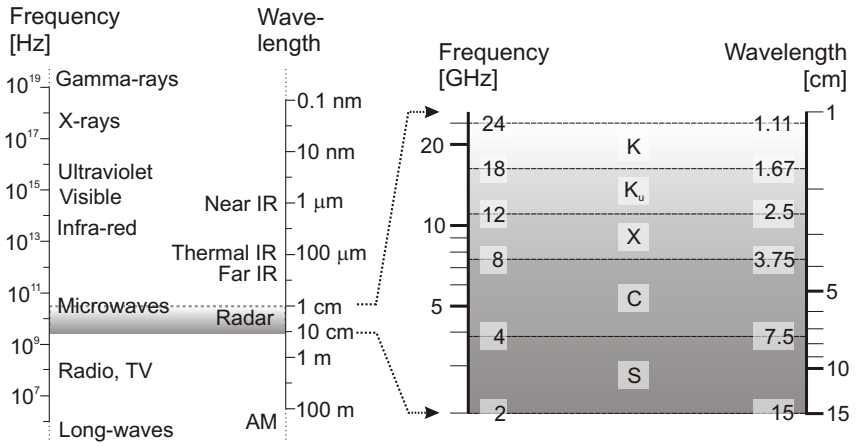

Figure 2.1.: Electromagnetic Spectrum

tive precipitation where drop sizes are expected to be large. This band is necessary in tropical and subtropical regions. At this band negligible attenuation occurs, however, large antennas are needed to achieve acceptable spatial accuracy and detection levels. These radars may observe precipitation up to a range of 250 km.

In regions where light to medium intensities of rainfall are prevalent, C-Band radars provide a good compromise between sensitivity and susceptibility towards attenuation and signal saturation. C-Band systems are the most common in mid and high latitudes. Their typical observation range is between 130 and 250 km.

X-Band radars, achieve high spatial resolution at antenna sizes that make it possible to mount them on mobile systems. Due to the even shorter wavelengths, sensitivity to rainfall is very high, but attenuation already becomes an issue at medium intensities and can quickly saturate for higher intensity precipitation. Therefore, the observation range is usually limited to about 30 to 60 km.

K_u and K band radars are generally used for cloud observations as their very short wavelengths make them very sensitive to cloud droplets. Consequently, precipitation severely affects measurements at this frequency band and the observation range is limited to a few tens of kilometers.

Detection - Scattering

As mentioned already, the wavelength of an electromagnetic wave strongly determines how the radiation interacts with other matter. Mie (1908) was able to provide an exact solution to the Maxwell equations for the scattering at spherical bodies. The backscattering cross section σ is given by the following equation.

$$\sigma = \frac{\pi D^2}{4a^2} \left(\sum_{n=1}^{\infty} (n-1)^n (2n+1)(a_n - b_n)^2 \right) \tag{2.1}$$

Here, D is the diameter of the sphere, $a = \pi D/\lambda$ is the electrical size, λ is the wavelength and a_n and b_n are coefficients of the scattering field. These coefficients involve Bessel and Hankel functions and are dependent on the scattering angle, the electrical size and the complex refractive index (Collier, 1996). The fact that the coefficients in the infinite series are size dependent make an exact solution of eqn. 2.1 for a large number of possible drop diameters a computationally intensive task. However, if the particles in question may be assumed to be small in comparison with the wavelength, the Mie solutions may be approximated by the so-called Rayleigh scattering cross section as presented in eqn. 2.2. The particles may assumed to be small if their diameter is smaller than approximately 0.07 times the wavelength or, equivalently, the electrical size is smaller than 0.22 (Battan, 1973).

$$\sigma = \frac{\lambda^2 a^6}{\pi} \left| \frac{m^2 - 1}{m^2 + 2} \right|^2 \tag{2.2}$$

Substituting the electrical size into this equation leads to

$$\sigma = \frac{\pi^5}{\lambda^4} \left| \frac{m^2 - 1}{m^2 + 2} \right|^2 D^6 \tag{2.3}$$

This is the form that is generally used to show the strong dependence of the backscattered intensity on the drop diameter. Here m denotes the complex index of refraction, which is dependent both on the temperature and the aggregation phase of the hydrometeor. This fact is often neglected and just the index of refraction of water at a certain temperature is used regardless of height or actual aggregation phase.

Ranging

The distance r of a target from the radar antenna is determined by the travel time τ of the echo.

$$r = \frac{1}{2} \cdot c_{air} \tau \tag{2.4}$$

with c_{air} being the speed of light in air.

Quantification - The Radar Equation

The derivation of the radar equation is presented along the lines of Battan (1973) and Collier (1996), to which the reader is referred, if more detail is needed.

Assuming a sender emits electromagnetic energy with power P_t isotropically in all directions, the power on the surface of a sphere with radius r around the sender will be

$$P_S = \frac{P_t}{4\pi r^2} \tag{2.5}$$

Due to the directional characteristics of the antenna system, the emission is not isotropic, which is accounted for by introducing the antenna gain G. The power incident on a scatterer of area A_t is then

$$P_\sigma = \frac{P_t G A_t}{4\pi r^2} \tag{2.6}$$

The power that returns back at the antenna depends on the effective antenna cross section A_e according to

$$P_r = \frac{P_t G A_t A_e}{(4\pi r^2)^2} \tag{2.7}$$

According to Battan (1973) A_e can be shown to be

$$A_e = \frac{G\lambda^2}{4\pi} \tag{2.8}$$

Combining equations 2.7 and 2.8 leads to

$$P_r = \frac{P_t G^2 \lambda^2 A_t}{(4\pi)^3 r^4} \tag{2.9}$$

As the scatterers are generally neither of regular shape nor do they scatter radiation isotropically or completely. Therefore, their actual area A_t is replaced by an equivalent cross section σ_i of an ideal scatterer that would return the same power as the scatterer itself. Moving from one scatterer to many scatterers leads to equation 2.10.

$$P_r = \frac{P_t G^2 \lambda^2}{(4\pi)^3 r^4} \sum_{i=0}^{n} \sigma_i \tag{2.10}$$

Assuming that the scatterers are distributed homogeneously inside the illuminated volume V_m

$$V_m = \pi \left(r\frac{\theta}{2} \right) \left(r\frac{\phi}{2} \right) \frac{h}{2} \tag{2.11}$$

(one of the strongest assumptions in the radar equation), the general sum can be normalized to the beam volume.

$$\bar{P}_r = \frac{P_t G^2 \lambda^2 \theta \phi h}{2^9 \pi^2 r^2} \sum_{vol} \sigma_i \tag{2.12}$$

According to Battan (1973) an adjustment factor of $2\ln(2)$ must be applied to account for the antenna pattern, if it is assumed to be of Gaussian shape, which is the usual case.

$$\bar{P}_r = \frac{P_t G^2 \lambda^2 \theta \phi h}{2^9 (2\ln(2)) \pi^2 r^2} \sum_{vol} \sigma_i \tag{2.13}$$

Until now, no assumptions have been made yet about the scattering cross section. As presented in the previous section, the Mie scattering cross section would have to be calculated for each scatterer whose diameter is comparable to the wavelength of the radar signal. If the Rayleigh scattering approximation from equation 2.2 is used,

however, the scattering cross section can be directly related to the diameter D_i of the hydrometeors, leading to

$$\bar{P}_r = \left(\frac{\pi^3 P_t G^2 \theta \phi h}{2^{10} \lambda^2 \ln(2)} \right) \frac{|K|^2}{r^2} \sum_{vol} D_i^6 \tag{2.14}$$

The first part of equation 2.14 is a constant specific to the properties of the radar system only. The second part is dependent on the range and the refractive properties of the scatterers, while the sum accumulates their number and size. This sum is denoted by the reflectivity factor Z, however, most of the time it is just referred to as reflectivity.

$$\bar{P}_r = C \frac{|K|^2}{r^2} Z \tag{2.15}$$

Given that the radar constant C is known, which can be done by calibration and K can be assumed e.g. to be the value of water, equation 2.15 can be solved for Z, which is the usual representation of weather radar measurements.

Collier (1996) lists the assumptions, for the radar system and the sampling volume, under which equation 2.15 is valid. It can easily be seen that if the radar was not calibrated properly, the estimates of Z will be in error. Similarly, if the particles in the sampling volume are not all water or ice, K will introduce errors. This is especially the case, in regions of phase change. There, large snow flakes, who by themselves would have lower reflectivity due to the low index of refraction of ice, become coated with a thin layer of water, whose K is large. Thus they appear to the incoming radiation like enormous drops leading to the so-called Bright Band effect, which leads to large overestimations in those regions of stratiform rainfall where the radar beam intersects the melting layer. This is also one of the cases, where the vertical structure of precipitation will introduce errors. While the term 'non-uniform beam filling' is commonly used only if precipitation particles are only present in parts of the beam, this term could be more generally used for all cases, where the phase or number concentration of scatterers is inhomogeneously distributed throughout the beam volume. This class of errors is interlinked with errors due to the vertical profile of reflectivity (VPR). Here, errors due to different reflectivities aloft and close to the ground become mixed with inhomogeneously filled volumes at large distances from the radar, where the beam's center is high above the ground and the illuminated volume is large, spanning several kilometers in the vertical direction. Other types of errors are connected with special forms of weather or processes of precipitation generation. One major source of erroneous estimation stems from the fact that not everything that interacts with the radiation emitted by the radar is actually precipitation. Removing unwanted effects by clutter is the topic of the following section.

2.2. Clutter

2.2.1. Introduction

Clutter is a general term for unwanted echoes in a radar image. In this thesis, echoes are interpreted with the purpose of measuring precipitation. Therefore, every echo

that is not caused by precipitation will be considered as clutter. On the other hand, basically every object designated to be clutter in this context may also serve as a target in another. However, different radar setups in terms of frequency, scanning strategy etc., may lead to improved results in these cases.

Clutter from the weather radar perspective may be divided into two main classes: Stationary objects and non-stationary objects.

Stationary objects may further be divided into terrain, with the radar beam being intercepted by hills, mountains or trees, and man-made structures. These include buildings in general, although high-rise buildings including communication towers and wind power structures provide the more significant contributions to clutter. The main feature that can be used to identify and correct for this class of clutter is that their echoes always appear in the same place. One of the simplest filters is therefore a static map of all range bins, which exhibit strong reflectivities either during non-raining periods or which produce implausibly large accumulations during rain events or when summed over periods of months.

With the introduction of Doppler capabilities in weather radars, echoes from stationary objects may be filtered out directly by the signal processor of the radar itself (Doviak and Zrnić, 1993; Seltmann, 1997). Table 2.1 gives an overview of different filtering approaches using Doppler- and polarization information. An advantage of filtering is that, in principle, they allow for the separation of the meteorological and the clutter signal, so that even if a range-bin is affected by clutter, meaningful information about occurring precipitation can be retrieved. However, in certain cases, this filtering may remove signals from meteorological echoes, which cannot be recovered once the spectral information is not available any more. An example of this may be seen in section 2.2.2.

Table 2.1.: Clutter filtering techniques for application during raw signal processing, and their data requirements

Author	Algorithm Class	Input Data
Torres, 1999	filter (dynamic)	Doppler spectrum
Siggia, 2004	filter (dynamic)	Doppler spectrum
Zrnić, 2007	threshold (dynamic)	Polarization cross-correlation
		Differential phase
		Differential reflectivity
Nguyen, 2008	filter (dynamic)	Doppler spectrum

Under certain meteorological conditions, the radar beam will be reflected at a dryer layer of air and thus hit the ground at some range from the radar. This effect, which goes under the name of anomalous propagation, or *anaprop*, will produce echoes at azimuths and ranges usually not affected by clutter. Doppler processing may be used to remove these echoes, which cannot be handled using static maps, or which would otherwise need to be identified using propagation modeling including knowledge of the current state of the atmosphere.

Returning to the general classification, there are two main classes of objects leading to non-stationary clutter echoes. The first category are airborne animals like birds or insect swarms. The second class consists of man-made airborne objects like aircraft

and chaff. In a maritime environment two additional sources of non-stationary clutter can be identified. Ships will be detected by radar as well as sea waves, without being fixed to a certain location, and thus must also be categorized as non-stationary clutter.

Non-stationary clutter cannot be removed by using static clutter maps. Due to its movement it can also not be suppressed using Doppler filtering.

The detrimental effects of clutter for the hydrological use of weather radar data are obvious:

- Poorly filtered stationary clutter leads to large overestimations of precipitation rates and amounts in the affected areas. Especially in small catchments, this effect introduces large errors in the water budget.

- While not as detrimental when occurring sporadically, non-stationary clutter can also have a negative impact on precipitation estimates, if objects appear regularly around the same areas. This is particularly true, for example, around airports or along highly frequented waterways.

- Clutter will negatively affect any information extracted from a radar image that relies on properties of meteorological phenomena. One example, which will be discussed later in more detail, is the determination of the movement speed of precipitation fields using image analysis techniques. Here, the intermittent nature of non-stationary clutter but also the strong and immobile signal of stationary clutter may severely impede the performance of the algorithms estimating the advection field.

There are a few properties of clutter signals, which make it difficult to remove them using simple techniques. Due to the size of the producing object, clutter signals are usually quite strong. However, intense precipitation can also produce very strong signals of 50 dBZ and more. While a simple threshold filter may already detect and remove a lot of clutter, it will also remove many convective events and thus be unacceptable for flood forecasting. The same holds for the spatial extent of large signals. Clutter as well as strong convection produces very localized intense signals.

There have been many approaches to separate clutter from meteorological signals. Those, that would mainly detect static clutter rely on beam propagation modeling to estimate the locations where the beam would interact with the terrain (Delrieu et al., 1995; Bech et al., 2007; Krajewski et al., 2006). Static clutter could also be detected using Doppler information. Table 2.2 gives an overview of some clutter identification approaches and the data required to use them. The algorithms were classified according to the main method employed for the identification. In addition, the three columns *Doppler*, *3-D* and *Polarized* were given to summarize, if an algorithm needs Doppler-information, 3-D volume scan data or polarization information.

The reason for these distinctions is that for the current study only 2-D reflectivity data had been available. Therefore, while there is a wealth of identification algorithms available in the literature, only two of them (Gabella and Notarpietro (2002), Haddad et al. (2004)) were 'frugal' enough to be applied to the problem at hand.

Table 2.2.: Clutter identification techniques and their data requirements. A "*" next to one of the input data items implies that the data necessary for this approach needs to be acquired during or directly after signal processing, which is generally not available to end-users.

Author	Algorithm Class	Input Data	Doppler	3-D	Polarized
Giuli 1991	decision tree (dynamic)	Doppler velocity Horizontal reflectivity Differential reflectivity	yes	no	yes
Delrieu, 1995	propagation modeling (static)	Digital Elevation Model	no	no	no
Kessinger, 1997	fuzzy (dynamic)	3-D reflectivity Doppler velocity Doppler spectrum*	yes	yes	no
Grecu, 2000	neural network (dynamic)	3-D reflectivity	no	yes	no
Gabella, 2002	texture (dynamic)	2-D reflectivity	no	no	no
Steiner, 2002	decision tree (dynamic)	3-D reflectivity	no	yes	no
Haddad, 2004	texture (dynamic)	2-D reflectivity	no	no	no
Berenguer, 2006	fuzzy (dynamic)	3-D reflectivity Doppler velocity	yes	yes	no
Germann, 2006	decision tree (dynamic)	3-D reflectivity Doppler spectrum* Doppler velocity	yes	yes	no
Krajewski, 2006	propagation modeling (static)	Digital Elevation Model	no	no	no
Gourley, 2007	fuzzy (dynamic)	Polarization cross-correlation Differential phase Differential reflectivity	no	no	yes
Hubbert, 2009	fuzzy (dynamic)	Raw pulse amplitude spectra* Raw pulse phase spectra*	yes	no	no

2.2.2. Clutter Detection Using Spatial Correlation

As described in the introduction, only two algorithms were found in the literature to identify clutter on the basis of single-scan, two-dimensional reflectivity data. For this study, both were tested, however, the application of the method by Haddad et al. (2004) did not lead to satisfying results.

The approach presented by Gabella and Notarpietro (2002) appeared to be both easy to implement as well as effective in removing dynamic and static clutter. It consists of two sub-steps whose results are combined to form a resulting clutter map for each radar image.

The first step analyzes the image for texture. Each range-bin i is compared to its neighboring bins in a $n \times n$ window by calculating the difference $dBZ_i - dBZ_j$. Next, all differences smaller than a threshold tr_1 are counted. This number is then compared to a second threshold n_p. A range-bin is considered clutter if the number of small differences is below n_p. This effectively removes all kinds of higher intensity speckle including isolated clutter, birds, aircraft, etc., while leaving meteorological echoes, which usually show more spatial continuity intact.

The second step identifies clutter according to its spatial extent. In this step, first, contiguous regions of reflectivities larger than a threshold tr_0 are identified in the radar image. For each region the ratio of area (provided as range-bin counts) divided by circumference (again, as bin counts) is calculated and a region is identified as clutter, if its ratio is below a threshold tr_2. This second step removes both very small echoes, which might have passed the first step, as well as echo regions with implausible geometries like spokes (due to interferences from other emitters) or anaprop (if restricted to a few azimuth angles).

Parameter Study

In the study undertaken here, before the filter could be applied to the radar data, its parameters needed to be adjusted to the site. This was necessary, because some intensive convective cells were identified as clutter when the parameter set given in Gabella and Notarpietro (2002) was used. The study was conducted as follows, using the concept of a truth map (c.f. Kessinger et al. (1997)). In several radar images, three regions were classified according to the main clutter identification process.

The method will be explained in the following with an example radar image as presented in fig. 2.2a. Two regions of false alarms were identified. The first, marked red in fig. 2.2b are regions of high reflectivity, which are assumed to be meteorological, but where the original parameters had been identifying clutter. The second region, present in fig. 2.2b only as a small green spot at the upper edge, was used to determine false alarms due to the second step of the filter identifying small features as clutter, which could however be confirmed to be meteorological echoes due to their temporal behavior. This was done in order to evaluate the trade off between the filter's ability to remove unwanted spokes and anaprop echoes and the removal of smaller cells. A third region, marked in blue in fig. 2.2b, determined areas where only clutter was expected, which would show the sensitivity of the filter. Areas, in which no decision could be made whether identifications would be correct or erroneous, were left unmarked and thus would not be accounted for in the evaluation.

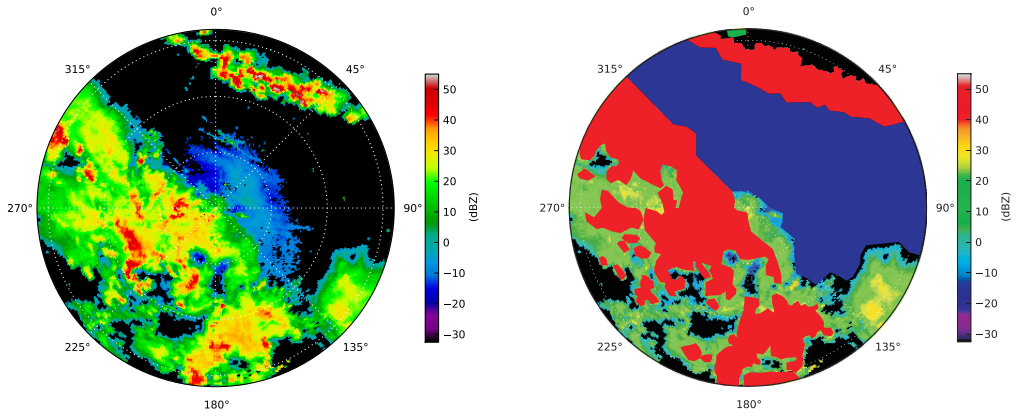

(a) original image **(b)** truth map

Figure 2.2.: Radar image and truth map for parameter performance comparisons

As it had been found earlier that the standard parameter set provided a very sensitive filter configuration, only parameter sets, which relaxed the filter were investigated, looking for a lower bound, which would lead to too much clutter passing the filter. After the regions had been determined in eight representative images, the filter was applied with different parameter sets. For each set and region the number of identified clutter bins was then counted. The parameter sets were then compared by ranking them according to their performance in each identification region. For example, if three parameter sets had produced 10, 20, and 30 counts in the blue region of an image and 10, 30 and 20 counts in the red region, they would have been assigned ranks 3, 2 and 1 for the clutter identification task and 1, 3 and 2 for not producing false alarms in high intensity regions. Assuming further that a parameter set had obtained ranks 1, 4 and 5 for its identifications in three blue regions of three different images, it would receive an average rank for the correct clutter task of 3.33. To obtain a decision, the average rank from all three regions was calculated. A set that had average ranks for the blue, green and red identification tasks of 2.5, 3.75 and 1.25 would receive a total average rank of 2.5. This way all three identification tasks could be given equal weight in the decision which parameter set to use.

Table 2.3 shows the results of the study. Columns FA-I and FA-S show the counts of false alarms due to intensity (red region in fig. 2.2b) and size (green region), respectively. Column CC shows the counts of correct clutter identifications (blue region). The individual ranks and the final rank are given in the remaining columns of the table. The individual ranks are averages over the ranks calculated for each truth-mapped image and not ranks based on the summary information in the count columns. The final rank is the average over the three individual ranks.

The table shows the behavior of the filter as expected from its definition. The increasing of the intensity threshold, tr_1, and the decreasing of the number threshold, n_p, lead to less false alarms due to intensity (column FA-I), and also lead to a decrease in regions with small image features. Reducing the area-circumference ratio threshold, tr_2, mainly affects the false alarm rate for small features and to a smaller

degree the correct detection of clutter (column CC).

The numbers in bold in the last four columns of table 2.3 indicate the parameter set with the best performance. It can be seen, that the set in the third row, proposed originally by Gabella and Notarpietro (2002) ($tr_1 = 6$, $n_p = 8$, $tr_2 = 1.3$) shows a good overall performance. However the parameter set $tr_1 = 12$, $n_p = 8$, $tr_2 = 1.05$ provides a better compromise between good detection power and lower false alarm rate and has the highest average rank. Therefore this set was chosen to do the identifications and corrections on which all subsequent results are based.

Table 2.3.: Comparison of different clutter filter parameters sets

tr_1	n_p	tr_2	FA-I	FA-S	CC	R (FA-I)	R (FA-S)	R (CC)	Rank
6	6	1.1	1140	1826	14622	4.06	6.62	8.12	6.27
6	6	1.3	1140	2847	14858	5.87	6.62	7.12	6.54
6	8	1.3	2058	3242	17944	8.62	7.25	**1.00**	5.62
8	8	1.3	1184	3169	16630	8.37	7.00	2.00	5.79
10	8	1.3	571	3120	16021	8.12	6.25	3.31	5.89
12	6	1.1	123	1618	12570	3.00	5.00	10.12	6.04
12	8	1.1	337	1987	15407	6.18	5.87	5.25	5.77
12	8	1.05	337	1858	15383	5.37	5.87	5.50	**5.58**
15	6	1.1	42	1581	12338	**2.75**	**4.75**	10.87	6.12
15	8	1.1	145	1911	15059	5.75	5.37	7.06	6.06
15	8	1.3	145	3067	15365	7.87	5.37	5.62	6.29

Identification Results

Fig. 2.3a shows the frequencies of detected clutter for the year 2008. The large number of identifications for some bins made it necessary to present them in $\log_{10}$ scale. The majority of high frequency bins lies within a range about 40 km from the radar (indicated by the first ring in the figure). The 45° orientation corresponds most likely to the rim of the Swabian Alb. A few spokes towards the north but more frequently to the south east were also identified by the filter. Also to the south east between 40 and 80 km are clutter echoes, which are probably due to the hills of the national park Augsburg Westliche Wälder.

Finally, the medium frequency detections up to 80 km should be discussed. The reason for this effect is presented in fig. 2.3b. During clear sky conditions almost all German weather radars show regions of increased reflectivity close to the radar. This effect is known as "German pancake" (Hassler et al., 2006). While the reason for its appearance is unknown, the signal provided is strong enough to trigger the first step of the clutter filter, especially along the rim of the pancake, which varies in extent, leading to the increase in detection frequency.

Correction

The next step after identification is correction. Ideally, bins identified as clutter should just be discarded and not be used for further analysis as correction inevitably

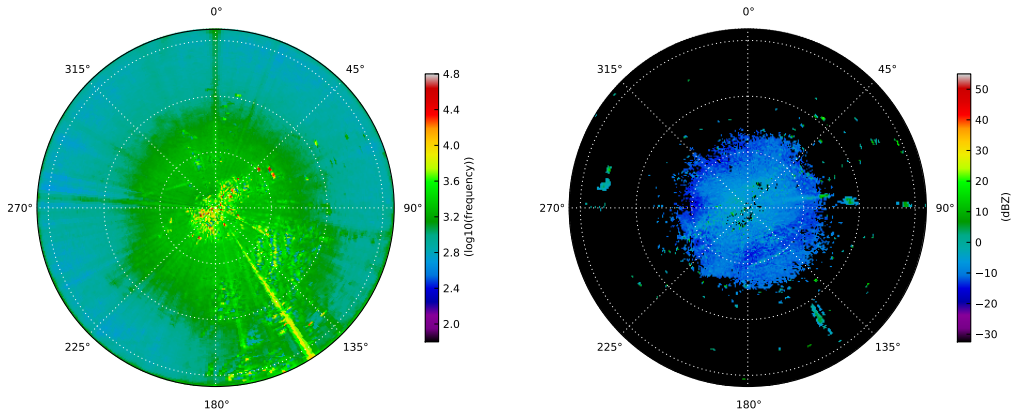

(a) clutter frequencies 2008 **(b)** Example 2008-06-01 12:15 UTC

Figure 2.3.: Clutter frequency enhancement due to "German Pancake" effect. (a) Clutter frequencies for year 2008, radar Türkheim, (b) Individual radar image with detected clutter

has to make assumptions, which, if not fulfilled introduce new errors into analyses based on the radar images. However, this is not always possible. Some algorithms used for advection estimation later in this thesis (see section 2.4) are unable to work with missing values. Hydrological models also need a definitive estimate of precipitation and likewise cannot deal properly with missing values. Therefore, the data needs to be corrected.

In addition, analyses of the corrected images give an overall indication on the effectiveness of the filter in addition to detailed verifications, similar to the parameter study presented above.

As the spatial extent of the majority of clutter is relatively small, virtually any interpolation method to infill the removed data should provide good results. In this study, the inverse distance weighting method (Shepard, 1968) was chosen as a compromise between speed and smoothness of interpolation. The faster nearest neighbor method may produce unreasonable results for larger areas of missing values (which may occur, however rarely). The additional time requirements of complex methods like spline interpolation or Kriging would not be warranted by the short distances and strong boundary conditions imposed by the surrounding valid data.

Figure 2.4 shows the accumulation of one year of precipitation data for the DWD radar site Türkheim. The color scale had been fixed for both images, obscuring part of the fact that the uncorrected image would have reported bins with accumulations up to 100000 mm in one year. The maximum reported accumulation in the corrected image is 1200 mm. In addition it can be seen that the filtering removed many of the intense spots to the south and also reduced the intensity of the positive spoke to the south east.

The filter yet fails to resolve two things: There are still bins which show high accumulations, which are clearly not plausible. The accumulations over the mountain ranges in the far south are much too small. This is most probably due to excessive suppression by a Doppler filter as mentioned in the introduction.

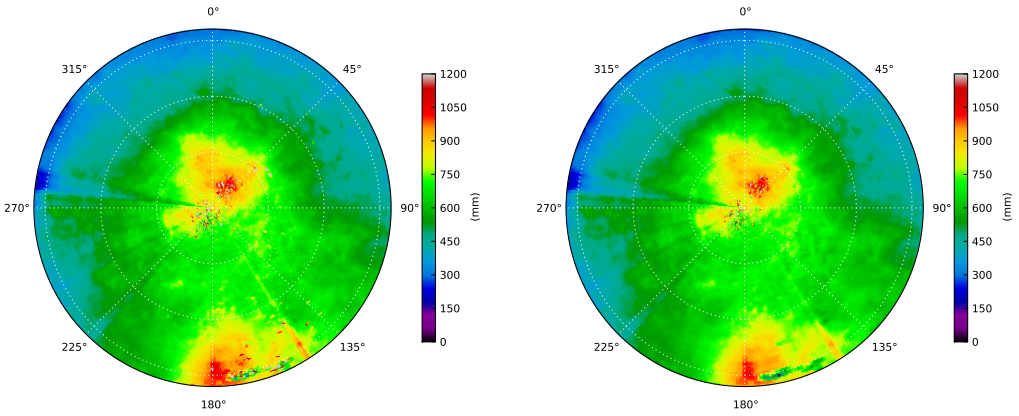

(a) uncorrected **(b)** corrected

Figure 2.4.: Effect of clutter removal. (a) Uncorrected accumulation for year 2008, radar Türkheim, (b) corrected accumulation

The remaining overestimations were analyzed with respect to two hypotheses. The first was whether these high accumulations were located at bins which had an already high clutter frequency. This could happen, for example, by a clutter bin being included in a precipitation field, where the intensity threshold of the clutter filter would not mark the bin as clutter, while the enhanced reflectivity would still lead to overestimation. To check this hypothesis, an empirical copula was constructed between the observed clutter frequencies and the accumulation. In short, both data were ranked, these ranks were normalized to the interval [0;1] and a 2-dimensional histogram was created from this transformed data. The result is shown in fig. 2.5.

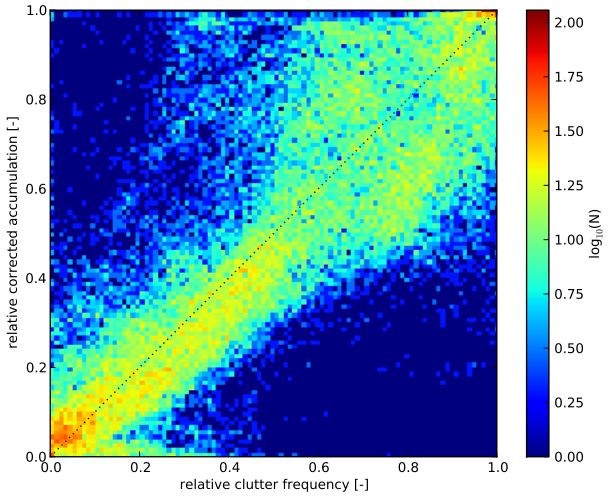

Figure 2.5.: Empirical Copula of annual accumulation vs. clutter frequency, radar Türkheim, year 2008

It can be seen that indeed most of the highest accumulations do have a high clutter frequency. However there are some bins, with both high accumulations and low frequencies and a broad range of accumulations with high clutter frequencies. This leads to the conclusion that, e.g., an additional threshold, which would lead to bins marked frequently as clutter being completely excluded might remove some of the residual clutter but would also remove many bins with possibly meteorological echoes.

Therefore a second hypothesis was tested, whether it was possible to remove the residual clutter by a static map.

This map was generated from corrected accumulations of the year 2007 and 2008. The two years were chosen to see if the static maps would change between years and whether this would make a difference in the correction. This map was created as a combination of the first step of the Gabella filter applied to the corrected accumulation, combined with a clutter map calculated by thresholding the difference between the corrected accumulation and its median filtered version.

The results of this additional static correction are shown in fig. 2.6. Both corrections remove additional implausible bins from the accumulation. Yet, still a number of implausible bins remain in both images. Comparing sub-figures (a) and (b) shows that the correction based on a static map of the same year (fig. 2.6b), yields better results than the static map of the previous year. The differences lie mainly over the mountain tops to the south and in the region of large accumulation to the north-east close to the radar.

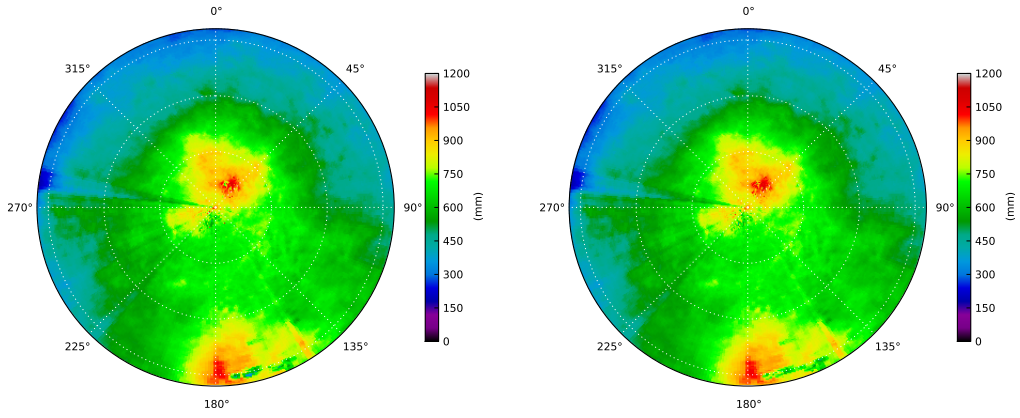

Figure 2.6.: Effect of additional static clutter map, accumulation for year 2008, radar Türkheim. (a) Corrected with static map of residual clutter of year 2007, (b) corrected using static map of residual clutter of year 2008

2.2.3. Summary

In this section, a method to remove clutter from individual radar images based on two-dimensional information only was implemented and tested on data for a period of one year with 5-minute resolution. The parameters were adjusted to avoid excessive

filtering during strong convective episodes, which may lead to some residual clutter still being present in long term accumulations.

Two approaches were investigated to remove this residual clutter. The empirical copula of residual clutter vs. accumulation does not show a clear dependence that could be exploited. Static maps identified from the residual clutter show some value in removing parts of the residual clutter, with maps based on more recent accumulations performing better than maps based on older data.

This has implications both for operational uses of static maps as well as reanalysis studies. For the former case, care has to be taken, to provide regular updates of the static maps. A more in-depth analysis would have to find the optimal length of an accumulation to produce the best static map. In the latter case, it could be worthwhile to recalculate clutter maps and corrections for historic radar images and not rely just on operational corrections. However, static maps are only useful as long as regions of clutter are still limited in extent.

This is because correcting for clutter in larger regions by interpolation from surrounding pixels will most probably introduce artifacts into the precipitation estimates. If there are no other sources of information, like measurements from other elevation angles which are not affected by clutter, the region close to the radar should be treated with extreme care or not be used for analysis, even if that would mean that in some directions the first 40 km of a radar image might have to be removed from a data set, which would be the case for the radar Türkheim.

2.3. Attenuation

2.3.1. Introduction

Atlas and Banks (1951) showed that attenuation at wavelengths below 7 cm will lead to an apparent storm structure different from its real structure. The intensity maximum moves radially towards the radar, and analogously, isocontours of intensity would appear more packed towards the near side of the storm. They also state that this effect decreases when the distance to the storm increases compared to its depth. If radar data is to be used to derive parameters of spatial structure for geostatistical methods either for interpolation or simulation, uncorrected attenuation is likely to introduce errors in the structure estimates and all results based on those.

This change in structure also directly relates to underestimations of precipitation intensity and amount in the region affected by attenuation.

Similarly to Z-R relations, it was found that power law relationships would also describe the connection between attenuation and rainfall intensity or radar reflectivity factor. Battan (1973) gives several k-R relations of the form $k = \alpha R^{\beta}$.

Usually, the first paper cited when dealing with attenuation is that of Hitschfeld and Bordan (1954). It is rarely mentioned that the main aim of the paper was not to provide a method of correcting attenuation, but to show that doing so without very precise knowledge of the radar calibration constant in the correction formula, will quickly lead to errors much larger than if the data had not been corrected at all. Their conclusion was that wavelengths below 10 cm, which are progressively affected by attenuation, should not be used for quantitative precipitation measurements.

Figure 2.7 shows that most radars in the European network are operating at C-Band (with a typical wavelength of 5 cm) with a few exceptions in France and south-east Europe. This is most probably due to the reduced cost of installation and operation of C-Band as compared to S-Band radars and the higher sensitivity towards small and medium rainfall intensities, which are prevalent in the mid and high latitudes. However, the intense events leading to flash-floods will be affected by attenuation.

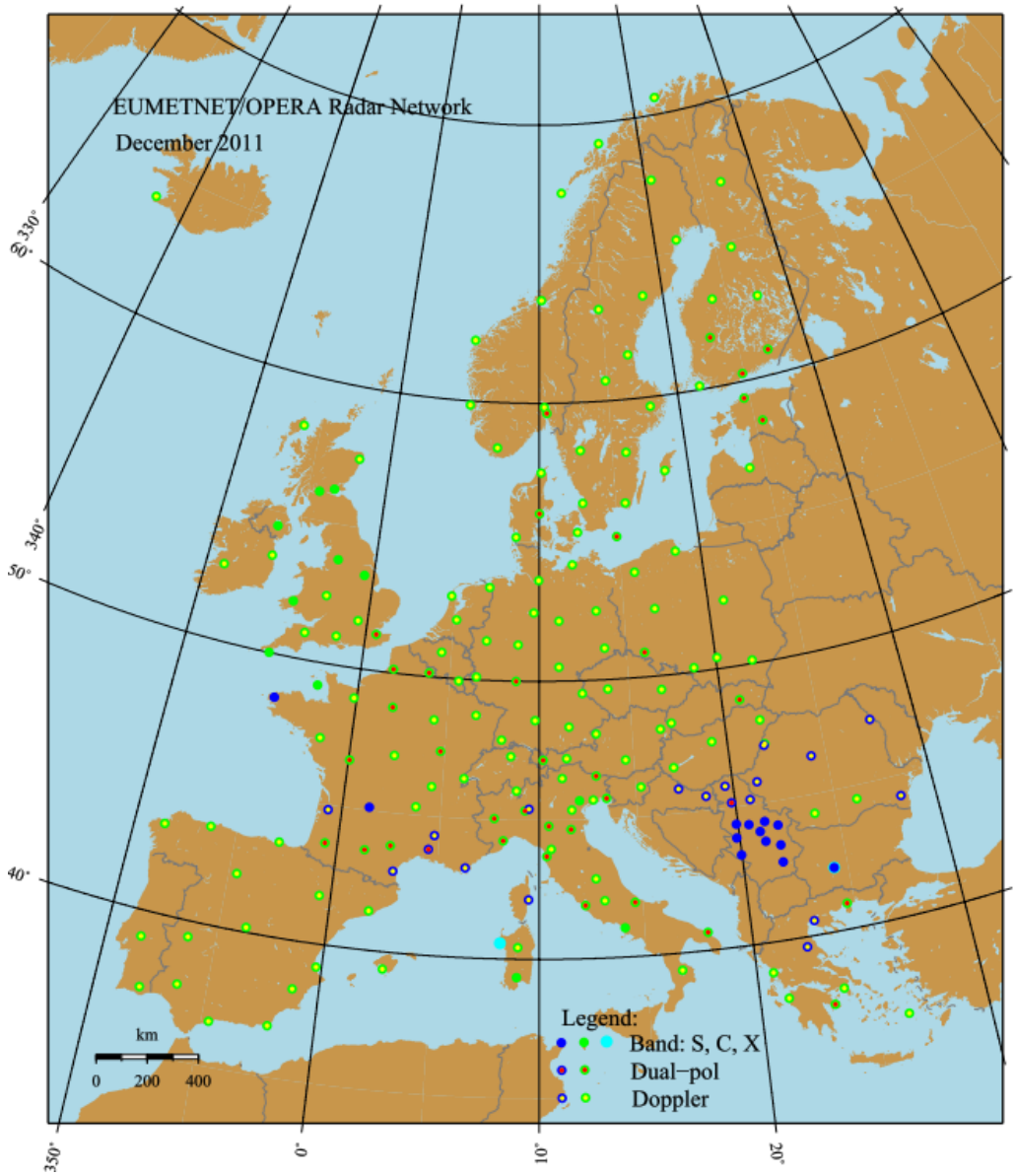

Figure 2.7.: Map of the European weather radar network
(source: OPERA project homepage, http://www.knmi.nl/opera/)

As will be explained in a later section, most gauge-adjustment techniques, which could be used to mitigate attenuation effects, assume a certain structure of the errors

corrected by the adjustment. This structure is assumed to be either completely isotropic, or at most an elliptical type of anisotropy is taken into account. The radial nature of the attenuation effect and its strong dependence on the intensities along the beam make this error behave very differently from these assumptions.

- The error is strongly dependent on intensity. Furthermore it is not dependent on the intensity at one location, but on the integral over the precipitation amount between the radar and that location.
- Therefore, the error is increasing radially outwards from the radar.
- The error is discontinuous azimuthally as it disappears as soon as the beam is no longer intercepting intense precipitation.

These properties make it unsuitable to correct for attenuation using e.g. simple bias adjustments but also more advanced geostatistical techniques. Therefore, it is the opinion of the author that attenuation correction should be attempted despite the warnings of Hitschfeld and Bordan.

While Hitschfeld and Bordan (1954) formulated their algorithm based on the rain rate, later algorithms focused on relationships between attenuation k and reflectivity Z. Depending on which of the two variables is assumed as the independent one, these relations are either termed k-Z ($k = \alpha Z^{\beta}$) or Z-k ($Z = \alpha k^{\beta}$) relation.

In order to avoid the divergence of the Hitschfeld and Bordan (HB) method, Hildebrand (1978) developed an iterative algorithm, starting out from an underestimate of the attenuation, which was shown to converge towards the true attenuation. The algorithm showed an improvement of precipitation estimates as long as the maximum attenuation was larger than the error in the radar calibration and the maximum reflectivity was below 60 dBZ. For the second case even this approach diverged and the algorithm had to be stopped at an earlier iteration.

When spaceborne radar was introduced, the need to correct for attenuation became more important as shorter wavelengths needed to be used due to size and power restrictions imposed by the operating conditions in space. Therefore several authors started to investigate the possibilities to correct these data for attenuation. Correction could be assumed to be more successful in this setting, as the earth's surface would terminate the beam and ideally provide a reference target, by which the total path integrated attenuation (PIA) could be determined. Meneghini et al. (1983) presented several methods to use the power backscattered from the surface to introduce factors to the radar calibration constant of Hitschfeld and Bordan (1954) or the linear factor of the k-R relation. They found that the version adjusting the calibration constant would lead to better results. However, their findings were based on idealized numerical calculations using a simplified atmospheric model. As the radar calibration factor is not known when data is obtained as reflectivity data (Z), modifying the linear factor of the k-R or Z-k relation, respectively, might be the only alternative for an end user.

Marzoug and Amayenc (1991) reformulated the HB equations to use reflectivity factors instead of rain rates. A big advantage of their method is that they managed to reformulate the recursive calculations of Hitschfeld and Bordan to a linear relation providing the specific attenuation of a radar bin based on apparent (i.e. attenuated)

reflectivities only. They provided several algorithms based on different amounts of knowledge of either PIA, initial attenuation (e.g. by a radome) or no additional information. They showed that the algorithm using no additional information would become unstable in the same way that the HB method would. However, if a reference for the PIA was available, their algorithm would become more and more stable and accurate with increasing precipitation intensity as opposed to the HB algorithm. Delrieu et al. (1997) tested and applied (Delrieu et al., 1999b,a, 2000) a method to use ground clutter returns to get an estimate of PIA by means of radar data only. Their approach uses two scans at different elevations to remove any signal caused by rain above the clutter bin. In addition it relies on data, which is unaltered e.g. by a Doppler filter as presented in section 2.2.1.

For the case when a PIA reference is not available, Nicol and Austin (2003) suggested the introduction of an adjustment parameter q, which could be tuned so that the attenuation correction would remain stable and a certain PIA would be achieved.

One problem for application of the Marzoug algorithms is, that they use a Z-k relation instead of a k-Z relation. For these relations, parameters must be determined either empirically or using backscattering models based on certain assumptions on the drop size distribution. These parameters are dependent on the wavelength and were calculated for X-Band and shorter wavelengths only, as these bands are predominantly used in satellite radar systems. As the radar data available for this study comes exclusively from C-band systems, the Z-k parameters needed to be determined before this method could be used for attenuation corrections at the 5 cm wavelength. While k-Z parameters can be found in the literature (e.g. in Krämer (2008) or Battan (1973)), due to their empirical nature and the poor log-log linearity of the relation (Delrieu et al., 1999a), these cannot simply be inverted without introducing large errors.

2.3.2. Constrained Forward Correction

Therefore, for this study a modified version of the method presented in Krämer (2008) was used to correct the data for attenuation. Krämer (2008) had investigated the variations of the parameters in the k-Z relation based on a recursive HB calculation and PIA reference measurements provided by a microwave link that had been installed co-radially with an X-Band radar close to Essen (Germany). Based on his results, he proposed a scheme to stabilize the HB algorithm by fixing the exponent of the k-Z relation and reducing the linear parameter, whenever the correction would produce corrected reflectivities beyond 59 dBZ until this threshold was no longer exceeded. In addition to the parameters at X-Band, k-Z parameters were also given for C-Band and example corrections were done with an operation DX dataset from the DWD radar site Essen, which is similar to the data used throughout this study. Jacobi et al. (2011) also used this approach but added an additional constraint that would limit the PIA to a maximum of 20 dBZ, with the linear factor of the k-Z being further reduced if this constraint was not met. Other parts of the Krämer algorithm, like the limitation to a minimum sector size, and the infilling of PIA references to sectors smaller than this minimum size and a subsequent backward correction were not implemented.

In short, the Krämer algorithm is based on a k-Z relation of the form

$$k = \alpha Z^{\beta} \tag{2.16}$$

which gives k in [dB/km] while Z needs to be given in linear units of $[mm^6/m^3]$. The recursive correction formula, calculating the actual reflectivity Z_i from the apparent (i.e. measured) reflectivity $Z_{a,i}$ at the range bin i is then

$$\begin{aligned} Z_i &= Z_{a,i} \cdot \prod_{j=0}^{i-1} 10^{k_j/10} \\ &= Z_{a,i} \cdot \prod_{j=0}^{i-1} 10^{\left(\alpha Z_j^{\beta}\right)/10} \end{aligned} \tag{2.17}$$

For numerical reasons, these calculations are usually done in decibel(dB)-space, which also simplifies the product to a summation

$$dBZ_i = dBZ_{a,i} + \sum_{j=0}^{i-1} \alpha \left(10^{dBZ_j/10}\right)^{\beta} \tag{2.18}$$

Fig. 2.8 shows the effect of the attenuation correction on a long term accumulation. As expected the amounts are increased everywhere. Most notable is the increase towards the south where the Allgäu Alps are located. According to Frei and Schär (1998) this area should provide an annual total between 4 and 5 mm/day, which would amount to a total accumulation between 1460 and 1825 mm, which is more realistically approached by the attenuation corrected accumulation. Some of the residual clutter, including the spoke to the southeast, however also gets increased. Although this shows the importance of proper clutter filtering, on the other hand, a radial accumulation bias due to an intensive clutter pixel is not seen in the figure.

Fig. 2.9 presents differences and ratios between the accumulations displayed in figs. 2.8a and 2.8b. While it can be seen in fig. 2.9a that the maximum accumulated correction amounts to approximately 300 mm for the year 2008, fig. 2.9b shows that the relative change increases radially, as expected, reaching its maximum in the regions of lower total accumulations in the northern semicircle, where the average correction is about 20-30%.

Both figures show that the two constraints are apparently effective in preventing gross overestimation while also, on average, limiting the amount of correction to reasonable values.

Another comparison was made on the hourly timescale. For this purpose hourly data from a set of ca. 340 operational gauging stations provided by the DWD were compared with hourly accumulations of clutter and attenuation corrected radar data for a period of 3 months between May and July 2008. This period comprises the event on 2nd of June, which led to devastating flash floods in the Starzel catchment (Ruiz-Villanueva et al., 2012). The stations were filtered to remove those which only sporadically provided data. It was found that 53 stations provided values for more than 95% of the time, while availability drastically decreased afterwards. In order to remove possible spurious correlations, the analysis was limited to these 53 stations.

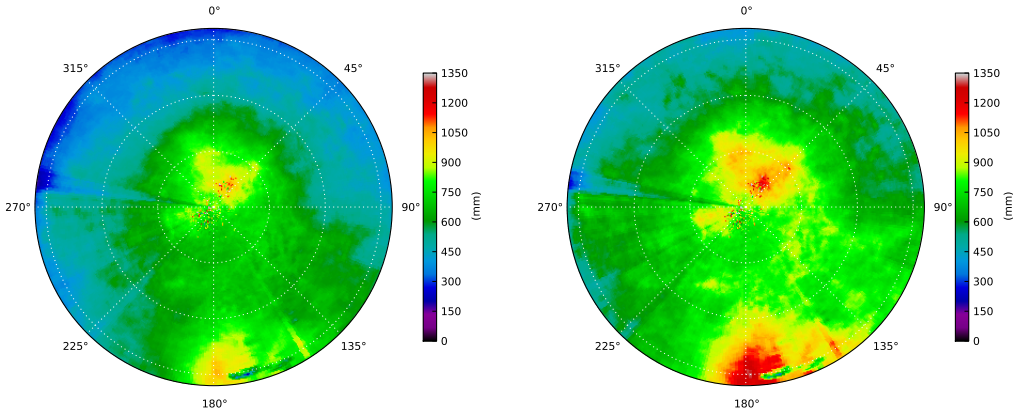

(a) uncorrected **(b)** corrected

Figure 2.8.: Effect of attenuation correction, radar Türkheim. (a) Accumulation for year 2008 corrected for clutter only, (b) clutter and attenuation corrected accumulation

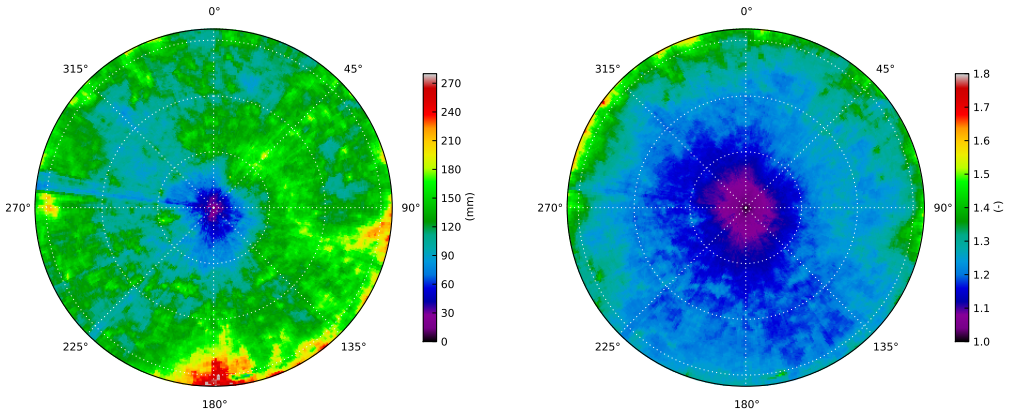

(a) difference **(b)** ratio

Figure 2.9.: Relative effects of attenuation correction, radar Türkheim, accumulation year 2008. (a) Difference between corrected and uncorrected (c.f. fig. 2.8) accumulation, (b) ratio between corrected and uncorrected accumulation

Fig. 2.10 shows a scatter plot of the uncorrected and the corrected data. It can be seen that the method effectively corrects the larger precipitation amounts towards a much better agreement between radar and gauge data. On the other hand, a tendency to overcorrect the small to medium intensity rainfalls is also apparent.

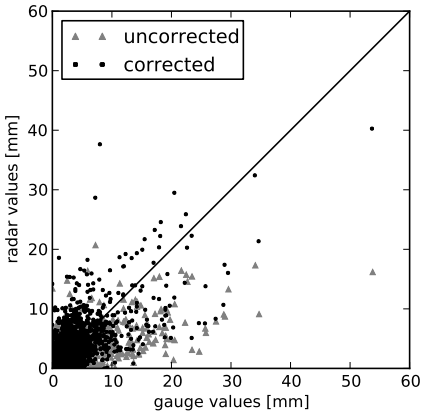

Figure 2.10.: Scatterplot of hourly accumulations for data corrected for clutter only (uncorrected) and corrected for clutter and attenuation (corrected), Radar Türkheim, May-July 2008

Tab. 2.4 gives some summary statistics based on the data presented in fig. 2.10. Both error measures slightly increase for the attenuation corrected data set in addition to a change in bias from underestimation to overestimation. The successful correction of the largest measurements is most likely the reason for the improved slope and correlation values.

Table 2.4.: Aggregate error measures for attenuation correction; agreement between hourly radar and gauge accumulations

	RMSE	MAE	bias	slope	correlation
uncorrected	0.463	0.061	0.859	0.531	0.774
corrected	0.485	0.075	1.238	0.780	0.798

To further assess the corrective performance of the method, fig. 2.11 shows the distribution of several error and goodness-of-fit measures. Figs. 2.11 (a) and (b), show the distribution of RMSE and MAE, with RMSE being chosen as a standard measure of error and MAE because it is a bit less susceptible to outliers than RMSE.

For figs. 2.11 (c) and (d) the difference between corrected and uncorrected RMSE and MAE, respectively, was taken and again the resulting distribution was plotted. In panels (c) through (f) of fig. 2.11 a negative value implies an improvement, while a positive value means that the 'correction' actually makes things worse. Fig. 2.11c shows that improvement only for roughly a third of the stations, while there is no improvement for the others. The MAE-difference in fig. 2.11d only shows improvement for one station. This is most probably due to the greater relative weight that many small to medium deviations get during the calculation of MAE.

Two additional measures of agreement were calculated and are shown in figs. 2.11 (e) and (f). Bias was calculated as the ratio between the mean of the radar data and the mean of the gauge data. Slope represents the slope of a linear regression between gauge and radar data, with the gauge data being the independent variable. The change between uncorrected and corrected radar data was calculated according to

$$\delta = |1 - b_c| - |1 - b_u| \tag{2.19}$$

with b_c being the value for the corrected and b_u the respective value for the uncorrected data. As both bias and slope should be 1, eqn. 2.19 shows an improvement as a negative value and a worsening as a positive value. It does not make a statement whether an underestimation is still an underestimation or whether there has been a more profound change to the dependence. However, this can be assessed using the other measures and the scatterplot.

Together with MAE-difference, the change in Bias, which also worsened for about two thirds of the data this shows that there is overcorrection in the majority of cases. The major improvements in terms of slope change, may on the other hand be attributed to the successful correction at larger intensities.

In summary, the attenuation correction has shown its potential in correcting intense precipitation, while the constraints imposed on the correction prevented large overcorrections. However, the method does overcorrect for small to medium intensities, leading to increased absolute errors and biases as compared to uncorrected radar data. Further refinements of the method are possible and should focus on removing these biases.

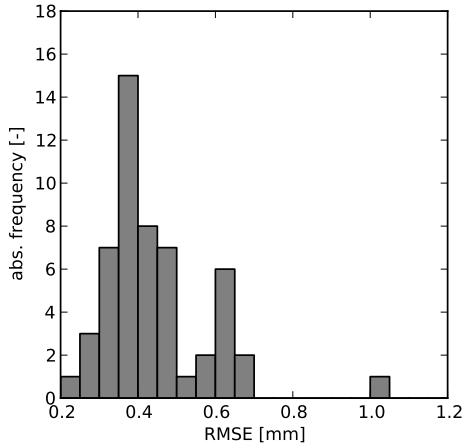

(a) RMSE

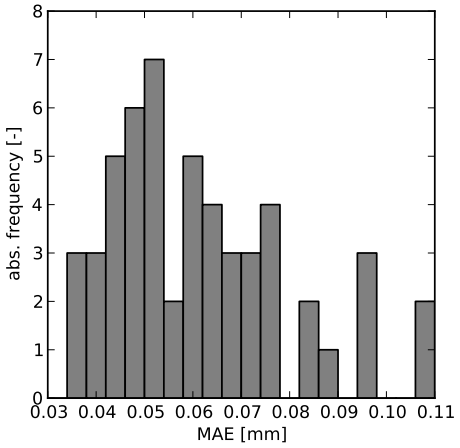

(b) MAE

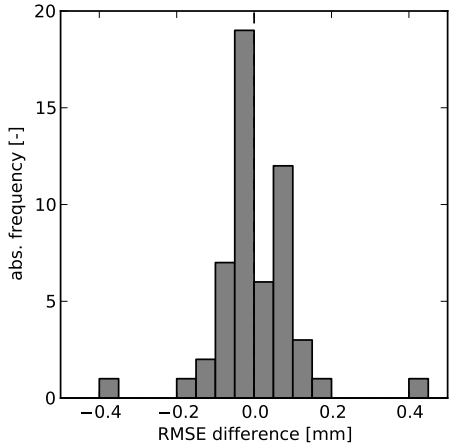

(c) RMSE-difference

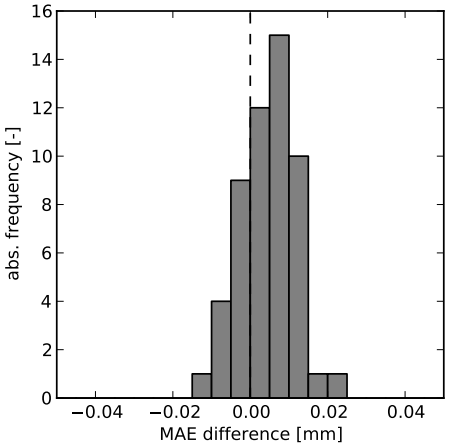

(d) MAE-difference

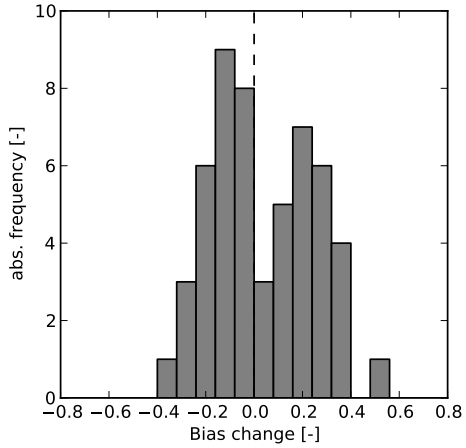

(e) Bias

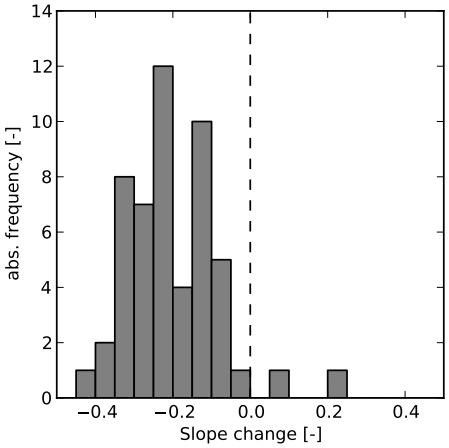

(f) Slope

Figure 2.11.: Distribution different error measures and their changes due to attenuation correction

2.4. Advection

2.4.1. Introduction

Weather radar scans are generally viewed as snapshots of the precipitation field of a certain point in time. Looking at it more closely, a full rotation of an antenna takes about 20-30 s. If a volume scanning strategy is employed it can take 5-15 minutes until the antenna returns to the same elevation angle. During this time, the precipitation field has moved, driven by the wind and changed according to the processes of cloud evolution. If winds are sufficiently strong, the precipitation field will have moved a considerable distance, e.g. a wind speed of 20 m/s would lead to a displacement by 6 km within 5 minutes.

It is common practice to accumulate radar data to hourly resolution before comparisons with rain gauges are made. This is done in general by simply adding up the rainfall depth information of the individual images. When a field is moving fast, an effect as shown in fig. 2.12a will be observed. The rainfall accumulation seems to have a ripple like structure due to the large displacements of the rainfall in between images. This is not only visually unsatisfying but it may also lead to errors in radar-rain gauge comparisons or geostatistical analyses of the spatial structure of the rainfall field.

Advection fields derived from radar imagery have been used to analyze storm motions (Rinehart and Garvey, 1978; Tuttle and Gall, 1999) or the lifetime of vortices (Trier et al., 2000). The advection fields may also be used to do short term forecasts or 'nowcasts' of precipitation (Turner and Zawadzki, 2010; Berenguer et al., 2011; Bowler et al., 2006; Saxen et al., 2008; Bowler et al., 2004; Ehret, 2003; Sinclair, 2007), where they show better skill than numerical weather prediction models up to lead times of approximately 6 hours (Ebert et al., 2004; Pierce et al., 2004; May et al., 2004; Turner and Zawadzki, 2010).

As mentioned before, correcting accumulations by taking advection into account should lead to a more realistic estimation of the spatial structure of the total precipitation, by improving the discrete sum to better approximate the continuous integration it would be in reality. Therefore, it should also improve the agreement between radar and rain gauges.

In this section, first, three different algorithms are investigated with respect to their accuracy and robustness to the choice of configuration parameters. Second, an analysis of the improvement of radar-rain gauge agreement by using advection information will be presented. A first visual impression of the effect of advection-aware accumulation is given in fig. 2.12.

2.4.2. Comparison of Advection Estimation Algorithms

Block Matching

The Block Matching (BM) technique is one of the simplest ways to determine the movement of objects between two images. First, the initial image is divided into blocks of a certain size, which may overlap. Then, for each block in the previous image, the current image is searched for the block that would provide the best match. This match is usually found by calculating the correlation between the image inten-

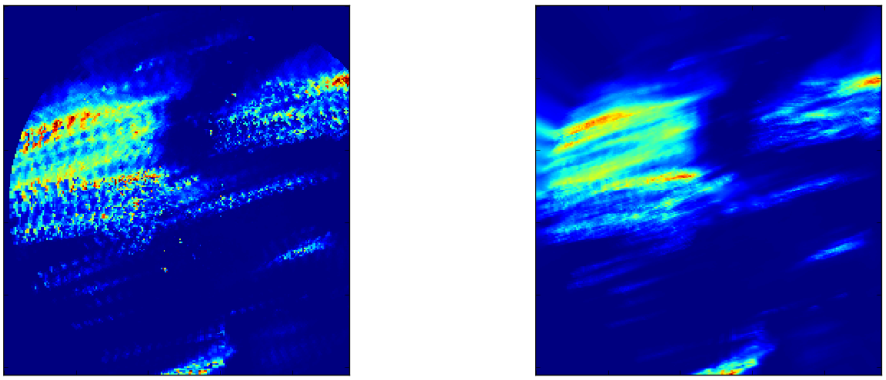

(a) simple accumulation **(b)** advection-aware accumulation

Figure 2.12.: Qualitative comparison between simple and advection-aware accumulation; Radar Dresden, 2008-06-23 01:50–2008-06-23 02:50 UTC

sities of the respective blocks. The vector from the previous image's block centre to the centre of the matching block becomes the previous block's advection vector estimate. This approach has been used in the TREC method presented by Rinehart and Garvey (1978). Performance, both in terms of speed and detection quality is affected by three parameters: The size of the blocks (bs) determines the ability of the approach to resolve small scale movements in an image. The larger the blocks, the less likely it will be to find a matching block, if not all parts of the image move in the same direction. On the other hand, if the block size is chosen too small, correlations might become unstable, leading to erroneous matchings. The shift size (ss) determines how fine the image will be sampled for advection vectors. Together with the block size, this parameter specifies the amount of overlap between blocks in the previous image. It does not have any influence on correct or incorrect estimates but increases the number of calculations per image and thus negatively affects the speed of the estimation. The third parameter is the maximum search range (mr). Choosing this parameter too small will result in blocks being missed, if the displacements between the two images were larger. Choosing it too large will result in longer searches and, occasionally, mismatches, if there are several similar features within an image.

In order to produce a displacement vector for each image pixel, in principle a shift size of 1 would have to be used. As this would have made calculation prohibitively slow and assuming a certain degree of smoothness (which may be justified by intuition as well as e.g. fig. 2.13), advection vectors at remaining pixels were calculated using inverse distance interpolation.

Fig. 2.13 shows a typical example of an advection retrieval using the block matching method. The calculated advection vector fields are the same in both panels while the background shows the radar reflectivities 5 minutes apart from each other.

The quality of the advection estimate can already be assessed to some degree by these images. If a feature is only advected but does not evolve, the start of a displacement arrow in the left hand image and its tip in the right hand image should be at the same location of a feature. This is more easily seen with the borders of the fields displayed in the figure.

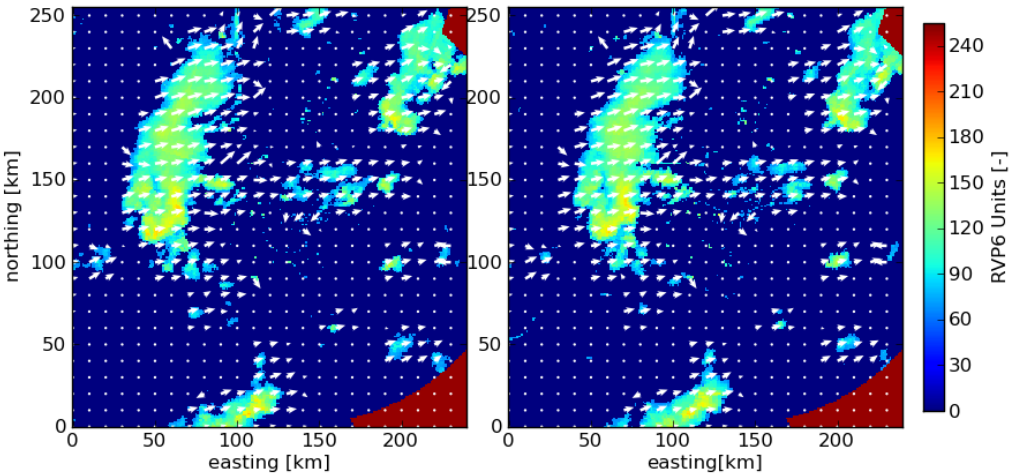

Figure 2.13.: Advection field estimated by the Block Matching method; Radar Dresden; 2008-06-23 02:20 UTC (left) 02:25 (right); Parameters: block size 20x20, shift size 5x5, maximum range 10x10 pixels

Another property of the block matching method is, that it will produce zero advection in areas where it is not raining. This is a direct result of the matching procedure which will match non-raining blocks without searching any further. For this reason, the TREC method could only be used to analyse internal storm motions.

Optical Flow Using Intensity Gradients Only

Horn and Schunck (1981) developed an method to calculate optical flow based on assumptions on the temporal development of intensity patterns in an image and smoothness constraints for the flow field.

Based on the assumption that the brightness intensity (I) of the pixels representing an object in an image would not change over time

$$\frac{dI}{dt} = 0 \tag{2.20}$$

using chain rule derivatives

$$\frac{\partial I}{\partial x}\frac{\mathrm{d}x}{\mathrm{d}t} + \frac{\partial I}{\partial y}\frac{\mathrm{d}y}{\mathrm{d}t} + \frac{\partial I}{\partial t} = 0 \tag{2.21}$$

and by identifying $\frac{\mathrm{d}x}{\mathrm{d}t} = v_x$ and $\frac{\mathrm{d}y}{\mathrm{d}t} = v_y$ they could find a direct functional relation between spatial and temporal gradients in the images and the velocity field observed by them.

An additional constraint was necessary to fully define the two unknowns v_x and v_y, which had been defined by one equation so far. This constraint was chosen such that the velocity field would vary smoothly in space, which could be realized by minimizing the squared sum of partial derivatives

$$\left(\frac{\partial v_x}{\partial x}\right)^2 + \left(\frac{\partial v_x}{\partial y}\right)^2 + \left(\frac{\partial v_y}{\partial x}\right)^2 + \left(\frac{\partial v_y}{\partial y}\right)^2 \tag{2.22}$$

If an objective function ε^2 is defined such that:

$$\begin{aligned} \varepsilon_b &= \frac{\partial I}{\partial x} v_x + \frac{\partial I}{\partial y} v_y + \frac{\partial I}{\partial t} \\ \varepsilon_c^2 &= \left(\frac{\partial v_x}{\partial x}\right)^2 + \left(\frac{\partial v_x}{\partial y}\right)^2 + \left(\frac{\partial v_y}{\partial x}\right)^2 + \left(\frac{\partial v_y}{\partial y}\right)^2 \\ \varepsilon^2 &= \iint \left(\frac{1}{\lambda_s^2}\varepsilon_c^2 + \varepsilon_b^2\right) \mathrm{d}x \, \mathrm{d}y \end{aligned} \tag{2.23}$$

minimizing ε^2 leads to estimates of v_x and v_y.

For this study, the implementation, which is part of the Open Computer Vision (OpenCV) library (Bradski and Kaehler, 2008) was used. This implementation is governed by three major parameters: The first parameter λ_s controls the importance given to the smoothness constraint (eqn. 2.23). The second parameter(mi) gives the maximum number of iterations allowed to the algorithm to satisfy the smoothness constraint. The window size of an averaging preprocessing, which is recommended in the original algorithm description to treat large displacements in an image correctly, is the third parameter, whose influence on the velocity estimates was investigated.

This algorithm, is the basis of the optical flow calculations for the STEPS nowcasting suite (Bowler et al., 2004, 2006), and will be denoted HS in the following.

While the method is mathematically elegant and also computationally efficient, it appears to be quite sensitive to the choice of parameters. This is exemplified in figs. 2.14 and 2.15. In fig. 2.14 minimal smoothing has been applied to the image before advection estimation and during estimation little weight is given to the smoothness constraint. Consequently, the estimated advection vectors seem to be pointing into arbitrary directions with unrealistic magnitudes as well. Fig. 2.15 shows the other extreme of parameter choice with intensive smoothing, large weights to the smoothness constraint and many iterations. The advection field looks much smoother and more realistic. However, it should be noted that the vectors appear to be gradually increasing in magnitude from outside a precipitiation field towards the inside. This would lead to a divergence of the precipitation field, which is not observed in reality. In addition, the vectors are generally too small in magnitude. A translation of the left image by the advection field would not be able to recreate the main features of the right image.

The HS method also seems to be able to detect motion only in places where there is an intensity gradient. Although it is argued in the original paper, that the iterative solution to the smoothness constraint should propagate velocities from regions with non-zero intensity gradient information to zero-gradient regions, this is apparently not the case for the OpenCV implementation.

Optical Flow Using Gradient Information on Several Image Scales

This algorithm was presented by Bouguet and Others (2000) and is based on a method developed by Lucas and Kanade (1981).

The Lucas & Kanade (LK) approach was initially developed for application in stereo-vision to register features in images, which had been acquired by two cameras from different viewing angles. In its full form, the method is even able to detect not

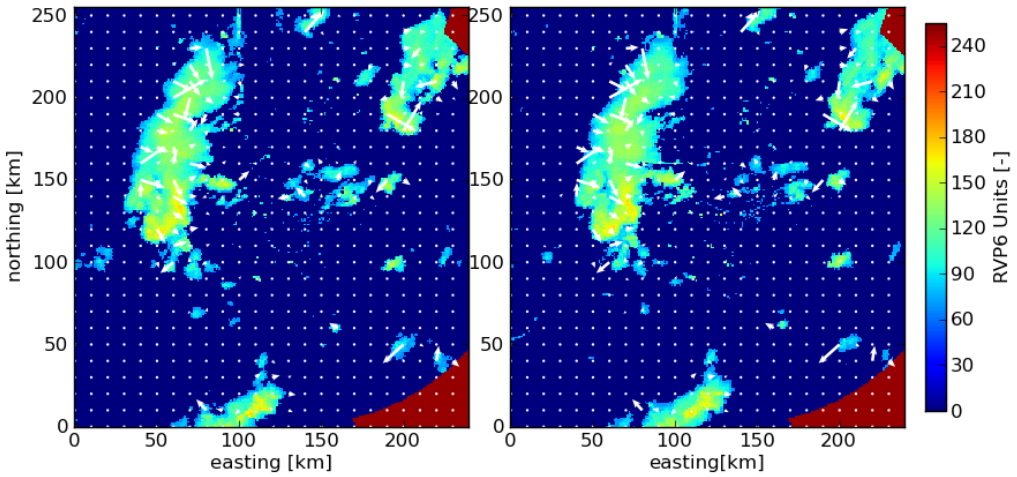

Figure 2.14.: Advection field estimated by the Horn & Schunck method; Radar Dresden; 2008-06-23 02:20 UTC (left) 02:25 (right); Parameters: λ_s 0.1, max. iterations 128, no smoothing

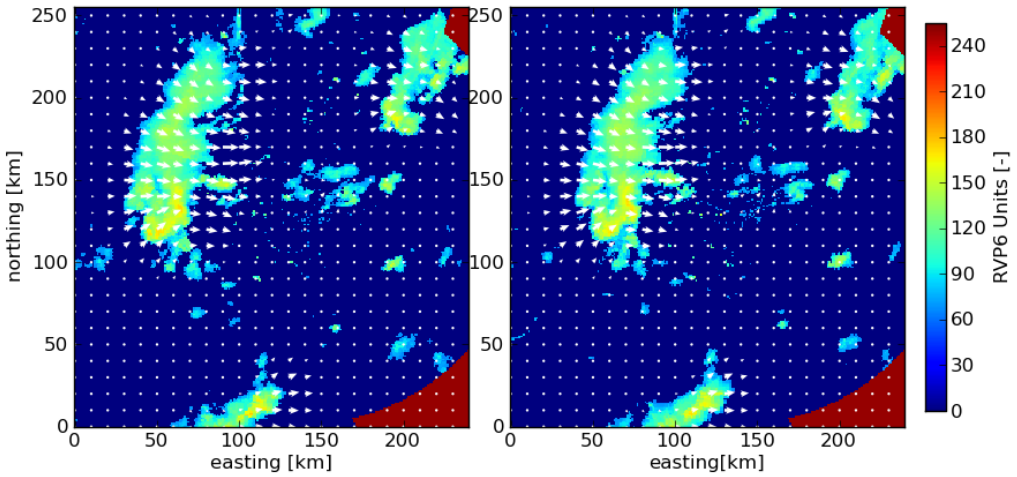

Figure 2.15.: Advection field estimated by the Horn & Schunck method; Radar Dresden; 2008-06-23 02:20 UTC (left) 02:25 (right); Parameters: λ_s 0.001, max. iterations 512, smoothing by 33x33 pixel window

only translations but arbitrary linear transformations including rotation, scaling and shearing of features between two images. However, using only the translation part makes the method suitable for optical flow detections as well.

Given two images $F(x)$ and $G(x)$, the algorithm searches for the displacement h such that $G(x) = F(x + h)$. For the case that h is small, the authors show that h can be estimated iteratively using

$$\begin{aligned} h_0 &= 0 \\ h_{k+1} &= h_k + \frac{\sum_x w(x)F'(x + h_k)[G(x) - F(x + h_k)]}{\sum_x w(x)F'(x + h_k)^2} \end{aligned} \tag{2.24}$$

with the weights $w(x)$ defined as

$$w(x) = \frac{1}{|G'(x) - F'(x)|} \tag{2.25}$$

and $F'(x)$ and $G'(x)$ being the derivatives of F and G calculated by finite differences.

Bouguet and Others (2000) implemented a hint in the original paper, that estimates of h at coarser aggregation scales may be used as first guesses for the search at finer scales down to the original image resolution. This concept of resampled images at different aggregation levels is called 'pyramids' in the image processing literature. Therefore, the algorithm has been denoted PyrLK (Lucas & Kanade with Pyramids) in the OpenCV library, from where its implementation has been taken, which will also be used as abbreviation for it in this thesis.

The PyrLK algorithm is different from the preceding two in that it does not calculate advection vectors for each image pixel (in the case of the HS method) or a regular set of blocks (as with BM). A preprocessing step first chooses points for which the LK algorithm is more likely to converge. These are usually features with high intensity gradients. Then, the displacements are calculated only for these points. In order to obtain information for the whole field, the results at the points were interpolated using inverse distance weighting. This approach has the advantage of immediately creating smooth advection vector fields, which also extend into zero-rain regions, which can be seen in fig. 2.16.

For the parameter sensitivity study three main parameters were chosen for comparison. The window size (ws) determines the number of pixels, which are aggreated for each pyramid level. The larger this size is, the quicker the resolution decreases with each step, allowing larger features to be identified but also reducing the number of levels that can be meaningfully used. The second parameter was the number of maximum iterations (mi) allowed to the Lucas & Kanade part of the algorithm to converge to the final displacement vector. Finally, one parameter from the preselection step was analyzed, which determined the minimum distance (md) that selected points must have to all other points in order to be valid candidates.

Parameter Sensitivity

In an operational environment it is very important that an algorithm not only provides the best results. It must also be robust in the sense that it would produce very bad results as rarely as possible. An algorithm that provides good results in

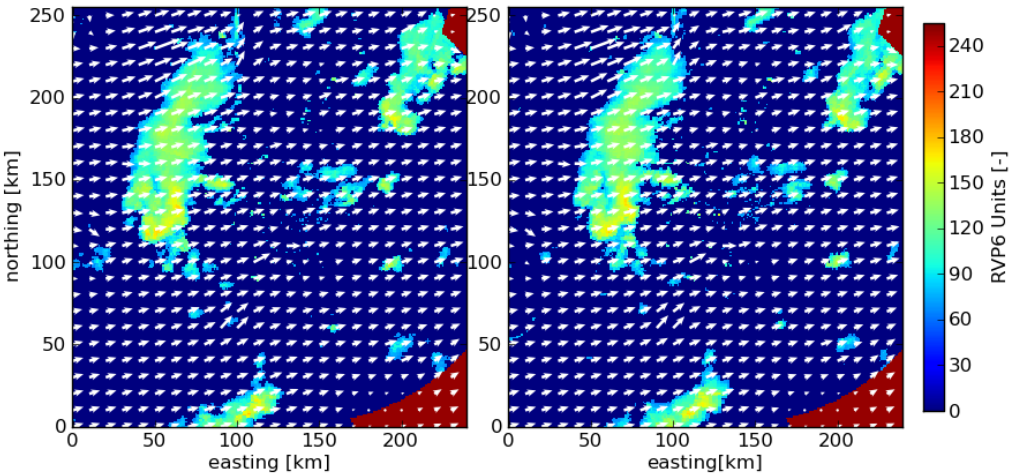

Figure 2.16.: Advection field estimated by the Lucas & Kanade with Pyramids method; Radar Dresden; 2008-06-23 02:20 UTC (left) 02:25 (right)

all cases may therefore be preferable to the algorithm that provides the best results, but which fails completely from time to time.

For this comparison a 1 hour dataset based on rasterized reflectivity data for the radar site Dresden was analyzed by each algorithm using a choice of parameter settings as described above and displayed in appendix A. The dataset consisted of the period displayed in fig. 2.12, which can be characterized by fast storm motion with moderate development between images. This is one of the most ideal cases as features show a considerable movement, which can be clearly separated from the development of the individual storm cells. Therefore spurious detections mistaking development for movement should be as small as possible.

For each successive image pair in the dataset and each parameter combination, advection fields were estimated by the three algorithms. Afterwards, the earlier image of each pair was advected using the estimated field and the advection method described on page 37. This advected field was compared to the later image of each pair calculating the mean absolute error (MAE) and the root mean square error (RMSE).

Tables 2.5 and 2.6 summarize the aggregate statistics over all analyzed image pairs and parameter combinations. They show that the PyrLK method performs best with respect to most statistics providing the lowest average errors with the smallest spread. Especially notable is the negative skew in RMSE of the PyrLK method. This can be interpreted that this method tends to produce outliers more toward low errors than high errors, i.e. tends to be less prone to total failure. Appendix A gives more detailed information on the behavior of each method with respect to different parameter sets.

In summary, the PyrLK method produces the lowest average error when advected images are compared with radar images of the next time step. In addition the algorithm appears to be completely insensitive within the range of all three tested parameters. This makes the method extremely robust, which would make it a good

Table 2.5.: Summary statistics of mean absolute error

Method	Min	Max	Median	Mean	Std	Skew
BM	20.586	92.874	29.841	33.079	16.345	2.828
HS	19.025	36.938	26.529	27.113	4.584	0.027
PyrLK	16.243	26.136	20.699	21.544	3.076	0.010

Table 2.6.: Summary statistics of root mean square error

Method	Min	Max	Median	Mean	Std	Skew
BM	3.787	6.420	4.835	4.858	0.533	0.602
HS	3.228	5.161	4.191	4.234	0.454	0.045
PyrLK	3.261	4.091	3.850	3.743	0.289	-0.345

choice for operational applications. While some of the errors produced by the HS method are smaller, they appear to be mainly artifacts when compared with the result of the parameter combination presented in fig. 2.14. The BM algorithm performs slightly worse than the HS method with some extreme outliers.

2.4.3. Advection-Aware Accumulation

One problem that arises when accounting for advection during accumulations is that not only does the field move, it also evolves. Therefore the initial image may not just be translated forward in time, somehow the changes in intensity between the two time steps must be taken into account as well. A simple way to do this, is to not just translate the initial field forward in time and accumulate its contributions, but to also translate the later image backwards in time and to weight each contribution according to its temporal distance from its respective original field.

This approach leads to the advection-aware accumulation A_v as calculated according to equation 2.26.

$$A_v = \frac{1}{\sum_{i,j} w_{i,j}} \sum_{j=0}^{n} \left[w_{0,j} \cdot \mathrm{adv}\left(I_{t_0}, \vec{v}, j \cdot dt\right) + w_{1,j} \cdot \mathrm{adv}\left(I_{t_1}, -\vec{v}, j \cdot dt\right) \right] \tag{2.26}$$

with $dt = (t_1 - t_0)/n$. The advection function $\mathrm{adv}\left(I_{t_i}, \vec{v}, \Delta t\right)$ provides the translation of the pixel intensity information contained in image I_{t_i} taken at time t_i to new pixels according to the advection field $vecv$ and the time span Δt. The weights are defined as $w_{i,j} = 1 - j/n$.

Figure 2.17 schematically shows the weights given to the intermediate images generated by the advection function for a discretization of $n = 3$. All these images would then be summed up according to equation 2.26 to form the advection corrected accumulation for that time interval.

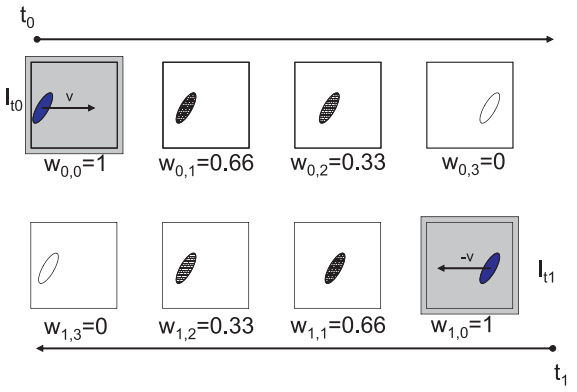

Figure 2.17.: Scheme of the weighted advection accumulation

Calculating Advected Fields Although it seems to be straightforward to calculate advected images from original images using advection fields, for the sake of completeness, the method used in this thesis should be explained.

Due to the way the advection fields are calculated, the correct way to calculate advected images is to translate each image pixel from the starting image to the advected image using the velocity vector given for that pixel. This can, however lead to some pixels in the advected image being assigned multiple values, either due to inconsistencies in the advection field, roundoff errors or actual or apparent convergent flows. Similarly, and consequently, some pixels may not be assigned any value for the same reasons.

Assuming that the advection field is *mainly* divergence free, a different approach may be used. This way, a pixel in the advected field is assigned the value from the pixel in the starting image to which this pixel's advection vector would point to if its direction were reversed.

More figuratively, the first method places the tail of the arrow representing the advection vector at each pixel in the original image and translates, or pushes, the intensity to the pixel at the tip of the arrow to create the output image. The second method places the tip of the arrow at each pixel and fetches, or pulls, the intensity from the pixel in the original image at the tail of the arrow, assigning this value to the pixel of the output image.

The second approach has the advantage of definitely assigning a value to each pixel in the output image. It works under the assumption that the advection field is spatially homogeneous in the sense that direction and magnitude doesn't change much over distances on the order of the advection vector's magnitudes. Some pixels in the original image may be used more than once, or be ignored but the method is computationally much more tractable without having to interpolate, to place additional, very strong constraints on the advection estimation or to devise complex search and decision algorithms to fill missing pixels and to deal with multiple assignments. Therefore, the second approach was chosen for advection calculations.

2.4.4. Assessment of the Corrective Performance of Advection-Aware Accumulation

Based on the findings of the comparison of the different advection algorithms, the PyrLK method was chosen to do a long term estimation of advection fields. This was done for the same three-month period presented in section 2.3 on page 25.

First, clutter corrected hourly accumulations were compared with advection-aware accumulations based on the clutter corrected images. Fig. 2.18 shows a scatterplot between these two datasets when compared to gauge data. As can be seen in this plot, the changes due to the correction are relatively small, which was to be expected.

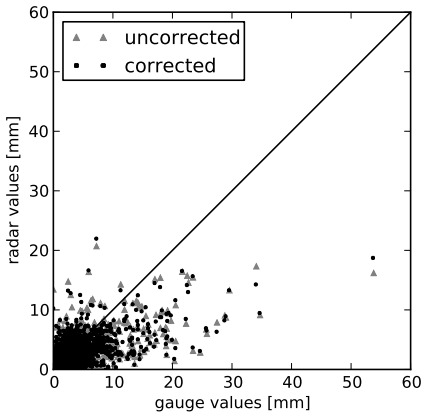

Figure 2.18.: Scatterplot between radar and gauge data for simple accumulations (labeled 'uncorrected') and advection-aware accumulations ('corrected')

Tab. 2.7 shows an aggregate analysis of the changes in radar-gauge agreement for all valid data pairs. While there is a slight increase in RMSE and MAE as well as a decrease in regression slope, the mean bias is improved as, however slightly, is the correlation.

Table 2.7.: Aggregate error measures for simple and advection-aware accumulation aggreement between hourly radar and gauge accumulations

	RMSE	MAE	bias	slope	correlation
simple	0.463	0.061	0.859	0.531	0.774
adv-aware	0.492	0.070	0.978	0.524	0.778

A more detailed analysis, similar to that of section 2.3 gives a more detailed representation of the changes in radar-gauge agreement due to accounting for advection. Figs. 2.19 (c) and (d) show that the correction worsens RMSE and MAE, respectively by roughly 10 to 20%. While bias is affected positively for the majority of compared gauges, the correction has a slightly negative impact on the estimated slope as can be seen in figs. 2.19 (e) and (f).

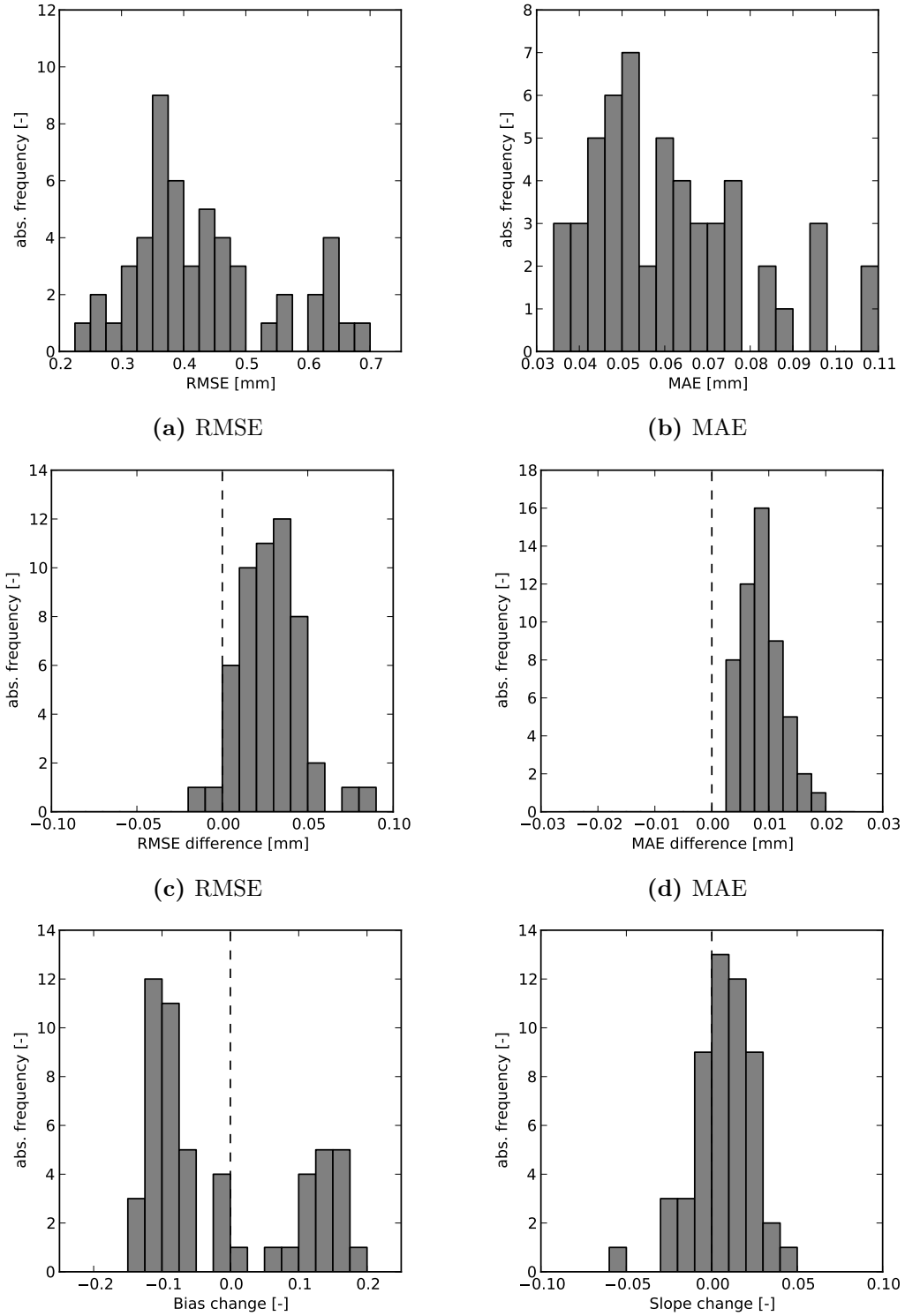

(a) RMSE **(b)** MAE

(c) RMSE **(d)** MAE

(e) Bias **(f)** Slope

Figure 2.19.: Distribution of changes in the different error measures

Summary

Three algorithms to determine optical flow in two subsequent images have been tested. Two algorithms, which have been in use for the estimation of advection from radar imagery, and a third one, which has shown to produce extremely robust estimates, which is most probably due to its strategy to analyze several aggregation scales instead of relying on only the original image pixels. Based on the estimates of this third algorithm it was tested, whether accumulation taking advection into account would improve radar-gauge agreement.

The effect was expected to be small in comparison to other corrections, as precipitation fields don't move as fast as presented in fig. 2.12. The results based on standard error measures are ambiguous. While there are improvements in mean bias, most other measures show a slight worsening, so despite the appealing visual impression, the method cannot be claimed to provide a significant improvement.

A possible source of error to investigate would be the method to calculate the intermediate advected fields. Using the pull-method ensured valid data for each image pixel, but slightly moved the advection field as estimated by the optical flow algorithm. Determining the optical flow inversely in time (i.e. switching the roles of current and previous image) and using these estimates for the forward advection while using the usual estimates (those that had been estimated for the current study) for the backward advection, might reduce some of the error.

Hydrological or hydraulic modeling with very high resolution might draw the largest profit from this kind of correction. In larger scale and/or lumped modeling the effects (both positive and negative) will most probably be negligible.

3. Data Correction based on Geostatistical Analyses of Radar Fields

3.1. Introduction

The term geostatistics was coined by Georges Matheron for the mathematical framework he had established for the estimation of mining resources. His work formalized the method initially proposed by Krige (1951), which is now commonly known as Kriging.

The basis of every geostatistical estimation is the assumption of a random function whose realizations are the observed spatial fields of the resource in question (gold, petroleum etc.). This random function is also called regionalized variable (ReV) in order to stress its spatial extent.

The analysis of such an ReV is subject to certain constraints, under which estimations at unobserved locations may be made. The strongest assumption is that of stationarity. A stationary ReV is invariant to translation, that is, the distributions at each location are identical and independent of each other. Relaxing the stationarity assumption to second order stationarity leads to the assumption of an ReV that still has a constant expectation everywhere, but where the covariance between two different points depends on their separation distance h, only. If an ReV does not satisfy this assumption and therefore does not have a finite covariance, it may still satisfy the so-called intrinsic hypothesis. The intrinsic hypothesis only requires that the increments of the variables be second order stationary, i.e.

$$E\left[Z(x) - Z(x+h)\right] = 0 \tag{3.1}$$

$$VAR\left[Z(x) - Z(x+h)\right] = 2\gamma(h) \tag{3.2}$$

The variable $\gamma(h)$ is called the semivariogram, or variogram for short, and is the fundamental representation of the structure of an ReV:

$$\gamma(h) = \frac{1}{2}E\left[\left(Z(x) - Z(x+h)\right)^2\right] \tag{3.3}$$

It is connected to the spatial covariance (if it exists) by the following formula:

$$\gamma(h) = c(0) - c(h) \tag{3.4}$$

where $c(h)$ is the covariance function for a given separation distance h. The derivation of these properties can be found e.g. in Matheron (1971) or Journel and Huijbregts (1978).

For practical application of this equation, the expectation E[] was replaced by the mean over a set of points which are separated by the distance h, leading to the

so-called Matheron estimator.

$$\hat{\gamma}(h) = \frac{1}{2}\frac{1}{N_h}\sum_{N(h)}\left(z(x_i) - z(x_j)\right)^2 \tag{3.5}$$

where $N(h) = \{(x_i, x_j) : x_i - x_j \in [h - \delta h; h + \delta h]\}$ and N_h is the cardinality of $N(h)$. In the definition of the set $N(h)$, an interval of separation distances allows for discrete measurement locations to be used. This produces an empirical variogram, to which a theoretical function may then be fitted.

As the Matheron estimator is sensitive to outliers, several more robust alternatives have been proposed (Cressie and Hawkins, 1980; Genton, 1998). However, this problem becomes less of an issue, if a large amount of data is available. As this is the case with radar data, where each image consists of more than 40000 data points, it was considered to be safe to use the Matheron estimator throughout this study.

There exists a large number of theoretical variogram functions, of which the most commonly used will be presented in the following paragraphs.

The Nugget Variogram The nugget variogram models white noise. It is zero at $h = 0$ by the definition of a variogram, but assumes its sill value s for all other separation distances.

$$\gamma_{Nug}(h, s) = \begin{cases} 0 & \text{if } h = 0 \\ s & \text{if } h > 0 \end{cases}$$

It is used to account for immediate increases in variance even for small distances. The discontinuity may cause problems for some analyses. In this case, sometimes another continuous variogram but with a very small range may be used to mimic the effect of a nugget variogram without discontinuity.

The Linear Variogram The linear variogram is the simplest variogram function. It is also special in that it is unbounded and, as opposed to the other variograms presented below, does not approach any limit. Given a certain slope m the variogram is given by

$$\gamma_{Lin}(h, m) = \frac{h}{m}$$

In two-dimensional space, this describes an infinite inverted cone with its vertex at the origin.

The Spherical Variogram The spherical variogram is one of the most widely used in the literature. It is defined by a range r after which it reaches its sill s and points separated by a distance larger than this range are assumed not to be correlated with each other any more.

$$\gamma_{Sph}(h, r, s) = \begin{cases} s\left(\frac{3}{4}\frac{h}{r} + \frac{1}{4}\frac{h^3}{r^3}\right) & \text{if } h < r \\ s & \text{if } h \geq r \end{cases}$$

The spherical model allows the use of sparse matrices, when Kriging systems with a lot of data must be solved, as the variogram contains information only for distances smaller than r.

The Exponential Variogram Another widely used variogram is the exponential, which is defined by two parameters; a sill s and a range r.

$$\gamma_{Exp}(h, r, s) = s\left\{1 - \exp(-h/r)\right\}$$

As opposed to the spherical type, the exponential only asymptotically approaches the sill, implying weak but non-zero correlation between points far away from each other. Therefore, the range parameter cannot directly be used as a measure of decorrelation in space. However, an 'effective range' may be defined as the separation distance at which the variogram reaches 95% of its sill value. By solving the variogram equation for this value it can be shown that the effective range of the exponential type is $-\ln(0.05)r \approx 3r$.

The empirical variograms of precipitation fields can be fitted well to the exponential type, which is why this model will be used mainly throughout this thesis.

The Gaussian Variogram The Gaussian variogram is able to model a zone of high correlation for small separation distances, and is defined by a sill s and a range r similarly to the exponential variogram.

$$\gamma_{Gau}(h, r, s) = s\left\{1 - \exp(-h^2/r^2)\right\}$$

As Clark (1977) showed that a regularized variogram may show such a behavior, it should be considered that regularization might be affecting a process, if a Gaussian variogram provides the best fit to some data.

The Matérn Variogram The Matérn Variogram may be seen as a generalization of the exponential and the Gaussian variogram. Besides sill s and range r, it introduces a third parameter v which controls its shape.

$$\gamma_{Mat}(h, r, s, v) = s\left\{1 - \frac{2^{1-v}}{\Gamma(v)}\left(\frac{h}{r}\right)^{v} K_v\left(\frac{h}{r}\right)\right\}$$

To calculate it, values of the Gamma function and the modified Bessel function of the second kind and order v, K_v, are needed. For values of $v = 0.5$, the Matérn model is identical to the exponential model. As v approaches infinity, the Matérn model approaches the Gaussian model. It can therefore be used as a tool to decide, which of the two simpler models may be more appropriate for a certain problem.

3.2. Analysis of the Effect of the Radar Sampling Volume on Variogram Estimates

3.2.1. Introduction

Matheron (1971) also investigated the effects of (possibly weighted) moving averages on an ReV and the variogram of the new ReV resulting from such a transformation.

The convolution g of a function f_1 with another function f_2 is defined as

$$g(x) = \int f_1(y) f_2(x - y) dy = \int f_2(y) f_1(x - y) dy \tag{3.6}$$

or in short form

$$g = f_1 * f_2 \tag{3.7}$$

A weighted moving average over a function can also be described as a convolution of that function with the corresponding weighting function. In geostatistics this is referred to as 'regularization'. It provides the link from point measurements on a continuous regionalized variable to averaged measurements taken e.g. by analyzing the mean ore content of a mining block or, as in the case of radar the reflectivity measured over a pulse volume.

Matheron (1971) showed that the covariogram c of an ReV f can be written as the regularization of the variable with itself.

$$c = f * \hat{f} \tag{3.8}$$

where $\hat{f}(x) = f(-x)$ denotes the function mirrored at the origin.

He went on to show that if $f_p = f * \hat{p}$ is a regularization of a ReV, then its covariogram c_p can be derived to be:

$$\begin{aligned} c_p &= f_p * \hat{f}_p \\ &= f * \hat{p} * \hat{f} * p \\ &= f * \hat{f} * p * \hat{p} \\ &= c * P \end{aligned} \tag{3.9}$$

This means that the covariogram of the regularized ReV is the regularization of the original covariogram with the covariogram of the weight function $P = p * \hat{p}$.

In practice, the covariogram of the regularized ReV (c_p) and the weight function (whose the covariogram P can be calculated) are known. c_p can be determined from the data, while the weight function is determined by the way the data is obtained. In order to retrieve the covariogram (c) of the original ReV, a deconvolution of eqn. 3.9 needs to be found.

Pardo-Igúzquiza et al. (2006) used a least squares approach to find that point-scale variogram c, which for a given regularization would best match the observed c_p. This was feasible and showed good results in the subsequent application of cokriging two satellite images of different resolutions to a sharpened image, as the satellite images' resolution could be assumed to be the same everywhere (i.e. pixels of identical size). For weather radar, the case is slightly different, as the pulse volumes increase with increasing distance from the radar.

In the following, two approaches will be presented, which aimed at determining the original (point-scale) covariogram assuming that the radar measurement presented a regularized version of the underlying precipitation process.

3.2.2. Average Variograms from Volumes of Equal Geometry

The first approach tried to follow the method of Pardo-Igúzquiza et al. (2006) as much as possible in that for variogram generation only data from pulse volumes of equal size were chosen. This results in using data along concentric circles around the radar as shown schematically in fig. 3.1a.

From these sub sets empirical variograms were calculated using the Matheron estimator (eqn. 3.5). Afterwards, a theoretical variogram was fitted to the empirical ones using least squares and a simple exponential model. Due to the limited size of the data on one ring, the estimated variograms for an individual image were too unstable to be fitted properly, as can be seen in fig. 3.1b. Assuming that the underlying ReV would not change too much over time, the procedure was modified to average the ring variograms for several images. The time period between 2006-08-27 8:40 to 2006-08-27 12:40 UTC was used as it contained mainly small thunderstorms scattered all over the radar range. This was necessary, because if whole rings were covered by a contiguous precipitation field, only the maximum detectable range, which would grow linearly with the radius of the ring, could have been estimated, which would completely obscure any regularization effects. The averaging proved to stabilize the empirical variogram estimates to a point where fitting a theoretical model would seem possible (fig. 3.1c). The range and sill of the fitted exponential model were then plotted over the radius of the ring they were estimated from, which led to the result displayed in fig. 3.2b.

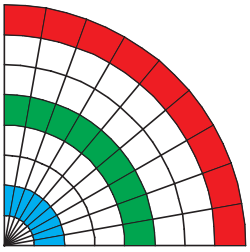

(a) schematic view

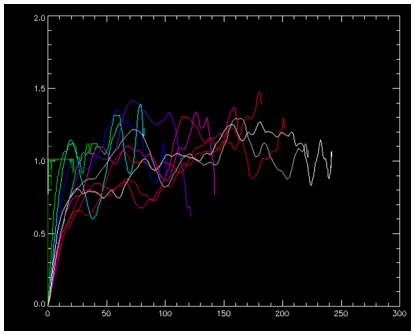

(b) single image ring variograms

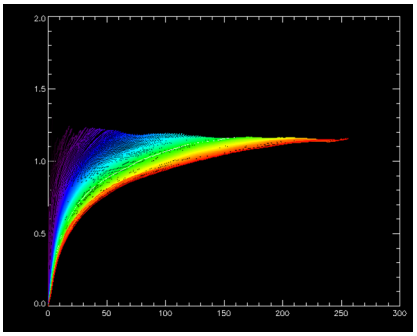

(c) mean ring variograms

Figure 3.1.: Schematic representation of radar bins taken for variogram calculations (a), results for an individual image (b), and averaged varigorams over a month of data (b)

The figure shows that the normalized sill is noisy and significantly below 1 up to a ring radius of approximately 80 km. The variogram range increases almost linearly with a bump between 90 and 100 km. As Clark (1977) pointed out, the range of a variogram should increase roughly by the geometrical extent of the regularizing block (if the weighting function would be uniform). This would imply an increase in range by the increase in diameter of a pulse volume. At 1° beam width this would

amount to an increase by 0.0174 km/km. The slope as estimated by linear regression in fig. 3.2b has a slope of 0.0617 km/km. Given that this regression was done on the range parameter and, as explained earlier, the effective range of an exponential variogram is about three times the range parameter, the increase in effective range is about 10 times larger than what would be expected by geostatistical theory.

In addition, the aforementioned bump cannot be explained by regularization. For comparison an image from the averaging period is presented in fig. 3.2a. It shows a larger contiguous patch of precipitation to the south west of the radar, at an approximate distance between 80 and 100 km. This patch moves almost tangentially from west to east, remaining in the same radar ranges for most of the averaging period. This is most likely the reason for the increase in range for this radar-range interval.

This showed that even slight inhomogeneities in a radar image would completely mask any regularization effect that could be estimated by this method.

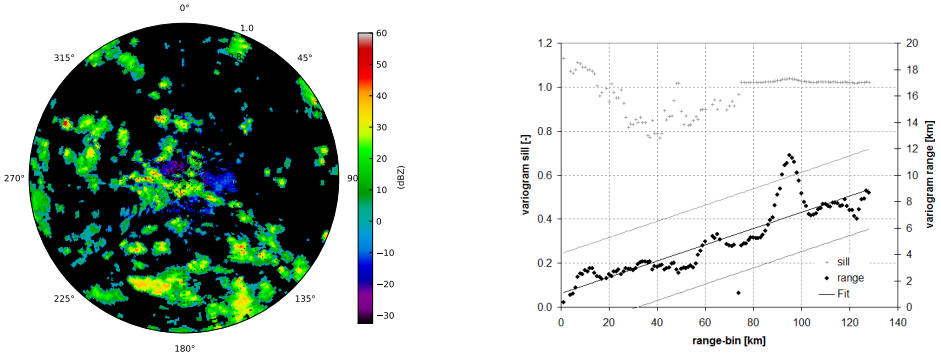

(a) example radar image **(b)** fitted variogram parameters

Figure 3.2.: Example radar image (2006-08-27 11:40 UTC) representative of the analysis period and resulting variogram parameters as function of distance from the radar.

3.2.3. Maximum Likelihood Estimation

In order to remove effects due to averaging and to overcome the limitation of sampling along rings of equal distance from the radar, a second method was tested. As Journel and Huijbregts (1978) showed, the mean variogram between two blocks may be approximated by evaluating the point support variogram between all points of a discretization of one block with all points of a discretization of the other and taking the mean. Assuming the data to be Gaussian, and prescribing a certain point support variogram, the likelihood of the data, conditional on the variogram parameters can be determined and maximized. This way, all data from a radar image may be used for the estimation taking the different sampling volumes directly into account.

However, the method is computationally demanding. Calculating a variogram using the Matheron-estimator is an $O(N^2)$ operation if N data points are used. Discretizing a block by M intervals in each of d dimensions adds an additional factor

of M^d to the computing time. This is further aggravated by the fact, that during optimization the likelihood needs to be calculated several times until the optimization algorithm converges toward the solution. In order to make the problem tractable, subsets of different sizes were selected from the data and it was tested, whether there was a systematic change in the resulting variogram parameters depending on the subset size. Each element of a subset consisted of a fixed number of data points on which the actual calculations were carried out. The final likelihood would be the negative sum of the logarithms of all the elements, which was to be minimized by a simplex algorithm.

For the experiment, data from the radar scan at 2006-08-20 12:55 UTC from the DWD radar Türkheim was used. The image, which is displayed in fig. 3.3a shows thunderstorms organized along several lines, and would have been a good candidate for comparisons with the ring-variogram method presented earlier, as most structures in the image were organized radially.

The minimizations were carried out using sets of sizes between 100 and 20000 elements which consisted of 10 to 30 blocks each. This way, between 3 and 100% of the complete data set were used. The estimated range parameters for an exponential variogram varied between 9.45 km and 13.85 km with an average of 11.05 km. Even though the discretization was reduced to two points per dimension, leading to a discretization of 4 points per block only, the largest set took approximately 9 hours to complete for a single 5-minute radar image.

Figure 3.3b shows the empirical variogram estimated using the standard Matheron-estimator without accounting for the different pulse volumes. The exponential type variogram, that was fitted to this estimate had a range of 6.87 km. Clark (1977) demonstrated for a one-dimensional example that regularization must lead to an increase in range of the variogram. As each radar volume presents a regularization of the assumed underlying ReV of the precipitation field, the range estimated by MLE should have been shorter than the range estimated by the Matheron-estimator.

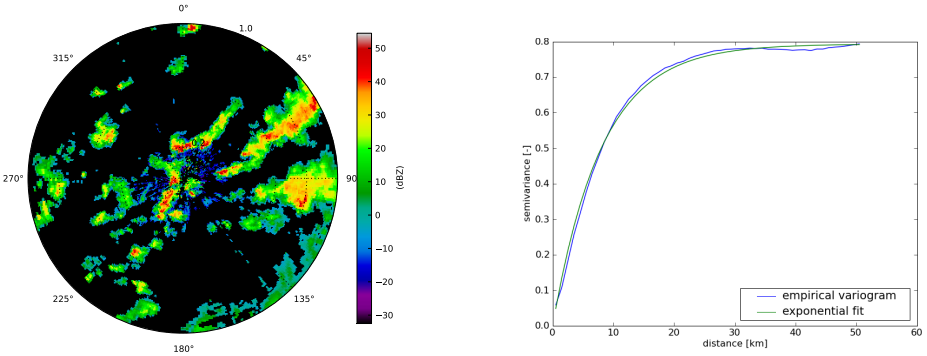

(a) radar image **(b)** estimated global variogram

Figure 3.3.: Empirical and fitted theoretical variogram estimated from the complete radar image of 2006-08-20 12:55 UTC; Radar Türkheim

3.2.4. Discussion

With both experiments providing results that contradicted basic theoretical considerations and being either strongly influenced by noise or computationally infeasible for any practical use, this line of research was abandoned for the time being.

Given some later experience with the techniques presented in the following sections, the likelihood method may be refined, both from the conceptual and the computational point of view, and may yet provide some results. However the manifold influences on the radar measurement, which occur additionally and independent of the increase in sampling volume, will make it very hard to distinguish the small signal that the regularization may provide.

In addition, the effects on interpolation results would be very small. In a hypothetical one-dimensional experiment, the change between a block-Kriging estimate and a point Kriging estimate was calculated. This experiment showed that the effect would amount to a few percent and only if the interpolation source were located very close to the target, inside the block. When the distances between interpolation sources and the target are beyond the block extent, the effect quickly diminishes towards zero.

Therefore, it is the opinion of the author that any other effect (like anisotropies or deviations of the data from Gaussianity or the stationarity assumptions) will have far more influence on the interpolation results.

3.3. Estimation of Spatial Structure with Censored Data using Copulas

3.3.1. The Copula Concept

The basis of Copula theory is Sklar's Theorem, which states that any multivariate cumulative distribution function H can be written as

$$H(x_1, \ldots, x_d) = C\left(F_1(x_1), \ldots, F_d(x_d)\right) \tag{3.10}$$

where $C : [0,1]^d \rightarrow [0,1]$ is a copula. Sklar proved this copula to be unique for a given combination of H and F_i. Conversely, this means that many multivariate distribution functions can be generated using the same copula by applying different marginals, or by using different copulas when keeping the marginal distributions. Another consequence is that using copulas, it is possible to separate the marginal distributions from the dependence between the variables.

Due to this flexibility, copulas have received increasing interest in the field of hydrology and meteorology (Schoelzel and Friederichs, 2008). They are used for interpolation (Bárdossy and Li, 2008; Bárdossy, 2011), analysis and simulation of rainfall fields (Aghakouchak et al., 2010; AghaKouchak et al., 2010), multi-site rain gauge timeseries (Bárdossy and Pegram, 2009) or design rainfall generators (Vandenberghe et al., 2010). In meteorology they are used to downscale NWP rainfall data to higher resolutions (Laux et al., 2011; van den Berg et al., 2011).

One common copula is the Gaussian copula. Eqn. 3.11 gives its definition.

$$C_{\Sigma}^{Gauss}(u) = \Phi_{\Sigma}\left(\Phi^{-1}(u_1), \ldots, \Phi^{-1}(u_d)\right) \tag{3.11}$$

Here, Σ is the d-dimensional correlation matrix. Practically, this definition means that working with the multivariate Gaussian distribution on normal-score transformed data is identical to using a Gaussian copula on the data together with their particular marginals. Due to this, the Gaussian copula is sometimes referred to as meta-Gaussian model by some authors (Wu et al., 2011).

While there are many other copula models like the Archimedean type copulas, the χ^2 or the v-copula, the well-known properties of the Gaussian distribution make the Gaussian copula a good starting point for copula-based analyses.

Stochastical representation of precipitation When dealing with precipitation data, one is faced with the problem of intermittency. Straightforward frequency analysis of rainfall data would lead to a right skewed distribution of non-zero values and a large number of discrete zero-values. The same is true when looking at the spatial distribution of rainfall which consists of more or less connected areas of non-zero precipitation amounts embedded in a background field of zero-rainfall. When dealing with single-site gauge data, this problem has often been addressed by modeling the occurrence and the amounts of precipitation separately using two different distribution functions (Wu et al., 2011; Wilks and Wilby, 1999; Charles et al., 1999). This concept has been also used in spatial analysis by e.g. using an indicator field for the occurrence of precipitation and a second field for the precipitation amounts (Berrocal et al., 2008). Another approach would be to model precipitation using only one continuous distribution, truncating it at a certain threshold and assign zero to all values below that threshold (Allcroft and Glasbey, 2003; Sansó and Guenni, 2000).

In addition to the mathematical elegance of this approach, which enables modeling one process by just one distribution, it also lends itself to a physical interpretation of the stochastic process. If the latent continuous distribution is seen as the total amount of water in the atmosphere, rainfall is that part, which exceeds the air's capacity for its gaseous phase. An analysis of the spatial and temporal distribution of total water content could provide further insight on the validity of this assumption and the more detailed distributional properties of that latent variable.

3.3.2. Maximum Likelihood Estimation (MLE) of the Variogram for Censored Data

When estimating the variogram on censored data using the Matheron or a similar estimator, a decision has to be made how to treat the censored data. All the data may be used with the censored ones being assigned a minimum value. If these data cluster, like the non-raining portions of a precipitation field, the variograms are most likely estimated with too large a range, implying much more spatial coherence in the uncensored data than is actually the case. Another approach would be to remove the censored data and estimate the variogram solely based on the uncensored values.

When constructing the pairs, they may be distinguished into three sets, for which different likelihoods have to be calculated. These sets, as they appear in eqn. 3.12, are: I_1 – the set of all pairs in which both values are uncensored, I_2 – the set of all pairs in which one of the values is censored and the other is uncensored and I_3 – the set of all pairs in which both values are censored. For further clarification,

superscripts c and u are attached to the values to indicate, whether they are censored or uncensored, respectively.

Thus, the likelihood of a parameter set ζ for a given dataset and configuration of pairs is then given by

$$\begin{aligned} L(\zeta) &= \prod_{i,j \in I_1} \phi\left(z_i^u, z_j^u, \rho(\gamma(h_{ij}, \zeta))\right) \cdot \\ &\quad \prod_{i,j \in I_2} \phi(z_j^u)\, \Phi\left(z_i^c | z_j^u, \rho(\gamma(h_{ij}, \zeta))\right) \cdot \\ &\quad \prod_{i,j \in I_3} \Phi\left(z_i^c, z_j^c, \rho(\gamma(h_{ij}, \zeta))\right) \end{aligned} \tag{3.12}$$

where $\rho()$ is the correlation function defining the off-diagonal element of the 2x2 covariance matrix using the variogram function $\gamma(h_{ij}, \zeta)$ of the separation distance h between points i and j and the additional parameters ζ. $\Phi(x, y, \rho)$ in this case, is the bivariate standard normal distribution function of values x and y and correlation ρ, while ϕ is its density.

In the bivariate case, the conditional bivariate distribution in the second product of eqn. 3.12, may be replaced by a univariate standard normal distribution function of a regression estimate

$$\Phi\left(z_i^c | z_j^u, \rho(\gamma(h_{ij}, \zeta))\right) = \Phi\left(\frac{z_i^c - z_j^u \cdot \rho(\gamma(h_{ij}, \zeta))}{\sqrt{1 - \rho(\gamma(h_{ij}, \zeta))^2}}\right)$$

3.3.3. Comparison Between Different Variogram Estimates

Fig. 3.4 shows a comparison for the parameter r of an exponential variogram for estimations done by a least squares fit of the Matheron-estimates and the MLE method described before. This plot is used to show that the MLE method indeed produces different results from the Matheron-estimated variograms and that there is no simple functional relationship between the two. It can be seen that the MLE method mostly calculates longer ranges for small Matheron estimates and shorter ranges for cases in which the Matheron-estimator would estimate ranges larger than 50 km. The linear regression line, plotted in the figure has a slope of 0.464 and an intercept of 17.446 km with a correlation coefficient of 0.768.

There are a few peculiarities in this figure, most notably the concentration of pairs along the 1:1 and several other straight lines. As an example, the 2:1 line has been plotted into the figure as well. The 1:1 line may be explained by a premature stop of the optimization. Although the data has been filtered for optimization failure, results where the optimization algorithm reported successful convergence were included in the data. The clusterings around the 2:1 and other straight lines, can, however hardly be explained this way. Whether this is a numerical problem, or due peculiarities of the field, for which the variogram had been estimated (e.g. almost no rainfall, residual clutter), would need to be investigated.

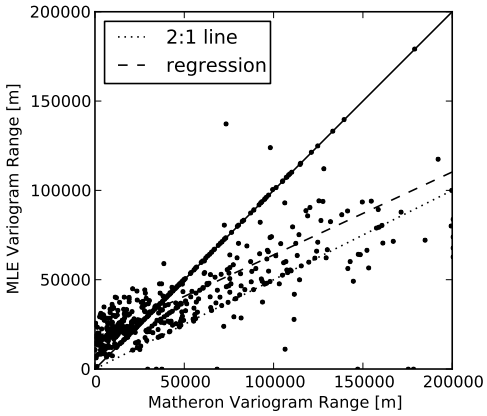

Figure 3.4.: Scatterplot of different estimates of the range parameter of an exponential variogram, based on Matheron and Maximum Likelihood Estimation

3.4. Radar-Gauge Adjustment using a Censored Copula Interpolation Approach

3.4.1. Introduction

The idea of calibrating radar with rain gauges is almost as old as radar meteorology itself. Hitschfeld and Bordan (1954) already suggested to use gauge measurements at a distance from the radar as a reference for path integrated attenuation to reduce the error in a forward attenuation correction scheme (c.f. section 2.3). However, in this setting the gauge data is not used to correct the rainfall estimates directly but constrains another correction.

In this early era of radar meteorology, research focused on finding the optimal Z-R relationship, leading to a wealth of relations for different climates and precipitation types. Battan (1973) lists 69 different relationships published between 1948 and 1970.

In the 1970s several studies were conducted investigating the possibility to adjust radar precipitation estimates by calculating the bias between radar and gauge and correcting the radar accordingly. Both local and global techniques were applied and some of them are summarized in Wilson and Brandes (1979).

One of the simplest methods is to calculate the mean bias between radar and gauge measurements,

$$F = \sum_{i=1}^{N} G_i \Big/ \sum_{i=1}^{N} R_i \tag{3.13}$$

or

$$F = \frac{1}{N} \sum_{i=1}^{N} G_i / R_i \tag{3.14}$$

where R is the precipitation amount estimated by the radar and G is the amount measured by the gauges. The factor F may then be applied globally to all radar pixels. These techniques are still in use and under investigation today (e.g. Holleman (2007)).

As it was found that the bias of the radar is not constant over the whole radar umbrella, local bias adjustments were investigated as well (Brandes, 1975). This form of adjustment already requires some kind of interpolation to transfer the local bias estimates from the gauge locations to all other radar pixels.

Another approach to gauge adjustment is that of probability matching. Presented by Rosenfeld et al. (1993) and extended in Rosenfeld et al. (1994), the method initially tries to establish a kind of nonparametric Z-R relationship. Based on the assumption that the cumulative distribution of the gauge-measured precipitation and that of the radar-measured reflectivity are due to the same underlying process, basically a quantile-quantile transformation is done between reflectivity and gauge precipitation. While this method can be more flexible than a simple adjustment factor, it cannot account for effects, which disturb the monotonicity between Z and R, which is for example the case when the Z values are affected by attenuation. It also needs Z and R estimated at similar time intervals and is as such not directly useful, if e.g. the gauge measurements are hourly accumulations while the radar data are 5-minute interval snapshots.

Since the beginning of the new millennium, gauge adjustment has been studied more intensely and several new approaches have been presented. García-Pintado et al. (2009), for example present what they call a concurrent multiplicative additive approach; a kernel smoothing interpolation of a multiplicative and an additive bias component as calculated from radar-gauge pairs. Jatho et al. (2010) combine radar and interpolated gauge data based on indices, which were calculated to represent the uncertainty about the correctness of the respective estimate. Seo and Breidenbach (2002) developed a local bias adjustment using an exponential smoothing filter for interpolation and a Kalman filtering approach for the combination of gauge and radar fields.

Ehret (2003) presented a technique, commonly referred to as conditional merging. It uses the same approach that would be used to produce a conditional stochastic simulation from a simulation method that is itself only able to produce unconditional fields, like e.g. the Turning Bands method. This approach showed quite good performance in comparison studies and has been implemented as one gauge adjustment method in the operational processing chain of the German weather service.

Todini (2001) presented an adjustment method based on a Bayesian approach, interpolating the gauge data to the radar resolution using block Kriging and employing the Kalman filtering framework with the radar as the innovation to produce a new estimate of the actual precipitation.

Most recently Velasco-Forero et al. (2009) presented an adjustment method using Kriging with external drift to directly incorporate the radar information during gauge interpolation.This method has been evaluated very successfully in other studies like Schiemann et al. (2011) and Goudenhoofdt and Delobbe (2009).

In the following, a new method to combine radar and gauge information is presented based on several new concepts that have not been addressed by previous authors.

3.4.2. Methodology

The method is a censored copula interpolation with weather radar data as external drift (CCID), whose components will be presented now.

Interpolation using Copulas

The first innovation of this method is the copula approach to interpolation. It allows a separate treatment of dependence and marginal distribution. Copula interpolation amounts to calculating a full distribution for each interpolation point, conditional on the available data. From this distribution, the conditional expectation (i.e. the mean) but also quantiles like the median or quantile ranges for uncertainty estimations may be calculated. The method may also be used for conditional sequential simulation without much change, by drawing a random number from the estimated distribution and adding the interpolated point to the set of conditions. Details on copula interpolation can be found in Bárdossy and Li (2008). In the following the extension of the copula interpolation approach to censored data will be presented.

Censoring

The second novelty in this approach is the explicit handling of censored values. It is based on the approach of Bárdossy (2011) who used it to interpolate groundwater parameters, where some values were below an analysis limit. The method calculates the conditional density of the value at an interpolation point

$$
\begin{aligned}
g_x(z) &= P(Z(x) = z | Z(x_i) \leq z_0; Z(x_j) = z_j) && (3.15)\\
&= \frac{P(Z(x) = z, Z(x_i) \leq z_0, Z(x_j) = z_j)}{P(Z(x_i) \leq z_0, Z(x_j) = z_j)} && (3.16)\\
&= \frac{P(Z(x_i) \leq z_0 | Z(x) = z, Z(x_j) = z_j) P(Z(x) = z, Z(x_j) = z_j)}{P(Z(x_i) \leq z_0 | Z(x_j) = z_j) P(Z(x_j) = z_j)} && (3.17)\\
&= \frac{P(Z(x_i) \leq z_0 | Z(x) = z, Z(x_j) = z_j)}{P(Z(x_i) \leq z_0 | Z(x_j) = z_j)} \cdot P(Z(x) = z | Z(x_j) = z_j) && (3.18)\\
&= g_x^c(z) \cdot g_x^u(z) && (3.19)
\end{aligned}
$$

Eqns. 3.18 and 3.19 repeat the observation by Bárdossy (2011) that the conditional density may be separated in an uncensored part $g_x^u(z)$, which is identical to the conditional density that would have been obtained, if no censored values were in the dataset, modified by a contribution from the censored conditions $g_x^c(z)$.

It should be noted that in the preceding equations the value of z was assumed to be known. In order to obtain the full conditional distribution, the densities must be calculated for a range of values z and the distribution must be derived by numerical integration of the density.

The conditional distribution of a multivariate normal distribution has an analytical solution. If we consider a partitioning of the mean vectors and covariance matrix of

a multivariate normal distribution,

$$\begin{aligned} \mu &= \begin{bmatrix} \mu_1 \\ \mu_2 \end{bmatrix} \\ \Sigma &= \begin{bmatrix} \Sigma_{11} & \Sigma_{12} \\ \Sigma_{21} & \Sigma_{22} \end{bmatrix} \end{aligned} \tag{3.20}$$

then the distribution of x_1 conditional on $x_2 = a$, $P(x_1|x_2 = a) \sim N(\bar{\mu}, \bar{\Sigma})$ is again normally distributed with

$$\begin{aligned} \bar{\mu} &= \mu_1 + \Sigma_{12}\Sigma_{22}^{-1}(a - \mu_2) \\ \bar{\Sigma} &= \Sigma_{11} - \Sigma_{12}\Sigma_{22}^{-1}\Sigma_{21} \end{aligned} \tag{3.21}$$

Using these equations, the censored copula simulation may be expressed for the Gaussian copula case by the following equation

$$g_x(z) = \frac{\Phi\left(z_i^c|z, z_j^u\right)\phi\left(z, z_j^u\right)}{\Phi\left(z_i^c|z_j^u\right)\phi\left(z_j^u\right)} \tag{3.22}$$

with Φ being a conditional normal distribution with conditional mean and covariance matrix calculated using eqns. 3.20 and 3.21, and ϕ being standard normal densities. The initial covariance matrices are generated using the variogram with parameters estimated before, and the separation distances between the individual points.

The multivariate normal distributions need to be integrated numerically, which can be done, e.g. by using the method presented by Genz (1992). As this becomes more time-consuming the more censored values are part of the conditioning points for an interpolation, one further simplification has been applied by replacing the censored conditions with pseudo non-censored conditions. These were given a z-value, which corresponds to half of the quantile value for the original censoring threshold.

Marginal Distributions of Radar and Gauge In order to use the copula approach, the marginal distributions of radar and gauge data must be determined. For the radar data, this is relatively straightforward. As the radar samples the whole area, the empirical distribution of the measurement provides a representative and reasonably smooth estimate. Due to the fact that non-raining clouds still produce a measurable reflectivity, a threshold must be introduced below which a pixel will be denoted as non-raining. This is best done already during Z-R conversion of individual (e.g. 5-minute) images, as even minuscule precipitation rates may accumulate to significant amounts for longer accumulations. For the scope of this thesis, all 5-minute radar rain intensities below 0.05 mm/h were considered as zero precipitation and were accumulated as such.

Estimates of the Non-Raining Fraction of a Precipitation Field From the radar data, the quantile p_0 of no rain was determined. This p_0 was also used in the estimation of the marginal distribution of the gauge data, for the following reason: differently from the radar, the gauges only sample the rainfall field at a limited number of locations. One can easily think of situations of isolated convective events,

which would be mostly missed by the majority of gauges. Or, on the other hand, in the case of widespread rain, almost all gauges might report precipitation, with no gauges reporting zero rain, although there were regions, where the radar would show that it hadn't rained. In both cases, values of p_0 calculated from the gauge data, would either over or underestimate the proportion of non-raining areas.

This was attempted to quantify by a bootstrapping experiment. For this experiment an hourly radar accumulation was used. The radar field was then sampled by a virtual network of gauges. This network was either constructed by drawing a number of random coordinates equal to the number of gauges in the original network. Another approach was to use the original network and apply a random transformation to this network, consisting of a random translation and a random rotation, and sample from the transformed locations. Then the distribution of the non-raining proportion $p_{0,g}$ of the samples was compared to the non-raining proportion estimated from the radar $p_{0,r}$.

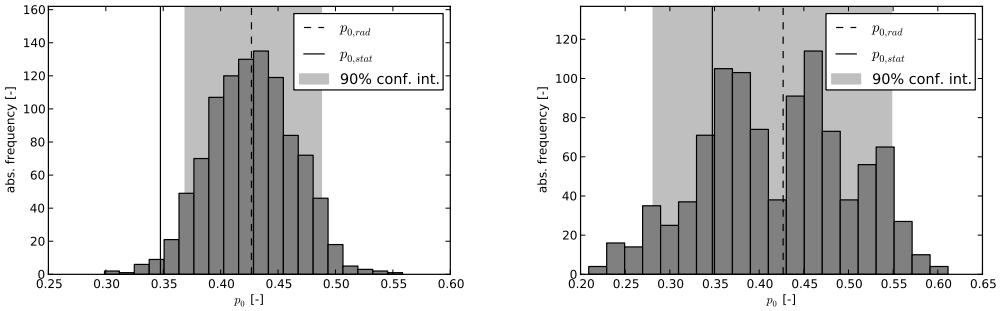

(a) random network **(b)** transformed original network

Figure 3.5.: Results of bootstrapping p_0

Fig. 3.5 shows the result for such a bootstrap experiment for both network randomizations for the hourly accumulation of 2008-06-02 18:50 UTC for Radar Türkheim. The outcome is somewhat ambiguous. While non-raining proportion lies outside the 90% confidence limits for the transformed original network, it is clearly outside for the completely randomized network. What is striking, however, is the large range of $p_{0,g}$ that can be achieved by different network configurations. In the purely random case it amounts to $\pm$ 0.1 or approximately 25% of the estimated $p_{0,r}$ from the radar. In the transformed network case it is even larger, reaching $\pm$ 0.2 or almost 50% of $p_{0,r}$. This large sampling uncertainty led to the decision to choose p_0 as determined by the radar, to also serve as the non-raining proportion for the gauge marginal distribution.

Kernel Density Estimation (KDE) for Bounded Data The small sampling density of rain gauges also implies a certain non-smoothness of their empirical marginal distribution. In addition, the interpolation results need to be transformed back from copula space to precipitation space, and because the gauges are viewed as the quantitatively more correct measurements, their marginal distribution should be used for that. As interpolation quantiles may exceed the empirical quantiles, which are

usually undefined beyond N/(N+1)[1], a way to properly represent the tails of the marginal distribution has to be found as well. It was decided to use KDE (Parzen, 1962; Rosenblatt, 1956) to produce a continuous estimate of the gauge marginal distribution. A non-parametric method was preferred to a parametric fitting, because, especially for the higher quantiles, small variations in fitting parameters could lead to large variations in the tail behavior of the distribution.

One problem for a KDE of precipitation data is its boundedness. If a symmetrical kernel would be used directly for the estimation, biases would be introduced in the lower quantiles. As a possible solution, a gamma kernel approach as proposed by Chen (2000) had been considered. It could, however, be shown that this kernel only produces reasonable results, if the data come in fact from a gamma distribution. Better results were achieved by applying the KDE to the log-transform of the data. This has two advantages. First, the data lose their lower bound after log-transformation and second, skewed distributions both become more symmetric and the distances between extreme values are reduced considerably. The last feature becomes important during bandwidth estimation. The bandwidth is a free parameter in KDE. It determines the size of the kernel and thus influences the amount of data points included in each density estimate. A non-optimal choice of the bandwidth leads to errors in the density estimates. Too large a bandwidth takes too many data points into account, leading to an oversmoothing of the estimate, while too small a bandwidth has the opposite effect and provides a density with an excessive number of modes, with their number approaching that of the number of data points for the extreme case of a bandwidth that considers only one data point per estimate. Pseudo-likelihood cross validation (Duin, 1976; Marron, 1988) was used to determine the optimal bandwidth. Both preceding authors point out that this pseudo-likelihood estimate is influenced strongly by the tail behavior of the distribution. By log-transforming the data, this effect can be reduced.

Radar Data as Auxiliary Information based on Gauge Correlation

Many gauge adjustment methods treat radar and gauge data separately in the sense that during interpolation only values at gauge locations are used, and the radar information that is available at each target in the interpolation domain is combined with the interpolation estimate, afterwards. Velasco-Forero et al. (2009) and Todini (2001) explicitly condition their estimates directly with the radar data using radar residuals as external drift in the first, and the radar as the innovation in a Kalman-filtering framework in the latter case.

So far, the distribution at an interpolation point is conditioned on the surrounding gauge data alone. Now, the co-located radar value is introduced as an additional condition. In order to do so, an assumption about the covariance between the radar measurement and the estimated precipitation value, as well as the covariance to all other conditioning points has to be made, as this is required to complete the covariance matrix of the underlying Gaussian copula.

By estimating the spatial structure using the radar data, it was assumed, that the radar measurement properly captures the spatial variability. Therefore, the covari-

[1] using the Weibull estimator of order statistics. For a list of other estimators and the controversy about their use, see Makkonen (2008) and Cook (2012)

ance between the radar and the other conditioning points should also be described by this variogram. The correlation between gauge and co-located radar values for a timestep gives a measure of the current agreement between radar and gauge measurement. As the gauge measurement is deemed more reliable, the condition from the radar is thus reduced in weight if the radar data deviates much from the gauges and is increased if both appear to measure similar values. Consequently, the better radar and gauge agree with each other the more similar to the radar measurement the final interpolation will become. Otherwise the interpolation will fall back to relying on the gauge data, without further modifications to the method.

The correlation is determined similarly to the maximum likelihood estimation of the spatial structure. Instead of finding the optimal parameters for a correlation function, which was dependent on separation distance, the correlation itself is used as the parameter to be optimized. The separation of the pairs into three sets (both uncensored, mixed censored-uncensored, both censored) and the calculation of the likelihoods remains the same.

Methods used for Comparison

Censored Copula Interpolation (CCI) without Drift This is a normal Gaussian copula interpolation without using the radar data as additional information. It was used in cross-validation to assess the additional value the inclusion of the radar data would have.

Quantile-Quantile (QQ) transformation This method only changes the radar values to match the gauge's distribution function for a particular image. Its results, together with that of the pure copula interpolation would bracket those of the CCID approach with the former using no radar data at all, the latter using the radar data to some degree, while the QQ-transformation uses the radar data alone, just changing the marginal distribution. As a quantile transformation, it is similar to the probability matching methods mentioned in the introduction, although here, the gauge distribution function is calculated for each image separately.

Ordinary Kriging (OK) In order to compare the new methods with some more commonly used adjustment techniques, ordinary Kriging was implemented and cross-validated on the same data sets. For more information on Kriging, the derivation of the interpolation equations for the different variants and applications, the reader is referred to textbooks like Journel and Huijbregts (1978) Isaaks and Srivastava (1990), Chiles and Delfiner (1999) or Wackernagel (2003). Although this method is not a real adjustment technique, it is widely used to interpolate gauge data and is therefore an alternative to radar data. No transformation was done to the gauge data before Kriging, and the variogram as estimated from the censored MLE was used.

Kriging with Radar as External Drift (EDK) External Drift Kriging was used as another interpolation method, which incorporates the radar data. Its use as a method for comparison is mainly motivated by the success of the method by Velasco-Forero et al. (2009), although it was not implemented exactly like explained there. No

transformation was done for this interpolation method either, and the same variogram from the censored MLE was used.

Censored Copula Interpolation with Attenuation Corrected Radar Data as Drift (CCID_A) Having showed the potential improvement due to attenuation correction, it was tested, whether this can further be improved by gauge adjustment, and whether the improvement might be notably different from that of uncorrected data. This used the full CCID procedure described above with the same gauge data set but different radar information. Here, data corrected for attenuation according to the method described in section 2.3 was used instead of the purely clutter corrected radar data. The time-period, the conversion to rain intensity and the aggregation to hourly resolution were, however, identical to the clutter corrected set.

3.4.3. Results

The first analysis of the performance of the CCID-approach was run over a period of 3 months between May 1st and August 1st 2008. This is the same period that was presented in the analyses in chapter 2.

The radar data was based on the DX-product for the radar Türkheim. This product is issued by the DWD and contains one 360 degree sweep of reflectivity measurements at the lowest possible elevation above the radar horizon every 5 minutes. The data had been corrected for clutter using the method described in section 2.2. Afterwards, reflectivities had been converted to rain intensities using the standard 3-part Z-R relationship of the DWD (Bartels et al., 2004) and aggregated to match the hourly resolution of the rain gauge data.

Leave-one-out cross-validation was used to assess the performance of the CCID and all comparison methods. During cross-validation, both the gauge marginal distributions (including the KDE bandwidth parameter) as well as the radar-gauge correlation were calculated every time. This sometimes led to the optimizations used for both estimations to fail for various reasons. These cross-validation results were excluded from the analysis.

Table 3.1 shows some error measures calculated from the respective estimates when compared to the value of the unused gauge. The value closest to that of a perfect estimate in each column is given in bold. RMSE and MAE, ideally should be zero. The column bias gives the ratio between the mean estimate and the mean of the gauge values, and as such provides a measure of the long term bias. Its ideal value would be 1, with values larger than one implying an overestimation and values smaller than one would mean underestimation. The columns intercept and slope give the values of the parameters of a linear regression between gauge and cross-validation values. They should be 0 and 1, respectively, if the cross-validation results were perfect. Finally the correlation of the data is given in the last row as another common measure of agreement. However, in order to assess the corrective power of an adjustment technique, the correlation can be misleading, as it only measures the linearity of the relationship and not whether the adjustment would produce a 1:1 agreement.

The first row shows the values obtained by comparison of unadjusted hourly radar accumulations with the gauge data. It shows the smallest root mean square and

Table 3.1.: Cross-validation results for the period 2008-05-01 – 2008-08-01

	RMSE	MAE	bias	intercept	slope	correl.
Radar	**0.771**	**0.414**	0.855	0.093	0.528	0.766
CCID	0.849	0.448	1.202	0.133	0.735	0.744
QQ	1.049	0.487	1.343	0.124	**0.909**	0.721
CCI	0.996	0.517	1.126	0.201	0.421	0.572
OK	1.026	0.523	1.156	0.197	0.464	0.567
EDK	0.928	0.491	**1.024**	0.093	0.765	0.758
CCID_A	0.975	0.452	1.216	0.105	0.847	0.734
Radar_A	0.831	0.434	1.108	**0.086**	0.805	**0.777**

mean absolute errors as well as the smallest intercept. However, as none of the other intercept values are particularly high, this measure of estimation quality is not very significant. The mean bias shows an underestimation of the gauge data by approximately 15%, while the slope implies an even larger underestimation by almost one half.

The second row, labeled 'CCID' contains the results for the censored copula interpolation with correlation adjusted radar as drift. Its performance is not particularly good in any of the categories presented, but it is not particularly bad in any measure either. The mean bias has become larger, similar to all other methods. The slope calculated for this method is 0.21 higher than that of the radar, showing that also some of the underestimation for large data has been removed. This can also be seen in the scatterplot in fig. 3.6a, where the radar data are given as gray triangles, and the adjusted estimates as black circles. The same figure shows that some of the changes are also due to some strong overestimations in the medium range of gauge measurements. Generally, correction has led to increased values, which improved on the underestimation especially for larger gauge measurements at the expense of a higher average bias. The correlation has not changed much between unadjusted radar and CCID estimates as the spread of the data has almost remained the same in addition to some large overestimations for smaller gauge measurements.

The following two rows, labeled 'QQ' and 'CCI' represent the results obtained by using the quantile-quantile transformation or the pure copula interpolation without radar drift, respectively. The numbers as well as the scatterplots in fig. 3.6 (c) and (d) show that both approaches would lead to worse results than the correlation adjusted drift. Here, even the very good slope estimate of the full drift version would be misleading, if the scatterplot were not consulted for comparison.

Ordinary Kriging does not improve with respect to any of the performance measures. External Drift Kriging does produce the best mean bias improvement, shows a good change in intercept and slope as well as a slight increase in correlation. The scatterplot (fig. 3.6f) shows some overestimations for medium gauge values, but in total a general tendency of correcting towards the 1:1 line. It should be noted that both Kriging variants also produce negative estimates, down to -11.1 mm in the EDK case. All of these negative estimates occur for small gauge values and might simply be set to zero in an operational setting. Transformation of the data or using

a residual map as drift as done by Velasco-Forero et al. (2009) may remove this issue as well.

As the CCID on attenuation corrected data is based on a different radar input data set, it is presented separately from the others in tab. 3.1. Accordingly, the points labeled 'unadj. radar' in fig. 3.6b originate from the attenuation corrected data of section 2.3, and not the clutter corrected data from section 2.2. The row labeled 'Radar_A' shows the statistics for the attenuation corrected radar data from section 2.3. The values differ slightly from the values in tab. 2.4 due to the different filtering constraints as mentioned above. It can be seen again, that the bias is changed from under- to overestimation by the attenuation correction. While row 'CCID_A' does not show major improvements as compared to row 'Radar_A', it can be seen in fig. 3.6b that the CCID-approach is effective in removing some of the worst overestimations, while retaining some of the values of the attenuation correction for the higher gauge values.

Stratiform Event The results for the three month period presented so far might give the impression that none of the adjustment techniques are able to provide significant correction. This may be due to the fact that this period is dominated by convective or other small scale events. In such cases, the probability is high, that neighboring gauges may provide very different measurements, making it hard for the interpolations (which all of the presented methods still are) to recreate the value for a missing measurement during cross-validation.

Therefore a second analysis was conducted focusing more on a stratiform event, where gauge measurements could be expected to be more similar over larger areas. By analyzing the available radar images for wetted area ratio and image mean flux (see Ehret (2003) for their definitions) a period between 2009-07-14 20:50 UTC and 2009-07-15 12:50 UTC was found, where most of the radar umbrella had been covered by appreciable precipitation. The data was then analyzed in exactly the same way as had been done with the previous three-month period, and the results will be presented accordingly as follows.

Table 3.2 gives the numerical statistics of the cross-validation. Bias, slope and correlation of the original radar data are much higher than in the previous case, indicating a much better agreement between radar and gauge from the start. The intercept is also noticeably higher, meaning that still significant overestimation occurs for low gauge values.

Applying CCID leads to an improvement with respect to all measures except bias. Again, it can be seen that reducing the influence of the radar according to radar-gauge correlation is beneficial to the adjustment. QQ leads to generally higher errors and larger spread around the 1:1 line (c.f. fig. 3.7c). Although, numerically the slope is slightly better than that of CCID, the correlation is much smaller. CCI shows the opposite behavior. While the homogeneity of the field helps the pure interpolation to achieve good results at the location of the left-out gauge, there is still a tendency for underestimation at higher intensities (resulting in a much smaller slope and the visual pattern in fig. 3.7d).

The Kriging methods both perform very well in this setting. Especially the External Drift Kriging produces four out of six of the best performance measures for this

Table 3.2.: Cross-validation results for a stratiform event

	RMSE	MAE	bias	intercept	slope	correl.
Radar	1.287	0.746	1.030	0.491	0.620	0.812
CCID	1.086	0.682	1.076	0.289	0.835	0.874
QQ	1.655	0.804	1.143	0.330	0.864	0.757
CCI	1.056	0.699	1.012	0.354	0.717	0.879
OK	1.031	0.680	**0.997**	0.290	0.756	0.883
EDK	**0.855**	**0.622**	0.996	**0.156**	0.879	**0.927**
CCID_A	1.013	0.671	1.081	0.306	0.819	0.885
Radar_A	2.177	1.012	1.712	0.723	**1.095**	0.764

data set. Low spread, and especially a very good correction of the largest intensities lead to a good regression slope as well as a very high correlation. A few negative estimates still remain, yet less pronounced as in the other example.

When looking at the statistics as well as the scatterplots (fig. 3.7b) for the attenuation corrected case, the corrective power of the CCID method can clearly be appreciated. The adjustment corrects the overestimations at small intensities (0-5 mm), while preserving most of the attenuation correction for the medium to high intensities. The differences between CCID and CCID_A are not large enough to be called significant. Yet, both produce similar results, despite using quite different radar information.

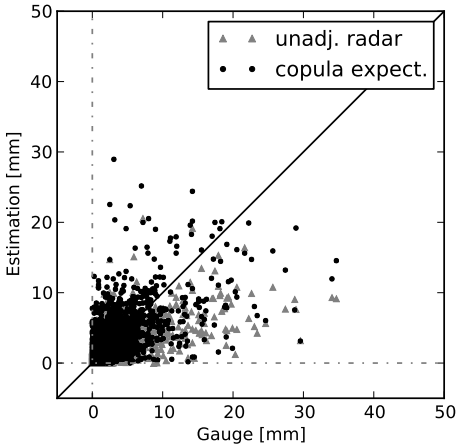

(a) Copula interpolation with correlation-adjusted drift (CCID)

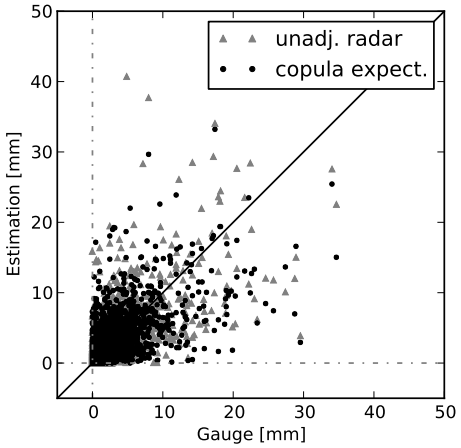

(b) Copula interpolation with attenuation corrected radar data (CCID_A)

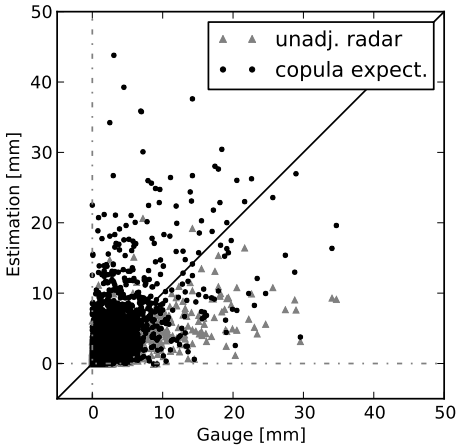

(c) Quantile-Quantile transformation (QQ)

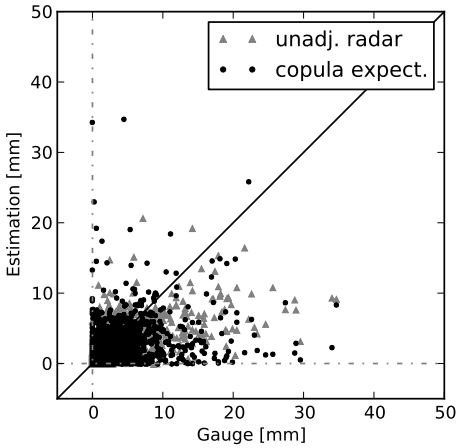

(d) Copula interpolation without radar (CCI)

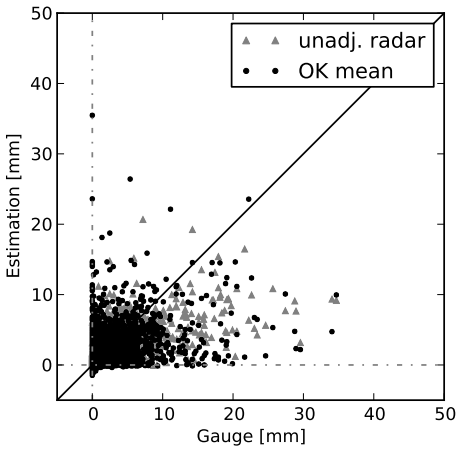

(e) Ordinary Kriging (OK)

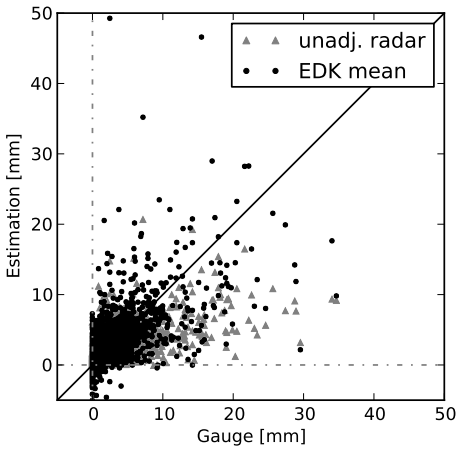

(f) Kriging with radar as external drift (EDK)

Figure 3.6.: Scatterplots comparing cross-validation estimates of different methods to gauge measurements during the period May through August 2008

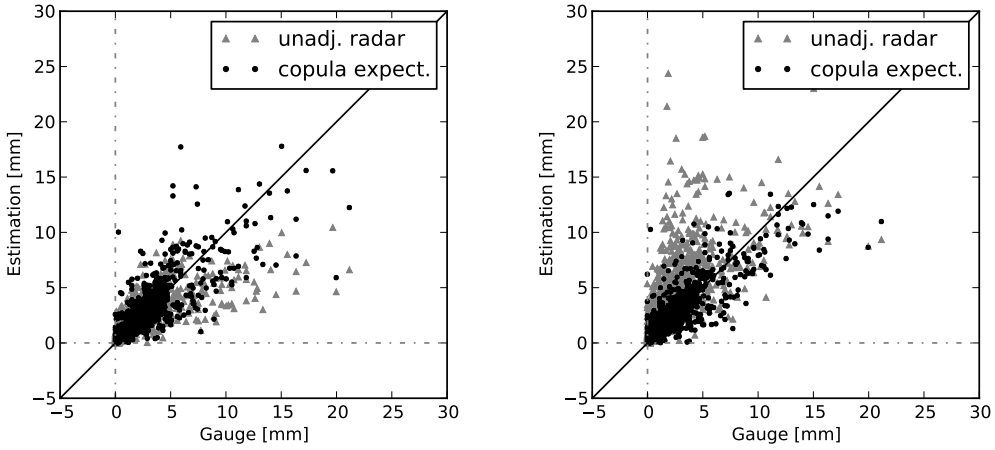

(a) Copula interpolation with correlation drift (CCID)

(b) Copula interpolation with attenuation corrected radar data (CCID_A)

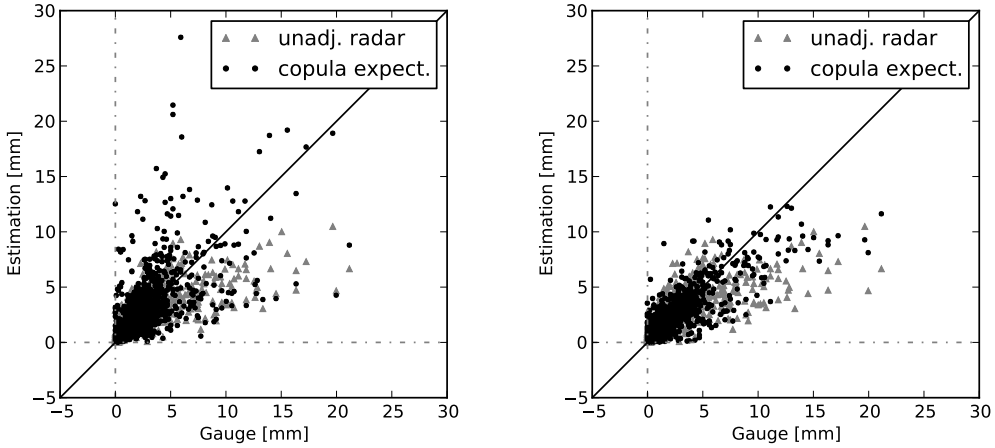

(c) Quantile-Quantile transformation (QQ)

(d) Copula interpolation without radar (CCI)

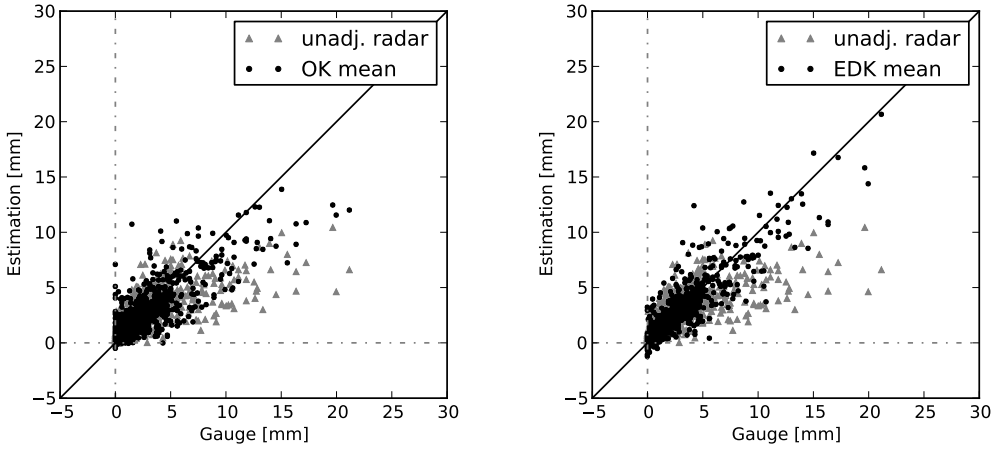

(e) Ordinary Kriging (OK)

(f) Kriging with radar as external drift (EDK)

Figure 3.7.: Scatterplots comparing cross-validation estimates of different methods to gauge measurements for a stratiform event (2009-07-14 20:50 – 2009-07-15 12:50 UTC)

3.4.4. Uncertainty Analysis

One advantage of geostatistical methods over other interpolation approaches like inverse distance, splines etc. is that they provide an estimate of the uncertainty in addition to the interpolated value.

For Kriging, this is given by the estimation variance.

Together with the interpolated value, which is the expected value of the ReV at the interpolation point, by virtue of the derivation of the Kriging equations, a normal distribution with that mean and variance can be defined as the conditional distribution at that point.

For the copula interpolation methods, the full distribution is obtained during interpolation. For the Gaussian Copula, this also reduces to finding a conditional mean and variance, but during back transformation from copula space to data space, the final distribution may change considerably.

One common measure to assess whether the uncertainty estimates are realistic is to evaluate the distribution of the quantiles of the gauge measurements during leave-one-out cross-validation. In that process, the conditional distribution is calculated at the location of a gauge, which previously had been removed from the data set. Now, instead of comparing the expectation to the gauge value, the value of the conditional distribution function is evaluated for the gauge measurement. This value is designated as the quantile $q(G)$ of that particular gauge value G, and it is calculated for the Gaussian Copula case as follows:

$$q_{Copula}(G) = F_{N(\mu_c,\sigma_c)}\left(F^{-1}_{N(0,1)}\left(F_G(G)\right)\right) \tag{3.23}$$

Here, F_G stands for the empirical distribution function of the gauges as obtained by kernel density estimation (sec. 3.4.2), $F^{-1}_{N(0,1)}$ is the inverse of a standard normal distribution and $F_{N(\mu_c,\sigma_c)}$ is the normal distribution function with conditional mean μ_c and standard deviation σ_c as calculated during interpolation.

For the Kriging variants the quantiles would be obtained according to

$$q_{Kriging}(G) = F_{N(\mu_k,\sigma_k)}(G) \tag{3.24}$$

with μ_k and σ_k representing the Kriged estimate and the square root of the Kriging estimation variance, respectively.

If the interpolation is unbiased and the conditional distribution – and thus the uncertainty – is estimated correctly, the resulting quantiles should be uniformly distributed.

This analysis was conducted for the five interpolation methods that would allow the estimation of a conditional distribution, which are CCID, CCID_A, CCI, OK and EDK. In the following the results of CCID_A were omitted as they did not differ significantly from that of CCID. Fig. 3.8 gives the distribution of the quantiles for each of the estimation variants for all gauge values. Due to the large range of density values, a logarithmic y-scale has been used. As the distribution should have a uniform density of 1, this value has been highlighted by the dotted horizontal line.

Figs. 3.8 (a) (b) show a similar behavior of low densities at smaller quantiles and very large densities at higher quantiles. This behavior is to be expected, if the general location of the conditional distribution is systematically too low with respect to the

reference and the spread of the distribution is too small. The CCID method shows a small plateau of almost constant density between 0.3 and 0.8 and can therefore be said to perform slightly better than the copula interpolation without the radar data as drift. One reason for the high densities at large quantiles is the treatment of zeros. Due to the fact that the censored interpolations in principle allow values below zero, whereas the gauge data are never smaller than zero, puts the gauge zeros preferably into the higher quantiles of the conditional distribution. If the gauge data were represented in the same way they were used during interplation, by $p_0/2$, for example for the CCID estimates, a similar distribution as with the EDK method would result.

Both Kriging variants show peaks of densities at 0, 1 and around 0.5. This means that, while the majority of gauge measurements falls around the Kriged estimate, the estimation variance is calculated too large for most values and too small for others.

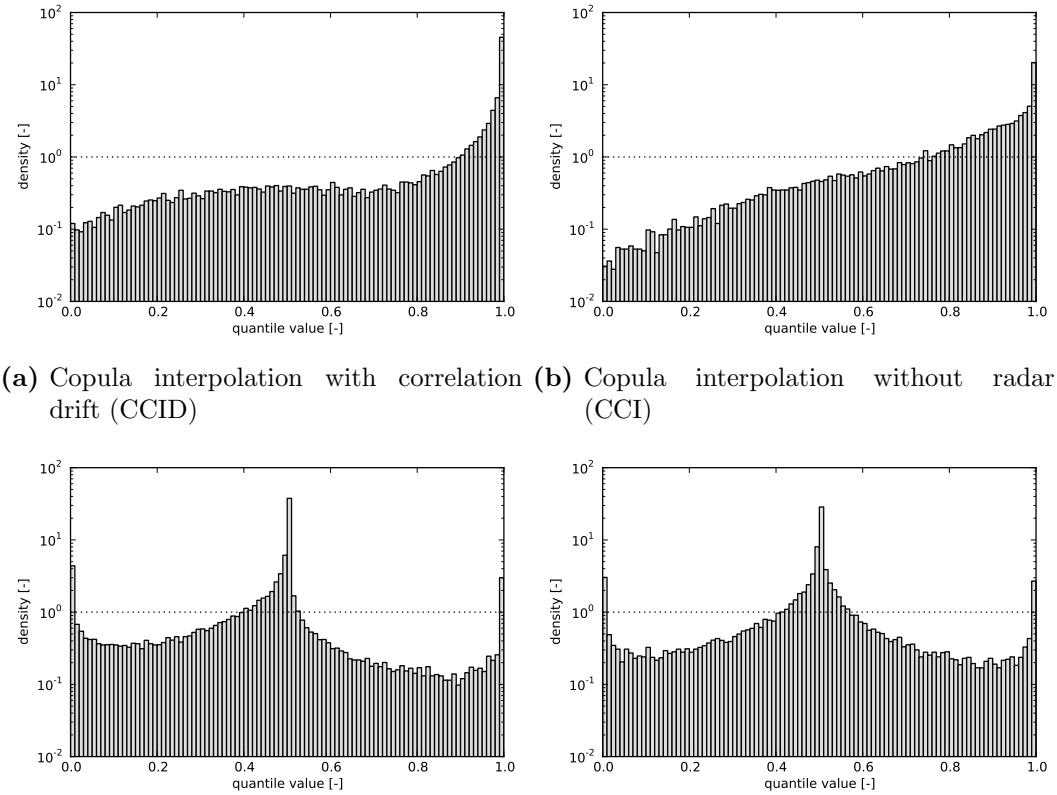

(a) Copula interpolation with correlation drift (CCID)

(b) Copula interpolation without radar (CCI)

(c) Ordinary Kriging (OK)

(d) Kriging with radar as external drift (EDK)

Figure 3.8.: Distribution of quantiles of gauge measurements as estimated from conditional distribution during cross-validation. Period 2008-05-01 – 2008-08-01

Given the aforementioned problems of properly representing gauge measurements of zero in the conditional distributions, and the fact, that from the viewpoint of flood forecasting, the higher precipitation amounts are of more interest, the same analysis was conducted with a threshold of 1 mm/h applied to the data.

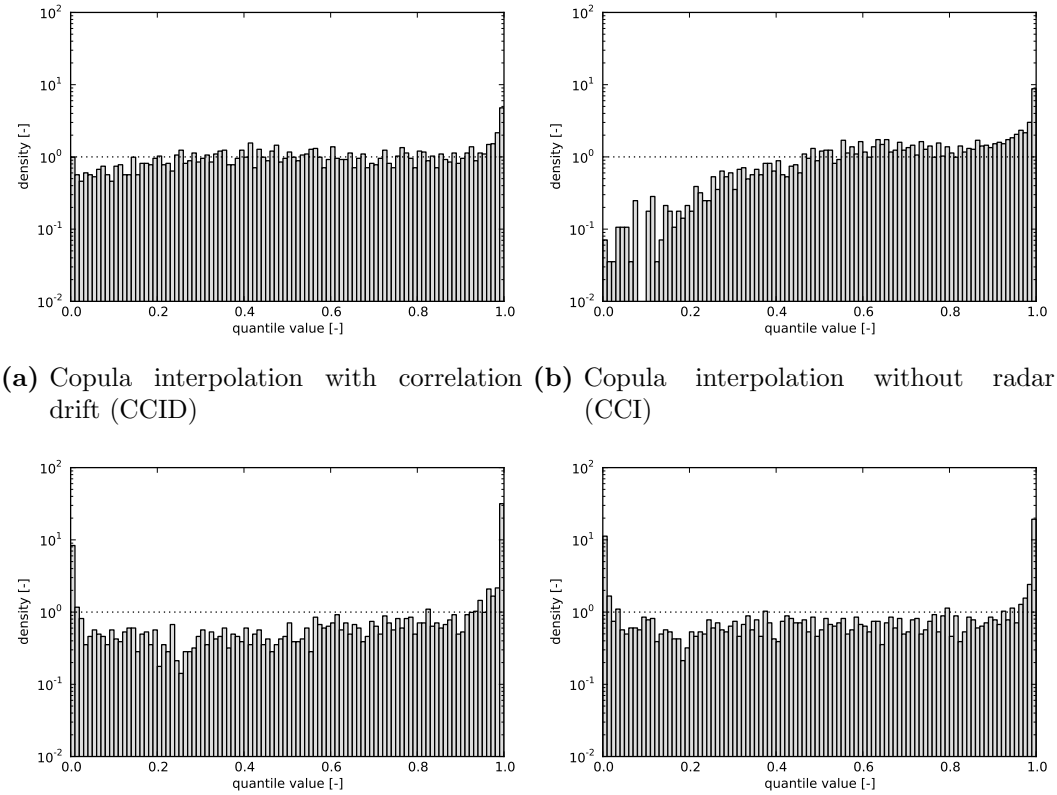

(a) Copula interpolation with correlation drift (CCID)

(b) Copula interpolation without radar (CCI)

(c) Ordinary Kriging (OK)

(d) Kriging with radar as external drift (EDK)

Figure 3.9.: Distribution of quantiles of gauge measurements as estimated from conditional distribution during cross-validation for gauge values larger than 1 mm/h. Period 2008-05-01 – 2008-08-01

The resulting quantile distributions are presented in fig. 3.9. All distributions have become more uniform than without the threshold, although the CCID method shows the smallest deviations, which are nevertheless still present at the highest quantiles. The pure copula interpolation (CCI) shows systematic underestimation, while the Kriging variants both show a similar behavior that now hints at an underestimation of the error variance.

3.4.5. Summary

This chapter presented several analyses of the spatial structure of rainfall fields as observed by weather radar.

The first was whether the reflectivity measured by the radar could be assumed to be a weighted average of some point scale stochastic process for which the variogram ought to be found. This assumption can be physically justified by the fact that the reflectivity has been derived as the sum of the sixth power of the individual drop diameters in the measurement volume (eqn. 2.14). Inhomogeneous beam filling, vertical profile effects, different precipitation phases etc. put more or less strong

limits to this assumption.

The point support variogram was attempted to be estimated using two approaches. The first aimed at inverting the convolution, which had been shown to have been successful with satellite imagery. The greatly differing averaging sizes in addition to effects from locally differing structures made it impossible to distinguish the small regularization signal from the surrounding noise. An averaging over time did not help to reduce the noise as it introduced other noises due to advection and the temporal evolution of the radar field. The second approach tried to model the regularization effect based on an assumed knowledge of the underlying point support variogram and to find the variogram that would maximize the likelihood of observing a given precipitation field. While this method could be applied to individual images, thereby reducing the effects of advection and temporal smoothing, the results obtained were not in accordance with theoretical considerations. Further attempts may be more successful, if they were, for example combined with the censoring and copula approaches presented in the second part of this chapter.

Given that the effect is small and only affects interpolation estimates for very small separation distances, while the computational demand is very high, its priority for operational application will be very low.

The second part of the chapter presented a new method for gauge adjustment for radar data introducing three new concepts to this topic.

First, a Gaussian Copula interpolation approach was used to provide conditional distributions at each interpolation point, separating the spatial dependence from the marginal distributions. Second, no-rain data was explicitly modeled using a censoring or latent variable approach. The censoring threshold was determined from the radar data, as it had been shown that an estimate from the gauge data could result in greatly varying values depending on the network's configuration. Using the censoring assumption the spatial structure was determined using a maximum likelihood approach. Third, the interpolation was conditioned on the radar data, based on the correlation between radar and gauge measurements. Accounting for the agreement between radar and gauge was shown to provide significant improvement as compared to full conditioning or completely ignoring the radar data.

While other adjustment methods were able to provide better results in certain settings, the method produces stable and consistent results. Finally, an uncertainty analysis showed that the conditional distribution of the full method captures the interpolation uncertainty much better than any of the comparison methods. This is an important property for Monte Carlo simulations of precipitation fields, which could be used to create hydrological model ensembles.

It should be noted that three optimizations are used during the estimation process. These need to be done for (i) the maximum likelihood estimations of the variogram, (ii) the kernel smoothing bandwidth for the gauge marginal distribution and (iii) the correlation between gauge and co-located radar measurements. If any of these optimizations fail, the method as a whole is most likely to produce erroneous results. This has to be kept in mind and accounted for, before the method can be used routinely e.g. to produce input time series for hydrological modeling.

4. Hydrological Implications

4.1. Introduction

In the preceding chapter, several precipitation estimates have been presented and compared with respect to their agreement with ground measurements.

While cross-validation is a well accepted and widely used method, it does not capture all aspects of precipitation fields that would be relevant for hydrology. As was seen, for example, during the estimation of the non-raining fraction p_0 of a radar image in section 3.4 (pp. 56), the gauge measurements can hardly be assumed to be representative for the entire field. This has also been discussed by other authors (Kitchen and Blackall, 1992; Michelson and Koistinen, 2000; Seed et al., 2007), and even if gauge measurements could be taken at a very high resolution, significant variability would still remain (Ciach, 2003).

When using precipitation estimates as input to a hydrological model, much of this variability would be filtered out by the catchment processes. For lumped modeling, only the areal integral would be used, removing all spatial variability. In semi-distributed modeling different traveling times might be taken into account, integrating over areas of equal travel time. Only in fully distributed modeling, would the complete spatial distribution of the precipitation be taken into account. However, interception, soil moisture storage, evapotranspiration, aquifer storage, snow melt and accumulation also affect how variability in the precipitation input is transferred to or removed from discharge variability. While these processes provide mainly temporal filtering to the precipitation input, considering them in a spatially distributed way will provide an indirect spatial filtering as well.

Assuming a model based solely on mathematical representations of physical processes with parameters derived from measurements of catchment properties, different precipitation input should lead to different discharge response and, ideally, the closer a precipitation estimate would be to the real precipitation, the better the modeled discharge would agree with the observed discharge. This way precipitation estimates could be evaluated directly on the scale of interest for the hydrologist.

The structure of most current hydrological models, however, relies on the estimation of some of the model parameters based on past observations, tuning the model such that given some meteorological forcing, the model would provide the best agreement with the observed discharge. This process is usually referred to as model calibration. This approach ties a certain set of parameters not only to the catchment, but also to its input, including the precipitation estimates. Bárdossy and Das (2008) showed that even small changes to an observation network would strongly affect the parameters received during calibration. The same problem can be expected, when dealing with precipitation estimates derived from different data sources or by different methods, for example those presented in the previous chapter. Indeed, several authors report this dependence of model parameters on the precipi-

tation input (Yilmaz et al., 2005; Vieux and Bedient, 2004; Cole and Moore, 2008) and the resulting problems to properly compare the results of hydrological models driven by different precipitation estimates.

Gourley and Vieux (2005) and Heistermann and Kneis (2011) took a different approach. Based on the assumption that, on the whole a better precipitation estimate should lead to better discharge simulations regardless of parameter choice, they either varied some of the parameters systematically (Gourley and Vieux, 2005), or randomly (Heistermann and Kneis, 2011), and assessed the distribution of model performances for the different precipitation inputs.

As Heistermann and Kneis (2011) point out, the calibration may compensate for some biases in a precipitation estimate. Especially linear biases like a constant over- or underestimation may easily be remedied by adjusting soil moisture capacities or evapotranspiration fluxes, thus removing more or less water from the system. Other, more subtle compensatory changes in differing parameter sets may not be as easily rationalized and may well go unnoticed. In addition there is no guarantee that model performances will actually be better for the majority of parameter sets. Assuming that the objective function defined by the chosen performance measure is reasonably smooth (which may be doubted as well, given the results of Kavetski et al. (2006) and Kavetski and Kuczera (2007)), this should be true at least in the vicinity of the optimal parameter set for each input. However, if two different inputs produce largely differing parameter sets, this condition may not be met and results may become meaningless.

This applies both for lumped as well as distributed models. A study by Mosthaf (2012) applied several unit hydrograph methods and an HBV model to several catchments in South-Western Germany, using different precipitation estimates as input. Neither the simple unit hydrograph models, with their minimal number of parameters, nor the more complex HBV model (with already 12 calibration parameters) would provide conclusive results on which precipitation input could provide the best fit to the observed discharge.

Distributed modeling may therefore be the only way to properly represent the small scale variability measured by weather radars. Their increased complexity, however, will also provide additional uncertainty and possibilities for the model to compensate certain biases.

Instead of attempting a hydrological verification, which may well fail for the reasons given above, this chapter will analyze the precipitation estimates from the previous chapter with respect to their spatial properties, how they differ among each other and what implications this may have on their use with hydrological models.

4.2. Scale Analysis

In order to do the analysis, the data of the precipitation estimates by CCID, CCI, QQ, OK and EDK for the area and time period presented in the previous chapter were first transferred from polar to Cartesian coordinates. This produced an hourly time series of raster images of approximately 256x256 pixels, for the period of May to August 2008, which represented the finest scale of analysis. The next scale was generated by producing an image from 2x2 averages of the pixels of the finest scale.

This image would have only a quarter of the original number of pixels. The next scale is then obtained by repeating this process of aggregation on the previous image, and this is repeated until only one pixel remains. This way, nine image scales were created ranging in integration size from 1 to 65536 km^2.

It should be stressed again that *none* of the following analyses is intended to provide any assessment of the relative qualities of the studied estimation procedures. Their aim is rather to try and quantify how different the estimates are on different aggregation scales and thus how different a hydrological response could be expected, for the better or worse, for each precipitation input.

This is different from the cross-validation with gauge data as reference from the previous chapter in that there only the individual agreement at a few points was measured, while this section tries to answer the question on whether differences between estimates persist even when averaging over larger areas, or from which point on gauge interpolations would be as useful as high resolution precipitation data.

4.2.1. Global Analysis

A first question may be, whether there would be a scale at which the differences between the individual estimates disappeared. In lumped modeling, this would be the scale, where also the hydrological response of a catchment would be independent of the chosen estimate. While there may be some differences when using a distributed model, it may be expected that these differences would also gradually disappear from this scale on.

For this purpose, the global differences between the precipitation estimates presented in chapter 3 were calculated. This was done by calculating measures of agreement between two estimates, similar to the cross-validation analyses presented in section 3.4.3.

Given the fact that the most commonly used precipitation input to current hydrological models is gauge interpolations, it was decided to use the Ordinary Kriging estimates as the reference for all following analyses.

All measures were calculated over the whole dataset for one particular scale, so, for example the RMSD for the 1 km^2 scale of CCID is the square root of the mean difference between all square kilometer pixels of the CCID dataset and the co-located pixels of the Ordinary Kriging dataset. MAD, (Pearson-) correlation and bias, defined as the ratio of the means of the two respective data sets, were calculated accordingly for each precipitation estimate and scale.

The difference and correlation plots generally show an increase in similarity between the estimates when averaged over larger areas. As the Copula interpolation also uses gauge data only, differences between its estimates and those obtained by Ordinary Kriging are lowest both in the root mean square (fig. 4.1a) as well as in the absolute sense (fig. 4.1b). Accordingly, correlations between the respective estimates are also the highest on every scale. The fact that the differences remain the same up to a scale of 100 km^2 and above may be due to the smoothness of the interpolated fields.

The pure quantile-quantile transform of the radar data provides the largest differences and the lowest correlations with the Ordinary Kriging data. The two methods, which incorporate both information from radar and gauge, range in between these

extremes. It may also be seen that, while the differences become smaller, they never reach zero even for the largest aggregation scale.

This is most probably due to the remaining systematic differences like over- or underestimations relative to each other. Fig. 4.1d shows a somewhat unexpected behavior for the biases of both copula interpolations and the quantile transformation. There, only the External Drift Kriging shows a change in bias towards 1.0 at larger scales, while the other three variants show a similar behavior but on different levels of bias and without the bias vanishing with increasing aggregation. This behavior might be connected to the negative estimates of the Kriging variants seen during cross-validation (c.f. figs. 3.6 (e) and (f)), which were not removed before aggregation, while negative values were filtered before averaging the values to produce the plots in fig 4.1.

The fact that RMSD in fig. 4.1a is larger than the respective MAD in fig. 4.1b by approximately a factor of 5 for each estimation method (except for QQ, where it is almost a factor of 10) shows that the distribution of differences is skewed with a few large differences.

Threshold processes play an important role in the formation of floods. In small catchments infiltration excess caused by intensive rainfall is the major process leading to flash floods. Saturation excess after longer periods of widespread rainfall produces

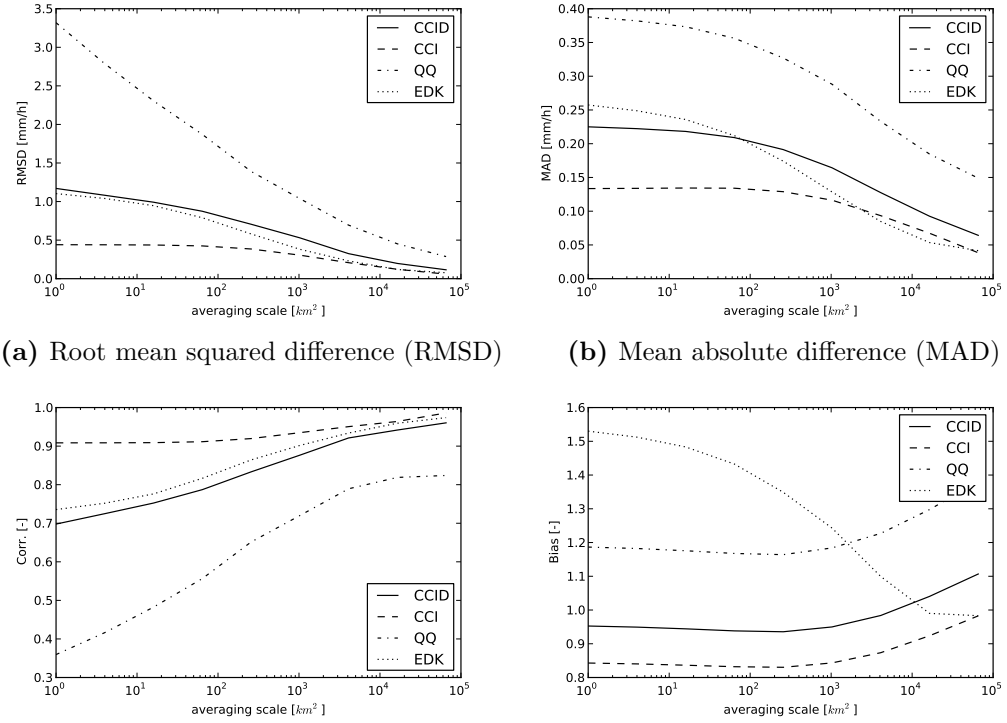

(a) Root mean squared difference (RMSD)

(b) Mean absolute difference (MAD)

(c) Correlation

(d) Bias

Figure 4.1.: Similarity measures for different precipitation estimates with Ordinary Kriging as reference over averaging scale. Only aggregate values larger than 0 were used for analysis

floods in larger catchments. In order to put more weight on the data that would actually trigger the former process, the data was thresholded for larger intensities and the analysis was conducted again on the filtered data set. Thresholds of 1 mm/h and 5 mm/h were chosen in order to distinguish between medium and intense rainfall. This poses a problem for the larger scales as less and less data that exceed this threshold are available after averaging, leading to spurious results especially for the correlation.

Nevertheless, there are some insights to be gained from this exercise. When looking at the 1 mm/h threshold (fig. 4.2), the differences between the alternative estimation methods become larger. Consequently, the correlations between the variants and ordinary Kriging become smaller. It is interesting to note that the external drift Kriging estimates become more similar to those of the pure gauge based interpolations than those of the CCID method. For aggregations between 10^3 and 10^4 km^2 differences between the gauge interpolations and EDK mainly vanish, which would mean that hydrological responses to those estimates may also be expected to become similar for medium to larger sized catchments. On the other hand, CCID or QQ estimates might still lead to different results in modeled discharge.

Fig. 4.2d in comparison with fig. 4.1d shows the effect that the many small and zero precipitation values have on the analysis. With the smallest values removed, the mean bias shows the expected behavior of dropping towards 1 for larger averaging scales. The sudden drops in correlation for the largest aggregation scales may, however, be due to insufficient sample sizes to reliably calculate this statistic. Therefore, although the results appear plausible, the values for all other measures should be treated with caution for the largest scale as well.

To further investigate the scale behavior of the different estimation variants for higher precipitation rates, a threshold of 5 mm/h was applied to the data before differences were calculated. While 5 mm/h may not sound much on the 1 km^2 scale, over an area of 64x64 km^2 it would produce runoff of over 5000 m^3/s. Fig. 4.3 shows the same scaling behaviors for this threshold as the other two, with the initial differences being higher than for the smaller thresholds. Accordingly, the correlations between the high intensity estimates becomes smaller, while the relative biases approximately remain the same. Only after averaging over more than 10^3 km^2 the differences gradually disappear.

4.2.2. Image Analysis

While the preceding global analysis showed the differences between the precipitation estimates, the image analysis tries to give an additional insight into the relative spatial variability of each variant. From the hydrological point of view, spatial variability leads to the activation of threshold processes in some places, while storage and retention capacities in other areas may still be large enough to accommodate additional rainfall. Aggregation over larger scales smooths out some of this variability. Lumped models or models with coarse spatial resolution would need to adjust their thresholds and related parameters in order to provide the same runoff behavior as models with a finer spatial resolution.

The most common summary statistic of variability, the standard deviation, was calculated for each image of the analysis period (2008-05-01 – 2008-08-01) and each

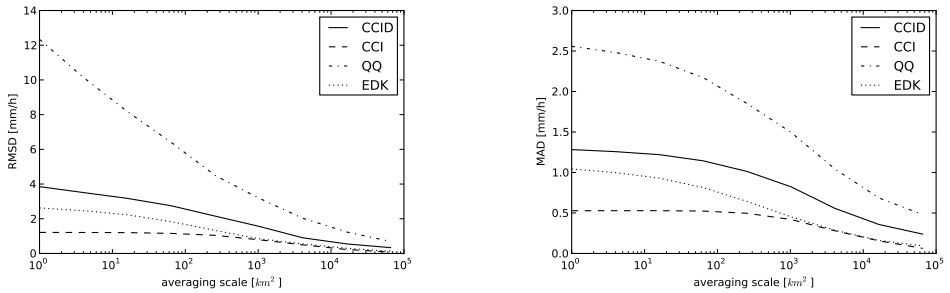

(a) Root mean square difference (RMSD)

(b) Mean absolute difference (MAD)

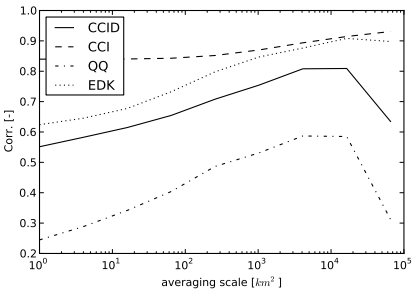

(c) Correlation

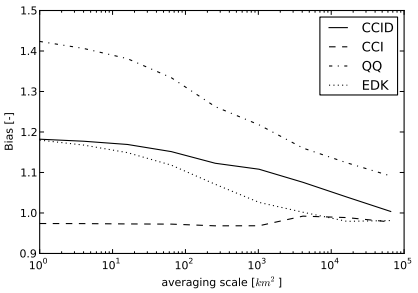

(d) Bias

Figure 4.2.: Similarity measures for different precipitation estimates with Ordinary Kriging as reference over averaging scale for precipitation threshold of 1.0 mm/h

estimation method. Afterwards, all data were standardized individually to the values of the Ordinary Kriging variant for each timestep and finally averaged over time to produce one value per variant and aggregation scale.

The results of this analysis are shown in fig. 4.4. The image standard deviation shows that the QQ-method produces the largest variability in space, which is on the finest scale almost 2.5 times larger than that of Ordinary Kriging. Even for the largest possible aggregation scale of 128x128 km^2 (at 256x256 km^2 only one pixel remains and no standard deviation can be calculated) it is still 50% higher than the Kriging variability. The interpolations including radar information (EDK and CCID) also show higher variability than Ordinary Kriging. However, beyond aggregation scales of 10^3 km^2 this difference becomes very small. The pure copula interpolation shows even less variability than the reference and remains like this, even at large aggregations.

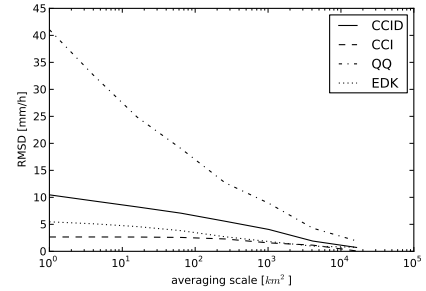

(a) Root mean square difference (RMSD)

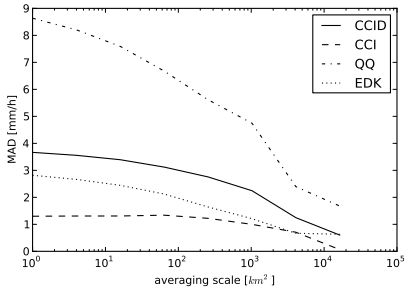

(b) Mean absolute difference (MAD)

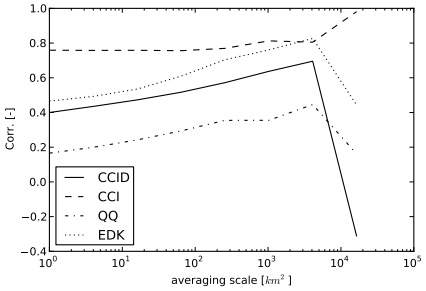

(c) Correlation

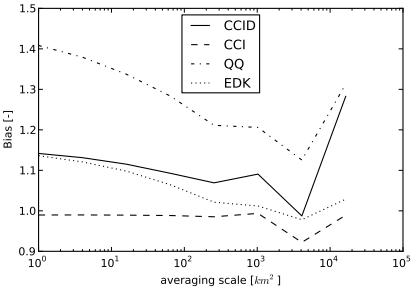

(d) Bias

Figure 4.3.: Similarity measures for different precipitation estimates with Ordinary Kriging as reference over averaging scale for precipitation threshold of 5.0 mm/h

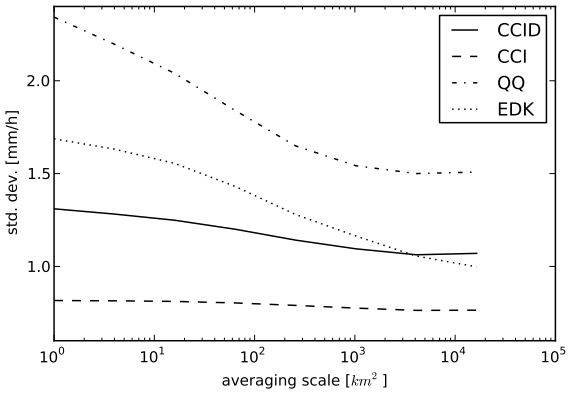

Figure 4.4.: Time averaged normalized image standard deviation (normalization per timestep to values of Ordinary Kriging variant)

4.2.3. Catchment Example

All previous analyses showed that there is considerable difference between all precipitation estimates over a wide range of scales. The scales had been constructed by partitioning a Cartesian grid. To see how the differences would appear for a particular catchment, aggregation was done for the area of the discharge gauge Rangendingen/Starzel. The resulting time series can then be displayed conveniently in a scatterplot, giving the best indication of variability and agreement between the different estimates. In fig. 4.5 one can see that each estimate produces very different results. While all dashed regression lines lie very close to the dotted 1:1 line, only the copula interpolation without drift (fig. 4.5b) shows very small spread around it. The catchment has an area of 123 km^2 and therefore presents a scale at which the previous results showed clear differences between estimates. This is again confirmed by this analysis.

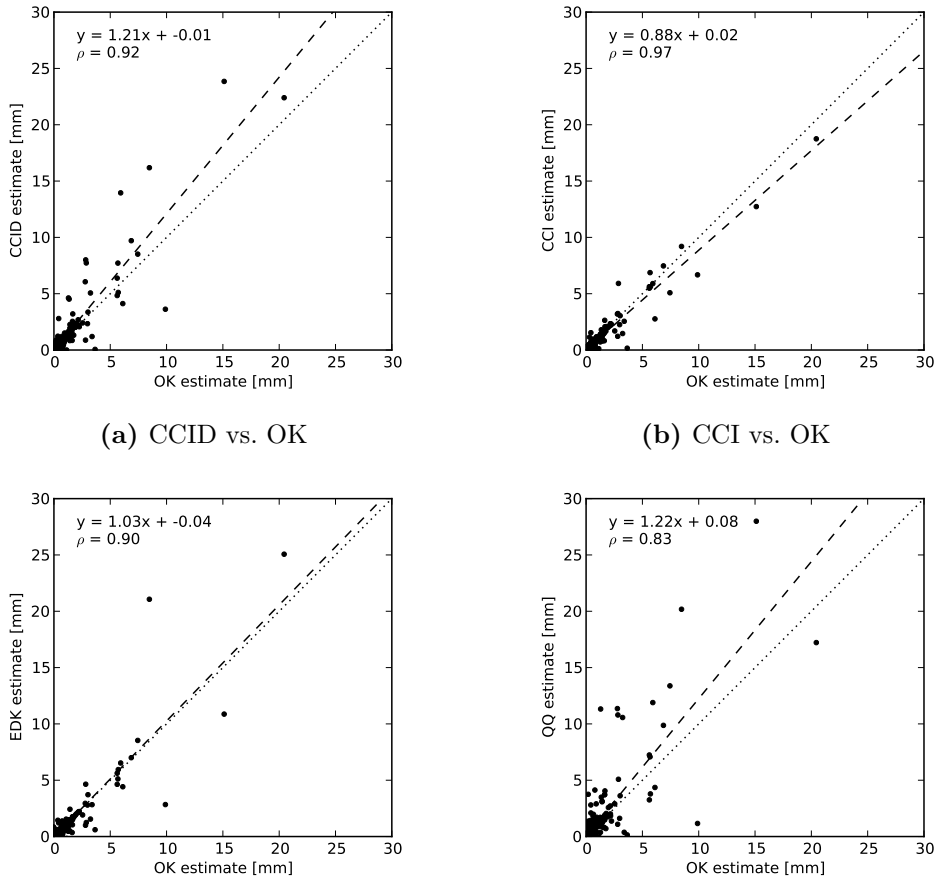

(a) CCID vs. OK

(b) CCI vs. OK

(c) EDK vs. OK

(d) QQ vs. OK

Figure 4.5.: Scatterplots comparing the different precipitation estimates with Ordinary Kriging as reference. Aggregation over the Starzel catchment (gauge Rangendingen). The parameters of the dashed linear regression line as well as the correlation coefficient for the data are given in the respective panels

4.3. Summary

In this chapter different analyses regarding the differences between precipitation estimates on different scales have been presented. A global analysis removing all spatial and temporal connections between the data, showed that differences for complete datasets tend to diminish between 10^3 km^2 and 10^4 km^2. For higher precipitation intensities dissimilarities prevail even over larger areas. This means that for example for flood forecasting the most important periods will be the ones that will show the biggest differences. Whether this will improve the identifiability of the 'best' estimate or just lead to more spread needs to be investigated.

The comparison also showed that each estimate has a distinctive bias when compared with the other variants, which also disappears over larger scales. This will definitely affect parameter estimates during model calibration and as such lead to different model behaviors making comparisons difficult. Many hydrological models consider evaporation from soil and vegetation. As mentioned earlier, one easy way to deal with constant precipitation biases would be to increase soil moisture storage capacities and evaporation rates. One way to separate 'good' precipitation estimates from 'worse' ones could therefore be to see, whether one of them produces unrealistically high or low evaporation rates. If parameters like field capacity or wilting point are not calibrated but determined from soil and land use maps, bias compensation might be reduced even further.

The image analysis, which considered the spatial variability of the estimated fields also showed that each approach has its distinctive signature with the radar data introducing a significant amount of variability, which also only partly disappears after averaging over areas larger than 1000 km^2. Therefore, distributed modeling should be expected to benefit most from radar data on scales below 10^3 km^2, while above that simple interpolation of gauge data might work as well.

The detailed analysis of the areal integrated precipitation time series for the small Starzel catchment gave an example on how different the precipitation amounts are that each estimation method provides. Although the retention and translation processes are expected to smooth a lot even of this variability, the question remains, whether all estimates could really be interpreted as realizations of the true catchment rainfall, and how these differences would really affect parameter estimation.

One might ask, whether this would be the right direction at all. It might be argued that given the low resolution input of interpolated gauge measurements uncalibrated models might not have produced useful results, even if all other model components had been able to represent the water storages and flows correctly, given the right forcing. Parameter estimation made it possible to produce models useful for flood and drought forecasting at the expense of not always knowing exactly what a certain parameter value meant for a specific catchment and not being able to separate catchment characteristics from input characteristics.

It may be an interesting exercise to challenge the currently available hydrological knowledge about processes and pathways to build a model and try setting all parameters formerly calibrated only based on hydrological and physical reasoning. With parameters only changed on the basis of new knowledge about the catchment properties, such a model should be able to identify much better, which precipitation input is closest to the real one.

5. Conclusions

In this thesis three areas of processing and analysis of weather radar were addressed aiming at improving its usefulness for hydrological applications.

The first part dealt with deterministic corrections of the data in order to improve its overall quality.

A clutter filter has been implemented and adjusted with a focus of removing false positives during intense convective events. Although corrected accumulations showed a significant decrease of overestimations due to clutter for many areas, in others residual clutter remains. Given the relative simplicity of the employed algorithm, adding a few additional checks and conditions might improve detection results. However, there will always be clutter conditions which will elude even the most elaborate filter, as long as the only information available is two-dimensional images. Adding more information (see tab.2.2), especially in the vertical, is expected to provide better results at the expense of increased complexity of the methods to be employed. Nevertheless, many datasets are still around that only provide two-dimensional reflectivity information, and for these, the presented clutter mitigation techniques will still be useful. This way radar precipitation time series may be increased in length by several years, which would improve the significance of any hydrological study.

At C-Band and higher frequencies, attenuation becomes a serious issue, especially in the case of flood relevant intense precipitation. The constrained iterative forward correction by Krämer (2008) had been extended by an additional constraint on the maximum path integrated attenuation. This was shown to produce stable results, which also appear reasonable for long term accumulations. On the point scale, overestimations for medium intensities were observed, while good results were achieved for the higher intensities. Presumably, this is the best result that may be obtained without an additional attenuation reference (either by virtue of commercial or dedicated microwave links, or, if available, by using the mountain reference technique), or networked observation of the same precipitation field from different directions by multiple radars, which is an upcoming topic especially for low-cost X-Band radars. Also, the real potential of the initial proposition of Hitschfeld and Bordan (1954) to calibrate the attenuation correction with the help of gauges has not been investigated yet. One would have to be careful not to correct other range dependent errors using this approach, but assuming effect of the vertical profile of reflectivity have been accounted for, a relaxed conditioning of the attenuation correction on gauge data might show good results. For this approach, the linear formulations of Marzoug and Amayenc (1994) should be preferred over the recursive scheme of Hitschfeld.

The third deterministic correction investigated was an advection aware accumulation scheme. Even though the results did not show a significant quantitative improvement, the resulting accumulated fields appear much more realistic, especially for fast moving storms. In addition a comparison between several advection estimation algorithms showed the remarkable robustness of the not well known approach

of Bouguet and Others (2000), which combines a fast, gradient based estimation of displacement with searches on multiple image scales. Having a robust advection estimation algorithm at hand is also a first step towards a reliable nowcasting of precipitation.

In chapter 3 a new method of adjusting radar data to gauge measurements was presented, which introduces several new approaches to the topic. First, copula interpolation was used to transfer the gauge values to ungauged areas. Separating the marginal distribution from the dependence structure enables separate modeling of these two and obviates the need for distributional assumptions, which are, for example, implied when using methods based on Kriging. Although only the Gaussian Copula was used in this thesis, other copulas could be tested, if their dependence structure would provide improved results. The copula approach itself was then extended by assuming zero precipitation values to represent a censored value instead of the zero value itself. This allows their handling in a mathematically elegant but also physically plausible way, without having to resort to indicator fields, separating occurrence from amount. Third, the radar data was introduced as auxiliary information, under the additional constraint that its influence is determined by its agreement with the gauge data, which was measured by the correlation between gauges and co-located radar observations.

Results of the complete method showed to be superior to quantile-quantile transformation of the radar data as well as a pure copula interpolation, which can be interpreted as extreme limits of the complete method using the radar with maximum influence and not at all, respectively. While Kriging methods showed slightly better results in certain situations, the ability of the new method to estimate the uncertainty connected with the interpolation more accurately than any other approach may make it interesting for the generation of precipitation ensembles for hydrological uncertainty studies. Although the method provides stable results without the need for empirical adjustment factors (like the ones needed to stabilize the multiplicative version of conditional merging (c.f. Ehret (2003))), it is dependent on the proper convergence of several optimizations. Improving the estimation of the gauge marginal distribution, overcoming the representativeness issues due to the limited amount of gauges in the network, should greatly improve the estimates, as should accounting for anisotropies in the spatial structure. It would be interesting to investigate, if a way could be found to use the fast Fourier transform based variogram map estimations presented in Velasco-Forero et al. (2009), which automatically account for anisotropy, while honoring the assumption of precipitation being a censored variable.

Chapter 4 finally investigated the implications of having several, in parts largely different, estimates of precipitation for hydrological modeling. The analyses presented show that differences between interpolation type methods and methods including radar information only gradually disappear after aggregation over scales of 1000 km^2 and larger. Up to this scale, the radar information will lead to different results in discharge simulations. Above 1000 km^2, the use of radar data may not be necessary, if the gauge network is sufficiently dense. Given the significant differences between the precipitation estimates, it is likely that optimal parameter sets derived from these data will also be quite different, especially those which may be used to compensate some of the biases shown to exist between the different variants. Although the ideal case for hydrological comparison and verification of precipitation

inputs would be a model that does not rely on calibration, but is only improved by more detailed process knowledge and catchment information, setting up such a model would require significant effort and might not be feasible to do yet. If models that need to be calibrated are to be used, simultaneous calibration or, in extension of the ROPE concept presented by Bárdossy and Singh (2008), looking for parameter sets that would provide good results for several precipitation inputs, may also lead to insights on the different quality of precipitation estimates.

Bibliography

AghaKouchak, A., Bárdossy, A., and Habib, E.: Copula-based uncertainty modelling: application to multisensor precipitation estimates, Hydrological Processes, 24, 2111–2124, doi:10.1002/hyp.7632, 2010.

Aghakouchak, A., Habib, E., and Bárdossy, A.: A comparison of three remotely sensed rainfall ensemble generators, Atmospheric Research, 98, 387–399, doi:10.1016/j.atmosres.2010.07.016, 2010.

Allcroft, D. J. and Glasbey, C. A.: A latent Gaussian Markov random-field model for spatiotemporal rainfall disaggregation, Journal of the Royal Statistical Society: Series C (Applied Statistics), 52, 487–498, doi:10.1111/1467-9876.00419, 2003.

Atlas, D. and Banks, H. C.: The Interpretation of Microwave Reflections from Rainfall, Journal of Meteorology, 8, 271–282, doi:10.1175/1520-0469(1951)008⟨0271:TIOMRF⟩2.0.CO;2, 1951.

Atlas, D. and Battan, L. J.: Radar in meteorology: Battan memorial and 40th anniversary radar meteorology conference, American Meteorological Society, Boston, 1990.

Bárdossy, A.: Interpolation of groundwater quality parameters with some values below the detection limit, Hydrology and Earth System Sciences, 15, 2763–2775, doi:10.5194/hess-15-2763-2011, 2011.

Bárdossy, A. and Das, T.: Influence of rainfall observation network on model calibration and application, Hydrology and Earth System Sciences, 12, 77–89, doi:10.5194/hess-12-77-2008, 2008.

Bárdossy, A. and Li, J.: Geostatistical interpolation using copulas, Water Resources Research, 44, 1–15, doi:10.1029/2007WR006115, 2008.

Bárdossy, A. and Pegram, G. G.: Copula based multisite model for daily precipitation simulation, Hydrology and Earth System Sciences, 13, 2299–2314, 2009.

Bárdossy, A. and Singh, S. K.: Robust estimation of hydrological model parameters, Hydrology and Earth System Sciences, 12, 1273–1283, doi:10.5194/hess-12-1273-2008, 2008.

Bartels, H., Weigl, E., Reich, T., Lang, P., Wagner, A., Kohler, O., and Gerlach, N.: Projekt RADOLAN – Routineverfahren zur Online-Aneichung der Radarniederschlagsdaten mit Hilfe von automatischen Bodenniederschlagsstationen (Ombrometer), Tech. rep., 2004.

Battan, L. J.: Radar observation of the atmosphere, University of Chicago Press, Chicago, 1973.

Bech, J., Gjertsen, U., and Haase, G.: Modelling weather radar beam propagation and topographical blockage at northern high latitudes, Quarterly Journal of the Royal Meteorological Society, 133, 1191–1204, doi:10.1002/qj, 2007.

Berenguer, M., Sempere-Torres, D., Corral, C., and Sánchez-Diezma, R.: A Fuzzy Logic Technique for Identifying Nonprecipitating Echoes in Radar Scans, Journal of Atmospheric and Oceanic Technology, 23, 1157, doi:10.1175/JTECH1914.1, 2006.

Berenguer, M., Sempere-Torres, D., and Pegram, G. G.: SBMcast - An ensemble nowcasting technique to assess the uncertainty in rainfall forecasts by Lagrangian extrapolation, Journal of Hydrology, 404, 226–240, doi:10.1016/j.jhydrol.2011.04.033, 2011.

Berrocal, V. J., Raftery, A. E., and Gneiting, T.: Probabilistic quantitative precipitation field forecasting using a two-stage spatial model, The Annals of Applied Statistics, 2, 1170–1193, doi:10.1214/08-AOAS203, 2008.

Bouguet, J. and Others: Pyramidal implementation of the Lucas Kanade feature tracker - description of the algorithm, Intel Corporation, Microprocessor Research Labs, 1, 1–9, 2000.

Bowler, N. E., Pierce, C. E., and Seed, A. W.: Development of a precipitation nowcasting algorithm based upon optical flow techniques, Journal of Hydrology, 288, 74–91, 2004.

Bowler, N. E., Pierce, C. E., and Seed, A. W.: STEPS: A probabilistic precipitation forecasting scheme which merges an extrapolation nowcast with downscaled NWP, Quarterly Journal of the Royal Meteorological Society, 132, 2127–2155, doi:10.1256/qj.04.100, 2006.

Bradski, G. and Kaehler, A.: Learning OpenCV: Computer Vision with the OpenCV Library, O'Reilly Media, Sebastopol, 1 edn., 2008.

Brandes, E. A.: Optimizing Rainfall Estimates with the Aid of Radar, Journal of Applied Meteorology, 14, 1339–1345, doi:10.1175/1520-0450(1975)014⟨1339:OREWTA⟩2.0.CO;2, 1975.

Bringi, V. and Chandrasekar, V.: Polarimetric Doppler weather radar: Principles and applications, Cambridge Univ Pr, 2001.

Charles, S. P., Bates, B. C., and Hughes, J. P.: A spatiotemporal model for downscaling precipitation occurrence and amounts, Journal of Geophysical Research, 104, 31 657–31 669, doi:10.1029/1999JD900119, 1999.

Chen, S.: Probability density function estimation using gamma kernels, Annals of the Institute of Statistical Mathematics, 52, 471–480, 2000.

Chiles, J.-P. and Delfiner, P.: Geostatistics: modeling spatial uncertainty, John Wiley & Sons, New York, 1999.

Ciach, G. J.: Local Random Errors in Tipping-Bucket Rain Gauge Measurements, Journal of Atmospheric and Oceanic Technology, 20, 752–759, doi:10.1175/1520-0426(2003)20⟨752:LREITB⟩2.0.CO;2, 2003.

Clark, I.: Regularization of a semivariogram, Computers & Geosciences, 3, 341–346, 1977.

Cole, S. J. and Moore, R. J.: Hydrological modelling using raingauge- and radar-based estimators of areal rainfall, Journal of Hydrology, 358, 159–181, doi:10.1016/j.jhydrol.2008.05.025, 2008.

Collier, C. G.: Applications of weather radar systems: A guide to uses of radar data in meteorology and hydrology, John Wiley and Sons, New York, 2nd editio edn., 1996.

Cook, N. J.: Rebuttal of "Problems in the extreme value analysis", Structural Safety, 34, 418–423, doi:10.1016/j.strusafe.2011.08.002, 2012.

Cressie, N. and Hawkins, D. M.: Robust estimation of the variogram: I, Journal of the International Association for Mathematical Geology, 12, 115–125, doi:10.1007/BF01035243, 1980.

Delrieu, G., Creutin, J. D., and Andrieu, H.: Simulation of Radar Mountain Returns Using a Digitized Terrain Model, Journal of Atmospheric and Oceanic Technology, 12, 1038–1049, doi:10.1175/1520-0426(1995)012⟨1038:SORMRU⟩2.0.CO;2, 1995.

Delrieu, G., Caoudal, S., and Creutin, J. D.: Feasibility of Using Mountain Return for the Correction of Ground-Based X-Band Weather Radar Data, Journal of Atmospheric and Oceanic Technology, 14, 368, doi:10.1175/1520-0426(1997)014⟨0368:FOUMRF⟩2.0.CO;2, 1997.

Delrieu, G., Hucke, L., and Creutin, J. D.: Attenuation in Rain for X- and C-Band Weather Radar Systems: Sensitivity with respect to the Drop Size Distribution, Journal of Applied Meteorology, 38, 57–68, doi:10.1175/1520-0450(1999)038⟨0057:AIRFXA⟩2.0.CO;2, 1999a.

Delrieu, G., Serrar, S., Guardo, E., and Creutin, J. D.: Rain Measurement in Hilly Terrain with X-Band Weather Radar Systems: Accuracy of Path-Integrated Attenuation Estimates Derived from Mountain Returns, Journal of Atmospheric and Oceanic Technology, 16, 405–416, doi:10.1175/1520-0426(1999)016⟨0405:RMIHTW⟩2.0.CO;2, 1999b.

Delrieu, G., Andrieu, H., and Creutin, J. D.: Quantification of Path-Integrated Attenuation for X- and C-Band Weather Radar Systems Operating in Mediterranean Heavy Rainfall, Journal of Applied Meteorology, 39, 840–850, doi:10.1175/1520-0450(2000)039⟨0840:QOPIAF⟩2.0.CO;2, 2000.

Doviak, R. and Zrnić, D. S.: Doppler radar and weather observations, vol. 33, Academic Press, San Diego, 2 edn., 1993.

Duin, R.: On the Choice of Smoothing Parameters for Parzen Estimators of Probability Density Functions, IEEE Transactions on Computers, C-25, 1175–1179, doi:10.1109/TC.1976.1674577, 1976.

Ebert, E. E., Wilson, L. J., Brown, B. G., Nurmi, P., Brooks, H. E., Bally, J., and Jaeneke, M.: Verification of Nowcasts from the WWRP Sydney 2000 Forecast Demonstration Project, Weather and Forecasting, 19, 73–96, doi:10.1175/1520-0434(2004)019⟨0073:VONFTW⟩2.0.CO;2, 2004.

Ehret, U.: Rainfall and flood nowcasting in small catchments using weather radar, Dissertation, Universität Stuttgart, 2003.

Frei, C. and Schär, C.: A precipitation climatology of the Alps from high-resolution rain-gauge observations, International Journal of Climatology, 18, 873–900, doi:10.1002/(SICI)1097-0088(19980630)18:8⟨873::AID-JOC255⟩3.0.CO;2-9, 1998.

Gabella, M. and Notarpietro, R.: Ground clutter characterization and elimination in mountainous terrain, in: Proceedings of ERAD, pp. 305–311, Copernicus GmbH, Delft, 2002.

García-Pintado, J., Barberá, G. G., Erena, M., and Castillo, V. M.: Rainfall estimation by rain gauge-radar combination: A concurrent multiplicative-additive approach, Water Resources Research, 45, doi:10.1029/2008WR007011, 2009.

Genton, M.: Highly robust variogram estimation, Mathematical Geology, 30, 213–221, doi:10.1023/A:1021728614555, 1998.

Genz, A.: Numerical Computation of Multivariate Normal Probabilities, Journal of Computational and Graphical Statistics, 1, 141–149, doi:10.2307/1390838, 1992.

Germann, U., Galli, G., Boscacci, M., and Bolliger, M.: Radar precipitation measurement in a mountainous region, Quarterly Journal of the Royal Meteorological Society, 132, 1669–1692, doi:10.1256/qj.05.190, 2006.

Giuli, D., Gherardelli, M., Freni, A., Seliga, T. A., and Aydin, K.: Rainfall and Clutter Discrimination by Means of Dual-linear Polarization Radar Measurements, doi:10.1175/1520-0426(1991)008⟨0777:RACDBM⟩2.0.CO;2, 1991.

Goudenhoofdt, E. and Delobbe, L.: Evaluation of radar-gauge merging methods for quantitative precipitation estimates, Hydrology and Earth System Sciences, 13, 195–203, doi:10.5194/hess-13-195-2009, 2009.

Gourley, J. J. and Vieux, B. E.: A Method for Evaluating the Accuracy of Quantitative Precipitation Estimates from a Hydrologic Modeling Perspective, Journal of Hydrometeorology, 6, 115–133, doi:10.1175/JHM408.1, 2005.

Gourley, J. J., Tabary, P., and Parent du Chatelet, J.: A Fuzzy Logic Algorithm for the Separation of Precipitating from Nonprecipitating Echoes Using Polarimetric Radar Observations, Journal of Atmospheric and Oceanic Technology, 24, 1439, doi:10.1175/JTECH2035.1, 2007.

Grecu, M. and Krajewski, W. F.: An Efficient Methodology for Detection of Anomalous Propagation Echoes in Radar Reflectivity Data Using Neural Networks, Journal of Atmospheric and Oceanic Technology, 17, 121–129, doi:10.1175/1520-0426(2000)017⟨0121:AEMFDO⟩2.0.CO;2, 2000.

Haddad, B., Adane, A., Sauvageot, H., Sadouki, L., and Naili, R.: Identification and filtering of rainfall and ground radar echoes using textural features, International Journal of Remote Sensing, 25, 4641–4656, doi:10.1080/01431160310001654455, 2004.

Hassler, B., Helmert, K., and Seltmann, J.: Identification of spurious precipitation signals in radar data, Proc. ERAD2006, 2006.

Heistermann, M. and Kneis, D.: Benchmarking quantitative precipitation estimation by conceptual rainfall-runoff modeling, Water Resources Research, 47, doi:10.1029/2010WR009153, 2011.

Hildebrand, P. H.: Iterative Correction for Attenuation of 5 cm Radar in Rain, Journal of Applied Meteorology, 17, 508–514, doi:10.1175/1520-0450(1978)017⟨0508:ICFAOC⟩2.0.CO;2, 1978.

Hitschfeld, W.: The Invention of Radar Meterology, Bulletin of the American Meteorological Society, 67, 33–37, doi:10.1175/1520-0477(1986)067⟨0033:TIORM⟩2.0.CO;2, 1986.

Hitschfeld, W. and Bordan, J.: Errors Inherent in the Radar Measurement of Rainfall at Attenuating Wavelengths, Journal of the Atmospheric Sciences, 11, 58–67, doi:10.1175/1520-0469(1954)011⟨0058:EIITRM⟩2.0.CO;2, 1954.

Holleman, I.: Bias adjustment and long-term verification of radar-based precipitation estimates, Meteorological Applications, 14, 195–203, doi:10.1002/met.22, 2007.

Horn, B. K. and Schunck, B. G.: Determining optical flow, Artificial Intelligence, 17, 185–203, doi:10.1016/0004-3702(81)90024-2, 1981.

Hubbert, J. C., Dixon, M., Ellis, S., and Meymaris, G.: Weather Radar Ground Clutter. Part I: Identification, Modeling, and Simulation, Journal of Atmospheric and Oceanic Technology, 26, 1165, doi:10.1175/2009JTECHA1159.1, 2009.

IKSE: Dokumentation des Hochwassers vom August 2002 im Einzugsgebiet der Elbe, Tech. rep., International Commission for the Protection of the Elbe River, Magdeburg, 2004.

Isaaks, E. H. and Srivastava, R. M.: An Introduction to Applied Geostatistics, Oxford University Press, New York, New York, USA, 1990.

Jacobi, S., Heistermann, M., and Pfaff, T.: Evaluation and improvement of C-band radar attenuation correction for operational flash flood forecasting, in: Proceedings of the International Symposium Weather Radar and Hydrology, IAHS Publishing, Exeter, UK, 2011.

Jatho, N., Pluntke, T., Kurbjuhn, C., and Bernhofer, C.: An approach to combine radar and gauge based rainfall data under consideration of their qualities in low mountain ranges of Saxony, Natural Hazards and Earth System Science, 10, 429–446, 2010.

Journel, A. G. and Huijbregts, C. J.: Mining geostatistics, London [u.a.], Academic Press, 1978.

Kavetski, D. and Kuczera, G.: Model smoothing strategies to remove microscale discontinuities and spurious secondary optima in objective functions in hydrological calibration, Water Resources Research, 43, 9, doi:10.1029/2006WR005195, 2007.

Kavetski, D., Kuczera, G., and Franks, S. W.: Calibration of conceptual hydrological models revisited: 1. Overcoming numerical artefacts, Journal of Hydrology, 320, 173–186, doi:10.1016/j.jhydrol.2005.07.012, 2006.

Kessinger, C., Ellis, S., and Andel, J. V.: The radar echo classifier: A fuzzy logic algorithm for the WSR-88D, in: Proc. Third Conf. on Artificial Intelligence Applications to the Environmental Science, p. P1.6, American Meteorological Society, Long Beach, CA, USA, 1997.

Kitchen, M. and Blackall, R.: Representativeness errors in comparisons between radar and gauge measurements of rainfall, Journal of Hydrology, 134, 13–33, doi: 10.1016/0022-1694(92)90026-R, 1992.

Krajewski, W. F., Ntelekos, A. A., and Goska, R.: A GIS-based methodology for the assessment of weather radar beam blockage in mountainous regions: two examples from the US NEXRAD network, Computers & Geosciences, 32, 283–302, doi: 10.1016/j.cageo.2005.06.024, 2006.

Krämer, S.: Quantitative Radardatenaufbereitung für die Niederschalgsvorhersage und die Siedlungsentwässerung, Ph.D. thesis, Gottfried Wilhelm Leibniz Universität Hannover, 2008.

Krige, D. G.: A statistical approach to some basic mine valuation problems on the Witwatersrand, J. of the Chem., Metal. and Mining Soc. of South Africa, 52, 119–139, 1951.

Laux, P., Vogl, S., Qiu, W., Knoche, H. R., and Kunstmann, H.: Copula-based statistical refinement of precipitation in RCM simulations over complex terrain, Hydrology and Earth System Sciences, 15, 2401–2419, doi:10.5194/hess-15-2401-2011, 2011.

Lucas, B. D. and Kanade, T.: An Iterative Image Registration Technique with an Application to Stereo Vision, in: 7th International Joint Conference on Artificial Intelligence, edited by Hayes, P. J., pp. 674–679, William Kaufmann, 1981.

Makkonen, L.: Bringing Closure to the Plotting Position Controversy, Communications in Statistics - Theory and Methods, 37, 460–467, doi:10.1080/03610920701653094, 2008.

Marron, J. S.: Automatic smoothing parameter selection: A survey, Empirical Economics, 13, 187–208, doi:10.1007/BF01972448, 1988.

Marshall, J. S., Langille, R. C., and Palmer, W.: Measurement of Rainfall by Radar, Journal of Meteorology, 4, 186–192, doi:10.1175/1520-0469(1947)004⟨0186:MORBR⟩2.0.CO;2, 1947.

Marzoug, M. and Amayenc, P.: Improved range-profiling algorithm of rainfall rate from a spaceborne radar with path-integrated attenuation constraint, IEEE Transactions on Geoscience and Remote Sensing, 29, 584–592, doi:10.1109/36.135820, 1991.

Marzoug, M. and Amayenc, P.: A Class of Single-and Dual-Frequency Algorithms for Rain-Rate Profiling from a Spaceborne Radar. Pad I: Principle and Tests from Numerical Simulations, Journal of Atmospheric and Oceanic Technology, 11, 1480–1506, doi:10.1175/1520-0426(1994)011⟨1480:ACOSAD⟩2.0.CO;2, 1994.

Matheron, G.: The theory of regionalized variables and its applications, École national supérieure des mines, Paris, 1971.

May, P. T., Keenan, T. D., Potts, R., Wilson, J. W., Webb, R., Treloar, A., Spark, E., Lawrence, S., Ebert, E. E., Bally, J., and Joe, P.: The Sydney 2000 Olympic Games Forecast Demonstration Project: Forecasting, Observing Network Infrastructure, and Data Processing Issues, Weather and Forecasting, 19, 115–130, doi:10.1175/1520-0434(2004)019⟨0115:TSOGFD⟩2.0.CO;2, 2004.

Meneghini, R., Eckerman, J., and Atlas, D.: Determination of Rain Rate from a Spaceborne Radar Using Measurements of Total Attenuation, IEEE Transactions on Geoscience and Remote Sensing, GE-21, 34–43, doi:10.1109/TGRS.1983.350528, 1983.

Michelson, D. and Koistinen, J.: Gauge-Radar network adjustment for the baltic sea experiment, Physics and Chemistry of the Earth, Part B: Hydrology, Oceans and Atmosphere, 25, 915–920, doi:10.1016/S1464-1909(00)00125-8, 2000.

Mie, G.: Beiträge zur Optik trüber Medien, speziell kolloidaler Metallösungen, Annalen der Physik, 330, 377–445, doi:10.1002/andp.19083300302, 1908.

Mosthaf, T.: Investigation on the influence of different methods to determine areal precipitation on flood forecasting, Diploma thesis, University of Stuttgart, 2012.

Nguyen, C. M., Moisseev, D. N., and Chandrasekar, V.: A Parametric Time Domain Method for Spectral Moment Estimation and Clutter Mitigation for Weather Radars, Journal of Atmospheric and Oceanic Technology, 25, 83–92, doi:10.1175/2007JTECHA927.1, 2008.

Nicol, J. C. and Austin, G. L.: Attenuation correction constraint for single-polarisation weather radar, Meteorological Applications, 10, 345–354, doi:10.1017/S1350482703001051, 2003.

Pardo-Igúzquiza, E., Chica-Olmo, M., and Atkinson, P. M.: Downscaling cokriging for image sharpening, Remote Sensing of Environment, 102, 86–98, doi:10.1016/j.rse.2006.02.014, 2006.

Parzen, E.: On Estimation of a Probability Density Function and Mode, The Annals of Mathematical Statistics, 33, 1065–1076, doi:10.1214/aoms/1177704472, 1962.

Pierce, C. E., Ebert, E. E., Seed, A. W., Sleigh, M., Collier, C. G., Fox, N. I., Donaldson, N., Wilson, J. W., Roberts, R. D., and Mueller, C. K.: The Nowcasting of Precipitation during Sydney 2000: An Appraisal of the QPF Algorithms, Weather and Forecasting, 19, 7–21, doi:10.1175/1520-0434(2004)019⟨0007:TNOPDS⟩2.0.CO;2, 2004.

Rinehart, R. E. and Garvey, E. T.: Three-dimensional storm motion detection by conventional weather radar, Nature, 273, 287–289, doi:10.1038/273287a0, 1978.

Rosenblatt, M.: Remarks on Some Nonparametric Estimates of a Density Function, The Annals of Mathematical Statistics, 27, 832–837, doi:10.1214/aoms/1177728190, 1956.

Rosenfeld, D., Wolff, D. B., and Atlas, D.: General Probability-matched Relations between Radar Reflectivity and Rain Rate, Journal of Applied Meteorology, 32, 50, doi:10.1175/1520-0450(1993)032⟨0050:GPMRBR⟩2.0.CO;2, 1993.

Rosenfeld, D., Wolff, D. B., and Amitai, E.: The Window Probability Matching Method for Rainfall Measurements with Radar, Journal of Applied Meteorology, 33, 682–693, doi:10.1175/1520-0450(1994)033⟨0682:TWPMMF⟩2.0.CO;2, 1994.

Ruiz-Villanueva, V., Borga, M., Zoccatelli, D., Marchi, L., Gaume, E., and Ehret, U.: Extreme flood response to short-duration convective rainfall in South-West Germany, Hydrology and Earth System Sciences, 16, 1543–1559, doi:10.5194/hess-16-1543-2012, 2012.

Sansó, B. and Guenni, L.: A Nonstationary Multisite Model for Rainfall, Journal of the American Statistical Association, 95, 1089–1100, doi:10.1080/01621459.2000.10474305, 2000.

Saxen, T. R., Mueller, C. K., Warner, T. T., Steiner, M., Ellison, E. E., Hatfield, E. W., Betancourt, T. L., Dettling, S. M., and Oien, N. A.: The Operational Mesogamma-Scale Analysis and Forecast System of the U.S. Army Test and Evaluation Command. Part IV: The White Sands Missile Range Auto-Nowcast System, Journal of Applied Meteorology and Climatology, 47, 1123–1139, doi:10.1175/2007JAMC1656.1, 2008.

Schiemann, R., Erdin, R., Willi, M., Frei, C., Berenguer, M., and Sempere-Torres, D.: Geostatistical radar-raingauge combination with nonparametric correlograms: methodological considerations and application in Switzerland, Hydrology and Earth System Sciences, 15, 1515–1536, doi:10.5194/hess-15-1515-2011, 2011.

Schoelzel, C. and Friederichs, P.: Multivariate non-normally distributed random variables in climate research–introduction to the copula approach, Nonlinear Processes in Geophysics, pp. 761–772, 2008.

Seed, A. W., Nicol, J. C., Austin, G. L., Stow, C. D., and Bradley, S. G.: The impact of radar and raingauge sampling errors when calibrating a weather radar, Meteorological Applications, 3, 43–52, doi:10.1002/met.5060030105, 2007.

Seltmann, J.: Radarforschung im DWD - vom SCAN zum Produkt, Promet, pp. 32–42, 1997.

Seo, D.-J. and Breidenbach, J.: Real-Time Correction of Spatially Nonuniform Bias in Radar Rainfall Data Using Rain Gauge Measurements, Journal of Hydrometeorology, 3, 93, doi:10.1175/1525-7541(2002)003⟨0093:RTCOSN⟩2.0.CO;2, 2002.

Shepard, D.: A two-dimensional interpolation function for irregularly-spaced data, in: Proceedings of the 1968 23rd ACM national conference on -, pp. 517–524, ACM Press, New York, New York, USA, doi:10.1145/800186.810616, 1968.

Siggia, A. D. and Passarelli, R. E.: Gaussian model adaptive processing (GMAP) for improved ground clutter cancellation and moment calculation, in: Proc. Third European Conf. on Radar in Meteorology and Hydrology, pp. 67–73, ERAD, Visby, Gotland, Sweden, 2004.

Sinclair, S.: Spatio-temporal rainfall estimation and Nowcasting for Flash Flood Forecasting, Phd thesis, University of KwaZulu-Natal, Durban, South Africa, 2007.

Skolnik, M. I.: Radar handbook, McGraw-Hill, New York, 2nd edn., 1990.

Steiner, M. and Smith, J. a.: Use of Three-Dimensional Reflectivity Structure for Automated Detection and Removal of Nonprecipitating Echoes in Radar Data, Journal of Atmospheric and Oceanic Technology, 19, 673–686, doi:10.1175/1520-0426(2002)019⟨0673:UOTDRS⟩2.0.CO;2, 2002.

Todini, E.: A Bayesian technique for conditioning radar precipitation estimates to rain-gauge measurements, Hydrology and Earth System Sciences, 5, 187–199, doi:10.5194/hess-5-187-2001, 2001.

Torres, S. M. and Zrnić, D. S.: Ground Clutter Canceling with a Regression Filter, Journal of Atmospheric and Oceanic Technology, 16, 1364–1372, doi:10.1175/1520-0426(1999)016⟨1364:GCCWAR⟩2.0.CO;2, 1999.

Trier, S. B., Davis, C. A., and Tuttle, J.: Long-Lived Mesoconvective Vortices and Their Environment. Part I: Observations from the Central United States during the 1998 Warm Season, Monthly Weather Review, 128, 3376–3395, doi:10.1175/1520-0493(2000)128⟨3376:LLMVAT⟩2.0.CO;2, 2000.

Turner, B. and Zawadzki, I.: Predictability of precipitation from continental radar images. Part III: Operational nowcasting implementation (MAPLE), Journal of Applied Meteorology, pp. 231–248, 2010.

Tuttle, J. and Gall, R.: A Single-Radar Technique for Estimating the Winds in Tropical Cyclones, Bulletin of the American Meteorological Society, 80, 653–668, doi:10.1175/1520-0477(1999)080⟨0653:ASRTFE⟩2.0.CO;2, 1999.

van den Berg, M. J., Vandenberghe, S., De Baets, B., and Verhoest, N. E. C.: Copula-based downscaling of spatial rainfall: a proof of concept, Hydrology and Earth System Sciences, 15, 1445–1457, doi:10.5194/hess-15-1445-2011, 2011.

Vandenberghe, S., Verhoest, N. E. C., Buyse, E., and De Baets, B.: A stochastic design rainfall generator based on copulas and mass curves, Hydrology and Earth System Sciences, 14, 2429–2442, doi:10.5194/hess-14-2429-2010, 2010.

Velasco-Forero, C. A., Sempere-Torres, D., Cassiraga, E. F., and Jaime Gómez-Hernández, J.: A non-parametric automatic blending methodology to estimate rainfall fields from rain gauge and radar data, Advances in Water Resources, 32, 986–1002, doi:10.1016/j.advwatres.2008.10.004, 2009.

Vieux, B. E. and Bedient, P. B.: Assessing urban hydrologic prediction accuracy through event reconstruction, Journal of Hydrology, 299, 217–236, doi:10.1016/j.jhydrol.2004.08.005, 2004.

Wackernagel, H.: Multivariate Geostatistics, Springer, 3 edn., 2003.

Whiton, R. C., Smith, P. L., Bigler, S. G., Wilk, K. E., and Harbuck, A. C.: History of Operational Use of Weather Radar by U.S. Weather Services. Part I: The Pre-NEXRAD Era, Weather and Forecasting, 13, 219–243, doi:10.1175/1520-0434(1998)013⟨0219:HOOUOW⟩2.0.CO;2, 1998.

Wilks, D. S. and Wilby, R. L.: The weather generation game: a review of stochastic weather models, Progress in Physical Geography, 23, 329–357, doi:10.1177/030913339902300302, 1999.

Wilson, J. W. and Brandes, E. A.: Radar Measurement of Rainfall–A Summary, Bulletin of the American Meteorological Society, 60, 1048–1060, doi:10.1175/1520-0477(1979)060⟨1048:RMORS⟩2.0.CO;2, 1979.

Wu, L., Seo, D.-J., Demargne, J., Brown, J. D., Cong, S., and Schaake, J.: Generation of ensemble precipitation forecast from single-valued quantitative precipitation forecast for hydrologic ensemble prediction, Journal of Hydrology, 399, 281–298, doi:10.1016/j.jhydrol.2011.01.013, 2011.

Yilmaz, K. K., Hogue, T. S., Hsu, K.-l., Sorooshian, S., Gupta, H. V., and Wagener, T.: Intercomparison of Rain Gauge, Radar, and Satellite-Based Precipitation Estimates with Emphasis on Hydrologic Forecasting, Journal of Hydrometeorology, 6, 497–517, doi:10.1175/JHM431.1, 2005.

Zoccatelli, D., Borga, M., Viglione, A., Chirico, G. B., and Blöschl, G.: Spatial moments of catchment rainfall: rainfall spatial organisation, basin morphology, and flood response, Hydrology and Earth System Sciences, 15, 3767–3783, doi:10.5194/hess-15-3767-2011, 2011.

Zrnić, D. S. and Melnikov, V.: Ground clutter recognition using polarimetric spectral parameters, in: 33rd Conf. on Radar Meteorology, 4, p. P11B.13, American Meteorological Society, Cairns, Australia, 2007.

Appendix

A. Parameter Sensitivity of Advection Estimation Methods

This appendix section gives the results of the analysis on the sensitivity of the three optical flow estimation methods presented in section 2.4 on their main parameters.

Sensitivity was assessed by boxplots of RMSE and MAE calculated from the difference between images advected by one timestep of 5 minutes using the estimated advection field, with the actual radar measurement made at this time.

In total 12 images from the time period 2008-06-23 01:50 – 2008-06-23 02:45 UTC for an excerpt from the German radar composite over the radar Dresden were used.

A.1. Block Matching Method

Figs. A.1 and A.2 show the results for MAE and RMSE for the block matching approach.

Increasing the block size (bs) improves the estimates as well as increasing the maximum search range (mr) from 5 to 10 pixels, implying that the majority of displacements are between 5 and 10 km per 5 minutes. An increased resolution of the estimated advection field, obtained by reducing the shift size (ss) only leads to a very small improvement of the performance of the algorithm.

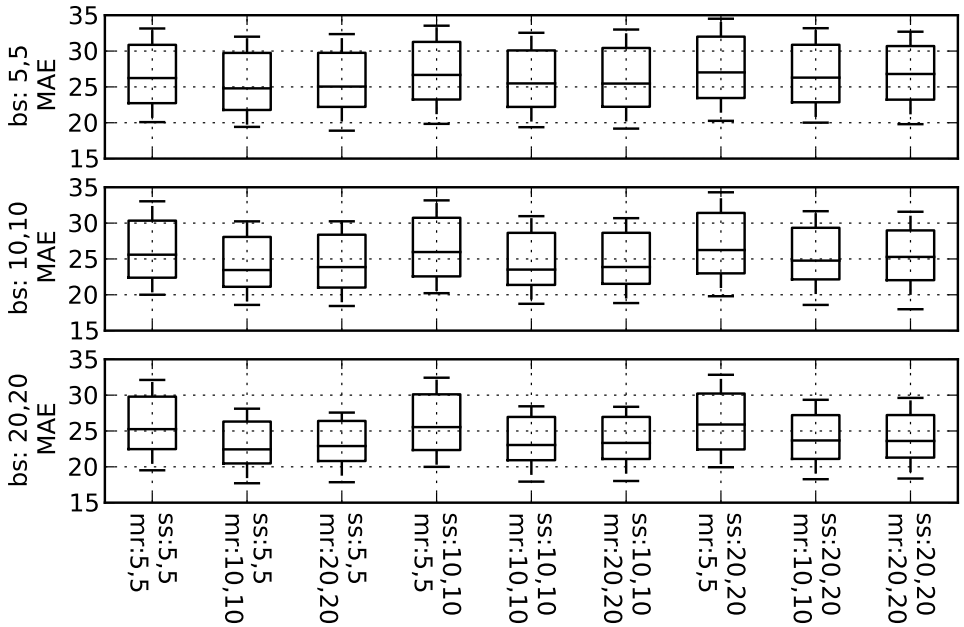

Figure A.1.: Boxplots of mean absolute error for Block Matching method. Parameters: bs - block size, ss - shift size, mr - maximum range. See section 2.4 for detailed explanation

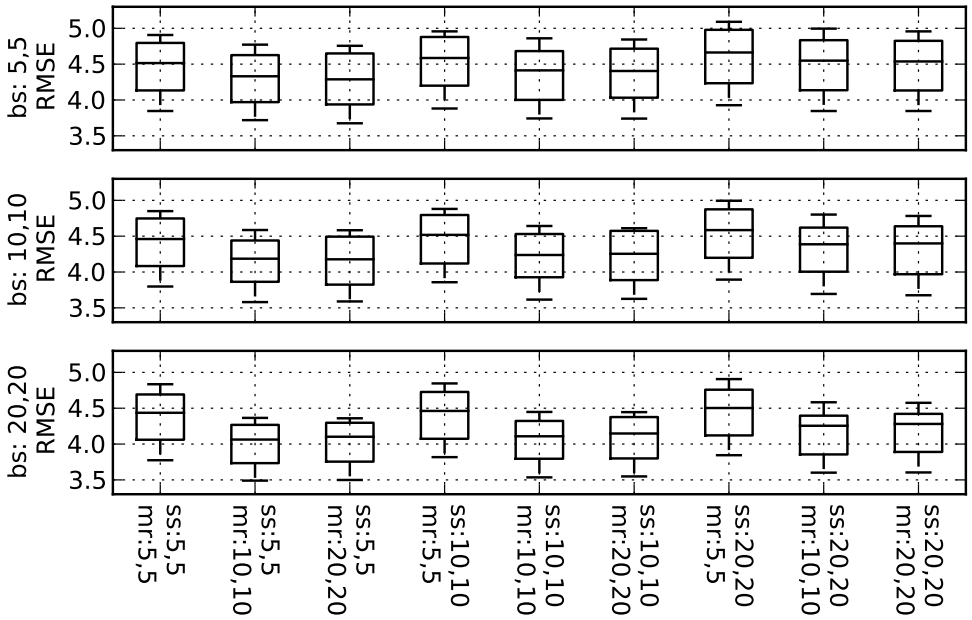

Figure A.2.: Boxplots of root mean squared error for Block Matching method. Parameters: bs - block size, ss - shift size, mr - maximum range

A.2. Horn and Schunck Method

From the boxplots in fig. A.3 the following dependencies of algorithm performance on the three investigated parameters may be observed:

For the smallest values of λ, the best results may be obtained by a slight smoothing of the input data.

Increasing the maximum number of iterations (mi) increases the error when not doing any smoothing, but reduces the spread of the distribution of errors for the optimal smoothing window of 7x7 pixels. As λ increases the beneficial effect of smoothing disappears with best results obtained for no smoothing at λ=10.

For higher lambda, increasing the number of iterations produces more images with less error for larger smoothing windows. It should be noted, that in the original publication, however, convergence of the field had been achieved for 32 to 64 iterations. Whether this may be an issue of the actual implementation of the algorithm, or caused by the data, would have to be investigated further.

The RMSE measure presented in fig. A.4 shows the increase in error due to smoothing and the somehow mitigating effect of a larger number of iterations for larger values of λ more pronounced. According to these plots, however, smoothing would always decrease the performance of the algorithm.

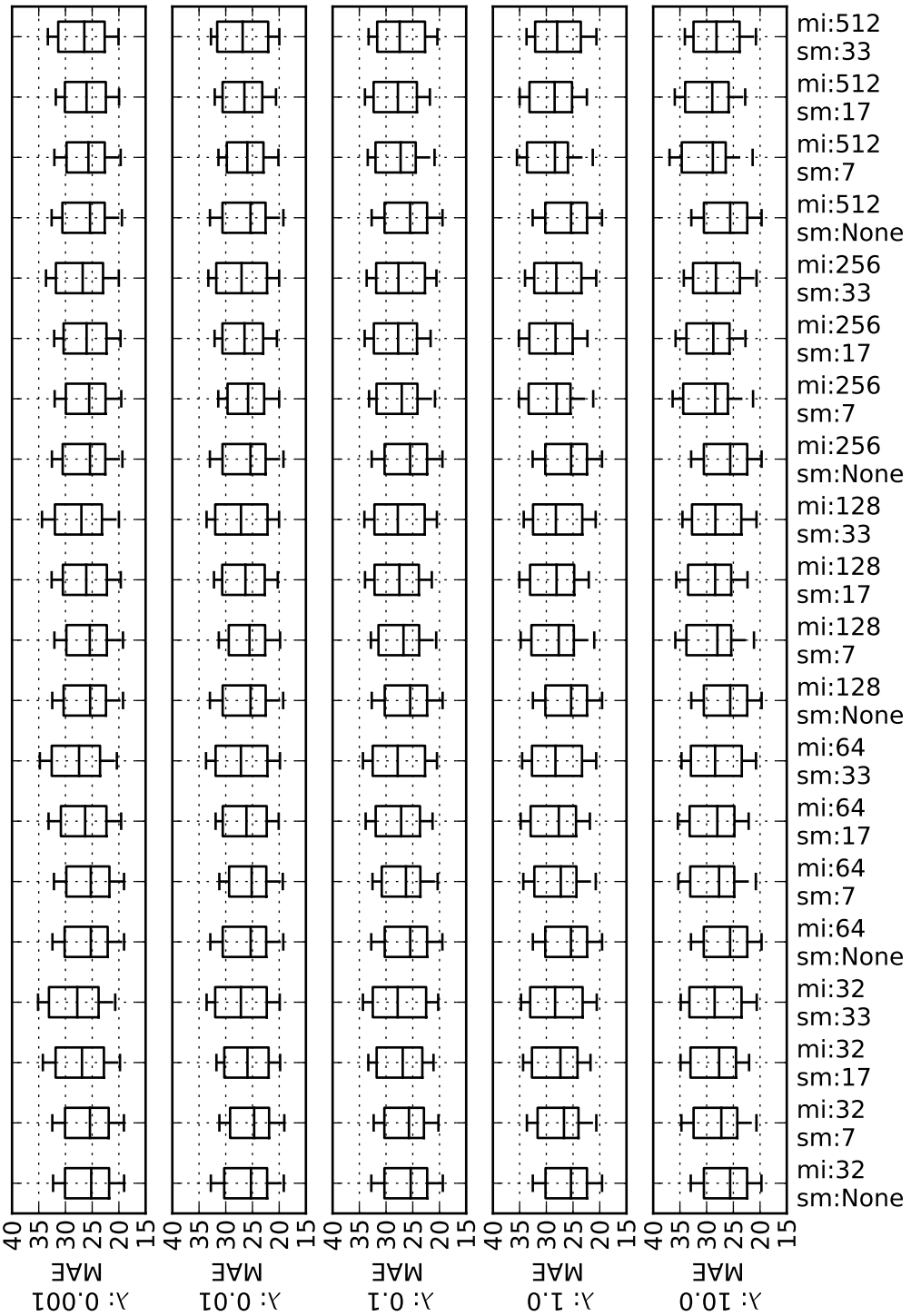

Figure A.3.: Boxplots of mean absolute error for Horn & Schunck method. Parameters: λ - smoothness weight, mi - maximum no. of iterations, sm - size of smoothing window

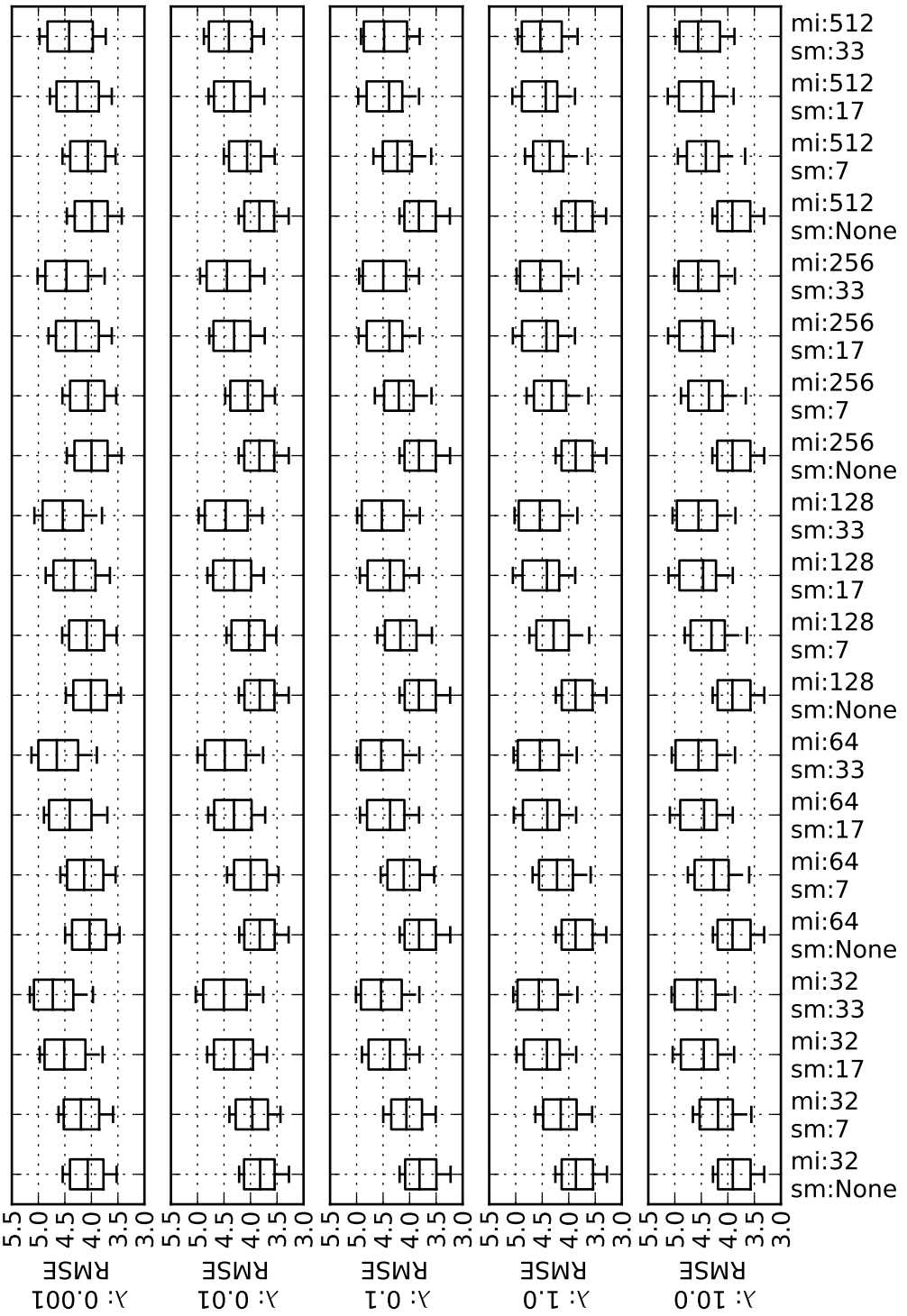

Figure A.4.: Boxplots of root mean squared error for Horn & Schunck method. Parameters: λ - smoothness weight, mi - maximum no. of iterations, sm - size of smoothing window

A.3. Lucas and Kanade Method with Pyramids

In figs. A.5 and A.6 no variation between parameter sets can be observed. Parameters had been chosen such that decisions on possible compromises regarding resolution of the estimated advection field or runtime performance could be made. However, none of these choices changed the behavior of the algorithm. Given that the performance for all parameter sets is better than those of the other algorithms, a search for the parameter region, which might produce even better estimates, possibly at the cost of higher instability, was not attempted.

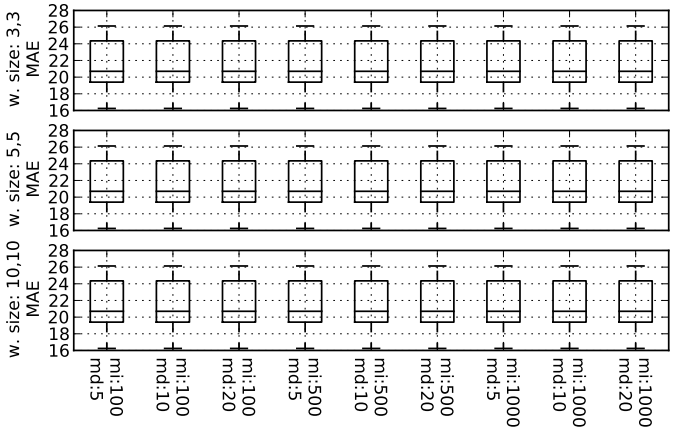

Figure A.5.: Boxplots of mean absolute error for Lucas & Kanade with pyramids method. Parameters: w. size - window size for pyramid generation, mi - maximum no. of iterations, md - minimum separation distance of analyzed points

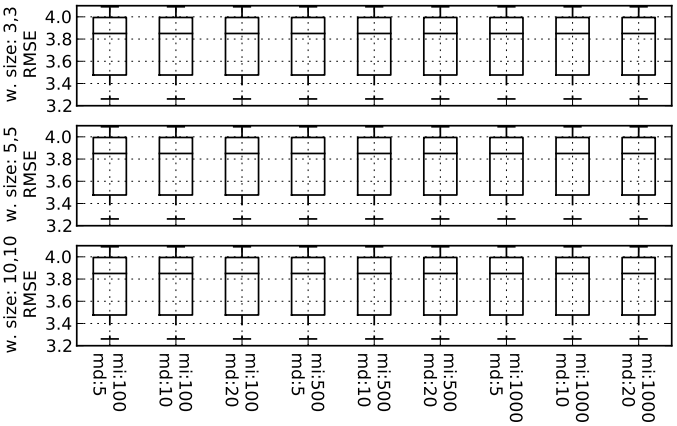

Figure A.6.: Boxplots of root mean squared error for Lucas & Kanade with pyramids method.
Parameters: w. size - window size for pyramid generation, mi - maximum no. of iterations, md - minimum separation distance of analyzed points

Curriculum Vitae

12. November 1976	born in Würzburg, Germany
1987 - 1996	Hanns-Seidel Gymnasium Hösbach, Germany Abitur
1997 - 1999	University of Heidelberg, Germany Vordiplom in Physics
1999 - 2004	University of Stuttgart, Germany, Dipl.-Ing. in Environmental Engineering
2001 - 2003	University of Tokyo, Japan, Master of Engineering (M.Eng.) in Civil Engineering Thesis on "Estimation of Snowfall and Cloud Liquid Water Content Using Ground Based Passive Microwave Radiometry"
2004 - 2006	Employee at Dr.-Ing. Karl Ludwig, Wasserwirtschaft, Wasserbau, Consulting Engineer, Karlsruhe, Germany
since 2006	Research Assistant at the Institute for Modelling Hydraulic and Environmental Systems, University of Stuttgart, Germany

Institut für Wasser- und Umweltsystemmodellierung
Universität Stuttgart

Pfaffenwaldring 61
70569 Stuttgart (Vaihingen)
Telefon (0711) 685 - 64717/64749/64752/64679
Telefax (0711) 685 - 67020 o. 64746 o. 64681
E-Mail: iws@iws.uni-stuttgart.de
http://www.iws.uni-stuttgart.de

Verzeichnis der Mitteilungshefte

5 Plate, Erich: *Beitrag zur Bestimmung der Windgeschwindigkeitsverteilung in der durch eine Wand gestörten bodennahen Luftschicht*,
und
Röhnisch, Arthur; Marotz, Günter: *Neue Baustoffe und Bauausführungen für den Schutz der Böschungen und der Sohle von Kanälen, Flüssen und Häfen; Gestehungskosten und jeweilige Vorteile*, sowie Unny, T.E.: *Schwingungsuntersuchungen am Kegelstrahlschieber*, 1967

6 Seiler, Erich: *Die Ermittlung des Anlagenwertes der bundeseigenen Binnenschiffahrtsstraßen und Talsperren und des Anteils der Binnenschiffahrt an diesem Wert*, 1967

7 *Sonderheft anläßlich des 65. Geburtstages von Prof. Arthur Röhnisch mit Beiträgen von* Benk, Dieter; Breitling, J.; Gurr, Siegfried; Haberhauer, Robert; Honekamp, Hermann; Kuz, Klaus Dieter; Marotz, Günter; Mayer-Vorfelder, Hans-Jörg; Miller, Rudolf; Plate, Erich J.; Radomski, Helge; Schwarz, Helmut; Vollmer, Ernst; Wildenhahn, Eberhard; 1967

8 Jumikis, Alfred: *Beitrag zur experimentellen Untersuchung des Wassernachschubs in einem gefrierenden Boden und die Beurteilung der Ergebnisse*, 1968

9 Marotz, Günter: *Technische Grundlagen einer Wasserspeicherung im natürlichen Untergrund*, 1968

10 Radomski, Helge: *Untersuchungen über den Einfluß der Querschnittsform wellenförmiger Spundwände auf die statischen und rammtechnischen Eigenschaften*, 1968

11 Schwarz, Helmut: *Die Grenztragfähigkeit des Baugrundes bei Einwirkung vertikal gezogener Ankerplatten als zweidimensionales Bruchproblem*, 1969

12 Erbel, Klaus: *Ein Beitrag zur Untersuchung der Metamorphose von Mittelgebirgsschneedecken unter besonderer Berücksichtigung eines Verfahrens zur Bestimmung der thermischen Schneequalität*, 1969

13 Westhaus, Karl-Heinz: *Der Strukturwandel in der Binnenschiffahrt und sein Einfluß auf den Ausbau der Binnenschiffskanäle*, 1969

14 Mayer-Vorfelder, Hans-Jörg: *Ein Beitrag zur Berechnung des Erdwiderstandes unter Ansatz der logarithmischen Spirale als Gleitflächenfunktion*, 1970

15 Schulz, Manfred: *Berechnung des räumlichen Erddruckes auf die Wandung kreiszylindrischer Körper*, 1970

16 Mobasseri, Manoutschehr: *Die Rippenstützmauer. Konstruktion und Grenzen ihrer Standsicherheit*, 1970

17 Benk, Dieter: *Ein Beitrag zum Betrieb und zur Bemessung von Hochwasserrückhaltebecken*, 1970

18 Gàl, Attila: *Bestimmung der mitschwingenden Wassermasse bei überströmten Fischbauchklappen mit kreiszylindrischem Staublech*, 1971, vergriffen

19 Kuz, Klaus Dieter: *Ein Beitrag zur Frage des Einsetzens von Kavitationserscheinungen in einer Düsenströmung bei Berücksichtigung der im Wasser gelösten Gase*, 1971, vergriffen

20 Schaak, Hartmut: *Verteilleitungen von Wasserkraftanlagen*, 1971

21 *Sonderheft zur Eröffnung der neuen Versuchsanstalt des Instituts für Wasserbau der Universität Stuttgart mit Beiträgen von* Brombach, Hansjörg; Dirksen, Wolfram; Gàl, Attila; Gerlach, Reinhard; Giesecke, Jürgen; Holthoff, Franz-Josef; Kuz, Klaus Dieter; Marotz, Günter; Minor, Hans-Erwin; Petrikat, Kurt; Röhnisch, Arthur; Rueff, Helge; Schwarz, Helmut; Vollmer, Ernst; Wildenhahn, Eberhard; 1972

22 Wang, Chung-su: *Ein Beitrag zur Berechnung der Schwingungen an Kegelstrahlschiebern*, 1972

23 Mayer-Vorfelder, Hans-Jörg: *Erdwiderstandsbeiwerte nach dem Ohde-Variationsverfahren*, 1972

24 Minor, Hans-Erwin: *Beitrag zur Bestimmung der Schwingungsanfachungsfunktionen überströmter Stauklappen*, 1972, vergriffen

25 Brombach, Hansjörg: *Untersuchung strömungsmechanischer Elemente (Fluidik) und die Möglichkeit der Anwendung von Wirbelkammerelementen im Wasserbau*, 1972, vergriffen

26 Wildenhahn, Eberhard: *Beitrag zur Berechnung von Horizontalfilterbrunnen*, 1972

27 Steinlein, Helmut: *Die Eliminierung der Schwebstoffe aus Flußwasser zum Zweck der unterirdischen Wasserspeicherung, gezeigt am Beispiel der Iller*, 1972

28 Holthoff, Franz Josef: *Die Überwindung großer Hubhöhen in der Binnenschiffahrt durch Schwimmerhebewerke*, 1973

29 Röder, Karl: *Einwirkungen aus Baugrundbewegungen auf trog- und kastenförmige Konstruktionen des Wasser- und Tunnelbaues*, 1973

30 Kretschmer, Heinz: *Die Bemessung von Bogenstaumauern in Abhängigkeit von der Talform*, 1973

31 Honekamp, Hermann: *Beitrag zur Berechnung der Montage von Unterwasserpipelines*, 1973

32 Giesecke, Jürgen: *Die Wirbelkammertriode als neuartiges Steuerorgan im Wasserbau*, und Brombach, Hansjörg: *Entwicklung, Bauformen, Wirkungsweise und Steuereigenschaften von Wirbelkammerverstärkern*, 1974

33 Rueff, Helge: *Untersuchung der schwingungserregenden Kräfte an zwei hintereinander angeordneten Tiefschützen unter besonderer Berücksichtigung von Kavitation*, 1974

34 Röhnisch, Arthur: *Einpreßversuche mit Zementmörtel für Spannbeton - Vergleich der Ergebnisse von Modellversuchen mit Ausführungen in Hüllwellrohren*, 1975

35 *Sonderheft anläßlich des 65. Geburtstages von Prof. Dr.-Ing. Kurt Petrikat mit Beiträgen von*: Brombach, Hansjörg; Erbel, Klaus; Flinspach, Dieter; Fischer jr., Richard; Gàl, Attila; Gerlach, Reinhard; Giesecke, Jürgen; Haberhauer, Robert; Hafner Edzard; Hausenblas, Bernhard; Horlacher, Hans-Burkhard; Hutarew, Andreas; Knoll, Manfred; Krummet, Ralph; Marotz, Günter; Merkle, Theodor; Miller, Christoph; Minor, Hans-Erwin; Neumayer, Hans; Rao, Syamala; Rath, Paul; Rueff, Helge; Ruppert, Jürgen; Schwarz, Wolfgang; Topal-Gökceli, Mehmet; Vollmer, Ernst; Wang, Chung-su; Weber, Hans-Georg; 1975

36 Berger, Jochum: *Beitrag zur Berechnung des Spannungszustandes in rotationssymmetrisch belasteten Kugelschalen veränderlicher Wandstärke unter Gas- und Flüssigkeitsdruck durch Integration schwach singulärer Differentialgleichungen*, 1975

37 Dirksen, Wolfram: *Berechnung instationärer Abflußvorgänge in gestauten Gerinnen mittels Differenzenverfahren und die Anwendung auf Hochwasserrückhaltebecken*, 1976

38 Horlacher, Hans-Burkhard: *Berechnung instationärer Temperatur- und Wärmespannungsfelder in langen mehrschichtigen Hohlzylindern*, 1976

39 Hafner, Edzard: *Untersuchung der hydrodynamischen Kräfte auf Baukörper im Tiefwasserbereich des Meeres*, 1977, ISBN 3-921694-39-6

40 Ruppert, Jürgen: *Über den Axialwirbelkammerverstärker für den Einsatz im Wasserbau*, 1977, ISBN 3-921694-40-X

41 Hutarew, Andreas: *Beitrag zur Beeinflußbarkeit des Sauerstoffgehalts in Fließgewässern an Abstürzen und Wehren*, 1977, ISBN 3-921694-41-8, vergriffen

42 Miller, Christoph: *Ein Beitrag zur Bestimmung der schwingungserregenden Kräfte an unterströmten Wehren*, 1977, ISBN 3-921694-42-6

43 Schwarz, Wolfgang: *Druckstoßberechnung unter Berücksichtigung der Radial- und Längsverschiebungen der Rohrwandung*, 1978, ISBN 3-921694-43-4

44 Kinzelbach, Wolfgang: *Numerische Untersuchungen über den optimalen Einsatz variabler Kühlsysteme einer Kraftwerkskette am Beispiel Oberrhein*, 1978, ISBN 3-921694-44-2

45 Barczewski, Baldur: *Neue Meßmethoden für Wasser-Luftgemische und deren Anwendung auf zweiphasige Auftriebsstrahlen*, 1979, ISBN 3-921694-45-0

46 Neumayer, Hans: *Untersuchung der Strömungsvorgänge in radialen Wirbelkammerverstärkern*, 1979, ISBN 3-921694-46-9

47 Elalfy, Youssef-Elhassan: *Untersuchung der Strömungsvorgänge in Wirbelkammerdioden und -drosseln*, 1979, ISBN 3-921694-47-7

48 Brombach, Hansjörg: *Automatisierung der Bewirtschaftung von Wasserspeichern*, 1981, ISBN 3-921694-48-5

49 Geldner, Peter: *Deterministische und stochastische Methoden zur Bestimmung der Selbstdichtung von Gewässern*, 1981, ISBN 3-921694-49-3, vergriffen

50 Mehlhorn, Hans: *Temperaturveränderungen im Grundwasser durch Brauchwassereinleitungen*, 1982, ISBN 3-921694-50-7, vergriffen

51 Hafner, Edzard: *Rohrleitungen und Behälter im Meer*, 1983, ISBN 3-921694-51-5

52 Rinnert, Bernd: *Hydrodynamische Dispersion in porösen Medien: Einfluß von Dichteunterschieden auf die Vertikalvermischung in horizontaler Strömung*, 1983, ISBN 3-921694-52-3, vergriffen

53 Lindner, Wulf: *Steuerung von Grundwasserentnahmen unter Einhaltung ökologischer Kriterien*, 1983, ISBN 3-921694-53-1, vergriffen

54 Herr, Michael; Herzer, Jörg; Kinzelbach, Wolfgang; Kobus, Helmut; Rinnert, Bernd: *Methoden zur rechnerischen Erfassung und hydraulischen Sanierung von Grundwasserkontaminationen*, 1983, ISBN 3-921694-54-X

55 Schmitt, Paul: *Wege zur Automatisierung der Niederschlagsermittlung*, 1984, ISBN 3-921694-55-8, vergriffen

56 Müller, Peter: *Transport und selektive Sedimentation von Schwebstoffen bei gestautem Abfluß*, 1985, ISBN 3-921694-56-6

57 El-Qawasmeh, Fuad: *Möglichkeiten und Grenzen der Tropfbewässerung unter besonderer Berücksichtigung der Verstopfungsanfälligkeit der Tropfelemente*, 1985, ISBN 3-921694-57-4, vergriffen

58 Kirchenbaur, Klaus: *Mikroprozessorgesteuerte Erfassung instationärer Druckfelder am Beispiel seegangsbelasteter Baukörper*, 1985, ISBN 3-921694-58-2

59 Kobus, Helmut (Hrsg.): *Modellierung des großräumigen Wärme- und Schadstofftransports im Grundwasser*, Tätigkeitsbericht 1984/85 (DFG-Forschergruppe an den Universitäten Hohenheim, Karlsruhe und Stuttgart), 1985, ISBN 3-921694-59-0, vergriffen

60 Spitz, Karlheinz: *Dispersion in porösen Medien: Einfluß von Inhomogenitäten und Dichteunterschieden*, 1985, ISBN 3-921694-60-4, vergriffen

61 Kobus, Helmut: *An Introduction to Air-Water Flows in Hydraulics*, 1985, ISBN 3-921694-61-2

62 Kaleris, Vassilios: *Erfassung des Austausches von Oberflächen- und Grundwasser in horizontalebenen Grundwassermodellen*, 1986, ISBN 3-921694-62-0

63 Herr, Michael: *Grundlagen der hydraulischen Sanierung verunreinigter Porengrundwasserleiter*, 1987, ISBN 3-921694-63-9

64 Marx, Walter: *Berechnung von Temperatur und Spannung in Massenbeton infolge Hydratation*, 1987, ISBN 3-921694-64-7

65 Koschitzky, Hans-Peter: *Dimensionierungskonzept für Sohlbelüfter in Schußrinnen zur Vermeidung von Kavitationsschäden*, 1987, ISBN 3-921694-65-5

66 Kobus, Helmut (Hrsg.): *Modellierung des großräumigen Wärme- und Schadstofftransports im Grundwasser*, Tätigkeitsbericht 1986/87 (DFG-Forschergruppe an den Universitäten Hohenheim, Karlsruhe und Stuttgart) 1987, ISBN 3-921694-66-3

67 Söll, Thomas: *Berechnungsverfahren zur Abschätzung anthropogener Temperaturanomalien im Grundwasser*, 1988, ISBN 3-921694-67-1

68 Dittrich, Andreas; Westrich, Bernd: *Bodenseeufererosion, Bestandsaufnahme und Bewertung*, 1988, ISBN 3-921694-68-X, vergriffen

69 Huwe, Bernd; van der Ploeg, Rienk R.: *Modelle zur Simulation des Stickstoffhaushaltes von Standorten mit unterschiedlicher landwirtschaftlicher Nutzung*, 1988, ISBN 3-921694-69-8, vergriffen

70 Stephan, Karl: *Integration elliptischer Funktionen*, 1988, ISBN 3-921694-70-1

71 Kobus, Helmut; Zilliox, Lothaire (Hrsg.): *Nitratbelastung des Grundwassers, Auswirkungen der Landwirtschaft auf die Grundwasser- und Rohwasserbeschaffenheit und Maßnahmen zum Schutz des Grundwassers*. Vorträge des deutsch-französischen Kolloquiums am 6. Oktober 1988, Universitäten Stuttgart und Louis Pasteur Strasbourg (Vorträge in deutsch oder französisch, Kurzfassungen zweisprachig), 1988, ISBN 3-921694-71-X

72 Soyeaux, Renald: *Unterströmung von Stauanlagen auf klüftigem Untergrund unter Berücksichtigung laminarer und turbulenter Fließzustände*,1991, ISBN 3-921694-72-8

73 Kohane, Roberto: *Berechnungsmethoden für Hochwasserabfluß in Fließgewässern mit überströmten Vorländern*, 1991, ISBN 3-921694-73-6

74 Hassinger, Reinhard: *Beitrag zur Hydraulik und Bemessung von Blocksteinrampen in flexibler Bauweise*, 1991, ISBN 3-921694-74-4, vergriffen

75 Schäfer, Gerhard: *Einfluß von Schichtenstrukturen und lokalen Einlagerungen auf die Längsdispersion in Porengrundwasserleitern*, 1991, ISBN 3-921694-75-2

76 Giesecke, Jürgen: *Vorträge, Wasserwirtschaft in stark besiedelten Regionen; Umweltforschung mit Schwerpunkt Wasserwirtschaft*, 1991, ISBN 3-921694-76-0

77 Huwe, Bernd: *Deterministische und stochastische Ansätze zur Modellierung des Stickstoffhaushalts landwirtschaftlich genutzter Flächen auf unterschiedlichem Skalenniveau*, 1992, ISBN 3-921694-77-9, vergriffen

78 Rommel, Michael: *Verwendung von Kluftdaten zur realitätsnahen Generierung von Kluftnetzen mit anschließender laminar-turbulenter Strömungsberechnung*, 1993, ISBN 3-92 1694-78-7

79 Marschall, Paul: *Die Ermittlung lokaler Stofffrachten im Grundwasser mit Hilfe von Einbohrloch-Meßverfahren*, 1993, ISBN 3-921694-79-5, vergriffen

80 Ptak, Thomas: *Stofftransport in heterogenen Porenaquiferen: Felduntersuchungen und stochastische Modellierung*, 1993, ISBN 3-921694-80-9, vergriffen

81 Haakh, Frieder: *Transientes Strömungsverhalten in Wirbelkammern,* 1993, ISBN 3-921694-81-7

82 Kobus, Helmut; Cirpka, Olaf; Barczewski, Baldur; Koschitzky, Hans-Peter: *Versucheinrichtung zur Grundwasser und Altlastensanierung VEGAS, Konzeption und Programmrahmen*, 1993, ISBN 3-921694-82-5

83 Zang, Weidong: *Optimaler Echtzeit-Betrieb eines Speichers mit aktueller Abflußregenerierung*, 1994, ISBN 3-921694-83-3, vergriffen

84 Franke, Hans-Jörg: *Stochastische Modellierung eines flächenhaften Stoffeintrages und Transports in Grundwasser am Beispiel der Pflanzenschutzmittelproblematik*, 1995, ISBN 3-921694-84-1

85 Lang, Ulrich: *Simulation regionaler Strömungs- und Transportvorgänge in Karstaquiferen mit Hilfe des Doppelkontinuum-Ansatzes: Methodenentwicklung und Parameteridentifikation*, 1995, ISBN 3-921694-85-X, vergriffen

86 Helmig, Rainer: *Einführung in die Numerischen Methoden der Hydromechanik*, 1996, ISBN 3-921694-86-8, vergriffen

87 Cirpka, Olaf: *CONTRACT: A Numerical Tool for Contaminant Transport and Chemical Transformations - Theory and Program Documentation* -, 1996, ISBN 3-921694-87-6

88 Haberlandt, Uwe: *Stochastische Synthese und Regionalisierung des Niederschlages für Schmutzfrachtberechnungen*, 1996, ISBN 3-921694-88-4

89 Croisé, Jean: *Extraktion von flüchtigen Chemikalien aus natürlichen Lockergesteinen mittels erzwungener Luftströmung*, 1996, ISBN 3-921694-89-2, vergriffen

90 Jorde, Klaus: *Ökologisch begründete, dynamische Mindestwasserregelungen bei Ausleitungskraftwerken*, 1997, ISBN 3-921694-90-6, vergriffen

91 Helmig, Rainer: *Gekoppelte Strömungs- und Transportprozesse im Untergrund - Ein Beitrag zur Hydrosystemmodellierung*-, 1998, ISBN 3-921694-91-4, vergriffen

92 Emmert, Martin: *Numerische Modellierung nichtisothermer Gas-Wasser Systeme in porösen Medien,* 1997, ISBN 3-921694-92-2

93 Kern, Ulrich: *Transport von Schweb- und Schadstoffen in staugeregelten Fließgewässern am Beispiel des Neckars*, 1997, ISBN 3-921694-93-0, vergriffen

94 Förster, Georg: *Druckstoßdämpfung durch große Luftblasen in Hochpunkten von Rohrleitungen 1997*, ISBN 3-921694-94-9

95 Cirpka, Olaf: *Numerische Methoden zur Simulation des reaktiven Mehrkomponententransports im Grundwasser*, 1997, ISBN 3-921694-95-7, vergriffen

96 Färber, Arne: *Wärmetransport in der ungesättigten Bodenzone: Entwicklung einer thermischen In-situ-Sanierungstechnologie*, 1997, ISBN 3-921694-96-5

97 Betz, Christoph: *Wasserdampfdestillation von Schadstoffen im porösen Medium: Entwicklung einer thermischen In-situ-Sanierungstechnologie*, 1998, ISBN 3-921694-97-3

98 Xu, Yichun: *Numerical Modeling of Suspended Sediment Transport in Rivers*, 1998, ISBN 3-921694-98-1, vergriffen

99 Wüst, Wolfgang: *Geochemische Untersuchungen zur Sanierung CKW-kontaminierter Aquifere mit Fe(0)-Reaktionswänden,* 2000, ISBN 3-933761-02-2

100 Sheta, Hussam: *Simulation von Mehrphasenvorgängen in porösen Medien unter Einbeziehung von Hysterese-Effekten*, 2000, ISBN 3-933761-03-4

101 Ayros, Edwin: *Regionalisierung extremer Abflüsse auf der Grundlage statistischer Verfahren*, 2000, ISBN 3-933761-04-2, vergriffen

102 Huber, Ralf: *Compositional Multiphase Flow and Transport in Heterogeneous Porous Media*, 2000, ISBN 3-933761-05-0

103 Braun, Christopherus: *Ein Upscaling-Verfahren für Mehrphasenströmungen in porösen Medien*, 2000, ISBN 3-933761-06-9

104 Hofmann, Bernd: *Entwicklung eines rechnergestützten Managementsystems zur Beurteilung von Grundwasserschadensfällen*, 2000, ISBN 3-933761-07-7

105 Class, Holger: *Theorie und numerische Modellierung nichtisothermer Mehrphasenprozesse in NAPL-kontaminierten porösen Medien,* 2001, ISBN 3-933761-08-5

106 Schmidt, Reinhard: *Wasserdampf- und Heißluftinjektion zur thermischen Sanierung kontaminierter Standorte*, 2001, ISBN 3-933761-09-3

107 Josef, Reinhold:, *Schadstoffextraktion mit hydraulischen Sanierungsverfahren unter Anwendung von grenzflächenaktiven Stoffen*, 2001, ISBN 3-933761-10-7

108 Schneider, Matthias: *Habitat- und Abflussmodellierung für Fließgewässer mit unscharfen Berechnungsansätzen*, 2001, ISBN 3-933761-11-5

109 Rathgeb, Andreas: *Hydrodynamische Bemessungsgrundlagen für Lockerdeckwerke an überströmbaren Erddämmen*, 2001, ISBN 3-933761-12-3

110 Lang, Stefan: *Parallele numerische Simulation instätionärer Probleme mit adaptiven Methoden auf unstrukturierten Gittern*, 2001, ISBN 3-933761-13-1

111 Appt, Jochen; Stumpp Simone: *Die Bodensee-Messkampagne 2001, IWS/CWR Lake Constance Measurement Program 2001*, 2002, ISBN 3-933761-14-X

112 Heimerl, Stephan: *Systematische Beurteilung von Wasserkraftprojekten,* 2002, ISBN 3-933761-15-8, vergriffen

113 Iqbal, Amin: *On the Management and Salinity Control of Drip Irrigation,* 2002, ISBN 3-933761-16-6

114 Silberhorn-Hemminger, Annette: *Modellierung von Kluftaquifersystemen: Geostatistische Analyse und deterministisch-stochastische Kluftgenerierung,* 2002, ISBN 3-933761-17-4

115 Winkler, Angela: *Prozesse des Wärme- und Stofftransports bei der In-situ-Sanierung mit festen Wärmequellen,* 2003, ISBN 3-933761-18-2

116 Marx, Walter: *Wasserkraft, Bewässerung, Umwelt - Planungs- und Bewertungsschwerpunkte der Wasserbewirtschaftung,* 2003, ISBN 3-933761-19-0

117 Hinkelmann, Reinhard: *Efficient Numerical Methods and Information-Processing Techniques in Environment Water,* 2003, ISBN 3-933761-20-4

118 Samaniego-Eguiguren, Luis Eduardo: *Hydrological Consequences of Land Use / Land Cover and Climatic Changes in Mesoscale Catchments*, 2003, ISBN 3-933761-21-2

119 Neunhäuserer, Lina: *Diskretisierungsansätze zur Modellierung von Strömungs- und Transportprozessen in geklüftet-porösen Medien*, 2003, ISBN 3-933761-22-0

120 Paul, Maren: *Simulation of Two-Phase Flow in Heterogeneous Poros Media with Adaptive Methods*, 2003, ISBN 3-933761-23-9

121 Ehret, Uwe: *Rainfall and Flood Nowcasting in Small Catchments using Weather Radar*, 2003, ISBN 3-933761-24-7

122 Haag, Ingo: *Der Sauerstoffhaushalt staugeregelter Flüsse am Beispiel des Neckars - Analysen, Experimente, Simulationen -,* 2003, ISBN 3-933761-25-5

123 Appt, Jochen: *Analysis of Basin-Scale Internal Waves in Upper Lake Constance,* 2003, ISBN 3-933761-26-3

124 Hrsg.: Schrenk, Volker; Batereau, Katrin; Barczewski, Baldur; Weber, Karolin und Koschitzky, Hans-Peter: *Symposium Ressource Fläche und VEGAS - Statuskolloquium 2003, 30. September und 1. Oktober 2003,* 2003, ISBN 3-933761-27-1

125 Omar Khalil Ouda: *Optimisation of Agricultural Water Use: A Decision Support System for the Gaza Strip,* 2003, ISBN 3-933761-28-0

126 Batereau, Katrin: *Sensorbasierte Bodenluftmessung zur Vor-Ort-Erkundung von Schadensherden im Untergrund*, 2004, ISBN 3-933761-29-8

127 Witt, Oliver: *Erosionsstabilität von Gewässersedimenten mit Auswirkung auf den Stofftransport bei Hochwasser am Beispiel ausgewählter Stauhaltungen des Oberrheins*, 2004, ISBN 3-933761-30-1

128 Jakobs, Hartmut: *Simulation nicht-isothermer Gas-Wasser-Prozesse in komplexen Kluft-Matrix-Systemen*, 2004, ISBN 3-933761-31-X

129 Li, Chen-Chien: *Deterministisch-stochastisches Berechnungskonzept zur Beurteilung der Auswirkungen erosiver Hochwasserereignisse in Flussstauhaltungen,* 2004, ISBN 3-933761-32-8

130 Reichenberger, Volker; Helmig, Rainer; Jakobs, Hartmut; Bastian, Peter; Niessner, Jennifer: *Complex Gas-Water Processes in Discrete Fracture-Matrix Systems: Upscaling, Mass-Conservative Discretization and Efficient Multilevel Solution,* 2004, ISBN 3-933761-33-6

131 Hrsg.: Barczewski, Baldur; Koschitzky, Hans-Peter; Weber, Karolin; Wege, Ralf: *VEGAS - Statuskolloquium 2004,* Tagungsband zur Veranstaltung am 05. Oktober 2004 an der Universität Stuttgart, Campus Stuttgart-Vaihingen, 2004, ISBN 3-933761-34-4

132 Asie, Kemal Jabir: *Finite Volume Models for Multiphase Multicomponent Flow through Porous Media*. 2005, ISBN 3-933761-35-2

133 Jacoub, George: *Development of a 2-D Numerical Module for Particulate Contaminant Transport in Flood Retention Reservoirs and Impounded Rivers,* 2004, ISBN 3-933761-36-0

134 Nowak, Wolfgang: *Geostatistical Methods for the Identification of Flow and Transport Parameters in the Subsurface,* 2005, ISBN 3-933761-37-9

135 Süß, Mia: *Analysis of the influence of structures and boundaries on flow and transport processes in fractured porous media*, 2005, ISBN 3-933761-38-7

136 Jose, Surabhin Chackiath: *Experimental Investigations on Longitudinal Dispersive Mixing in Heterogeneous Aquifers,* 2005, ISBN: 3-933761-39-5

137 Filiz, Fulya: *Linking Large-Scale Meteorological Conditions to Floods in Mesoscale Catchments,* 2005, ISBN 3-933761-40-9

138 Qin, Minghao: *Wirklichkeitsnahe und recheneffiziente Ermittlung von Temperatur und Spannungen bei großen RCC-Staumauern*, 2005, ISBN 3-933761-41-7

139 Kobayashi, Kenichiro: *Optimization Methods for Multiphase Systems in the Subsurface - Application to Methane Migration in Coal Mining Areas*, 2005, ISBN 3-933761-42-5

140 Rahman, Md. Arifur: *Experimental Investigations on Transverse Dispersive Mixing in Heterogeneous Porous Media,* 2005, ISBN 3-933761-43-3

141 Schrenk, Volker: *Ökobilanzen zur Bewertung von Altlastensanierungsmaßnahmen,* 2005, ISBN 3-933761-44-1

142 Hundecha, Hirpa Yeshewatesfa: *Regionalization of Parameters of a Conceptual Rainfall-Runoff Model*, 2005, ISBN: 3-933761-45-X

143 Wege, Ralf: *Untersuchungs- und Überwachungsmethoden für die Beurteilung natürlicher Selbstreinigungsprozesse im Grundwasser,* 2005, ISBN 3-933761-46-8

144 Breiting, Thomas: *Techniken und Methoden der Hydroinformatik - Modellierung von komplexen Hydrosystemen im Untergrund*, 2006, 3-933761-47-6

145 Hrsg.: Braun, Jürgen; Koschitzky, Hans-Peter; Müller, Martin: *Ressource Untergrund: 10 Jahre VEGAS: Forschung und Technologieentwicklung zum Schutz von Grundwasser und Boden,* Tagungsband zur Veranstaltung am 28. und 29. September 2005 an der Universität Stuttgart, Campus Stuttgart-Vaihingen, 2005, ISBN 3-933761-48-4

146 Rojanschi, Vlad: *Abflusskonzentration in mesoskaligen Einzugsgebieten unter Berücksichtigung des Sickerraumes,* 2006, ISBN 3-933761-49-2

147 Winkler, Nina Simone: *Optimierung der Steuerung von Hochwasserrückhaltebecken-systemen,* 2006, ISBN 3-933761-50-6

148 Wolf, Jens: *Räumlich differenzierte Modellierung der Grundwasserströmung alluvialer Aquifere für mesoskalige Einzugsgebiete*, 2006, ISBN: 3-933761-51-4

149 Kohler, Beate: *Externe Effekte der Laufwasserkraftnutzung*, 2006, ISBN 3-933761-52-2

150 Hrsg.: Braun, Jürgen; Koschitzky, Hans-Peter; Stuhrmann, Matthias: *VEGAS-Statuskolloquium 2006,* Tagungsband zur Veranstaltung am 28. September 2006 an der Universität Stuttgart, Campus Stuttgart-Vaihingen, 2006, ISBN 3-933761-53-0

151 Niessner, Jennifer: *Multi-Scale Modeling of Multi-Phase - Multi-Component Processes in Heterogeneous Porous Media*, 2006, ISBN 3-933761-54-9

152 Fischer, Markus: *Beanspruchung eingeerdeter Rohrleitungen infolge Austrocknung bindiger Böden,* 2006, ISBN 3-933761-55-7

153 Schneck, Alexander: *Optimierung der Grundwasserbewirtschaftung unter Berücksichtigung der Belange der Wasserversorgung, der Landwirtschaft und des Naturschutzes*, 2006, ISBN 3-933761-56-5

154 Das, Tapash: *The Impact of Spatial Variability of Precipitation on the Predictive Uncertainty of Hydrological Models,* 2006, ISBN 3-933761-57-3

155 Bielinski, Andreas: *Numerical Simulation of CO_2 sequestration in geological formations*, 2007, ISBN 3-933761-58-1

156 Mödinger, Jens: *Entwicklung eines Bewertungs- und Entscheidungsunterstützungssystems für eine nachhaltige regionale Grundwasserbewirtschaftung*, 2006, ISBN 3-933761-60-3

157 Manthey, Sabine: *Two-phase flow processes with dynamic effects in porous media - parameter estimation and simulation,* 2007, ISBN 3-933761-61-1

158 Pozos Estrada, Oscar: *Investigation on the Effects of Entrained Air in Pipelines,* 2007, ISBN 3-933761-62-X

159 Ochs, Steffen Oliver: *Steam injection into saturated porous media – process analysis including experimental and numerical investigations*, 2007, ISBN 3-933761-63-8

160 Marx, Andreas: *Einsatz gekoppelter Modelle und Wetterradar zur Abschätzung von Niederschlagsintensitäten und zur Abflussvorhersage, 2007,* ISBN 3-933761-64-6

161 Hartmann, Gabriele Maria: *Investigation of Evapotranspiration Concepts in Hydrological Modelling for Climate Change Impact Assessment*, 2007, ISBN 3-933761-65-4

162 Kebede Gurmessa, Tesfaye: *Numerical Investigation on Flow and Transport Characteristics to Improve Long-Term Simulation of Reservoir Sedimentation*, 2007, ISBN 3-933761-66-2

163 Trifković, Aleksandar: *Multi-objective and Risk-based Modelling Methodology for Planning, Design and Operation of Water Supply Systems*, 2007, ISBN 3-933761-67-0

164 Götzinger, Jens: *Distributed Conceptual Hydrological Modelling - Simulation of Climate, Land Use Change Impact and Uncertainty Analysis*, 2007, ISBN 3-933761-68-9

165 Hrsg.: Braun, Jürgen; Koschitzky, Hans-Peter; Stuhrmann, Matthias: *VEGAS – Kolloquium 2007,* Tagungsband zur Veranstaltung am 26. September 2007 an der Universität Stuttgart, Campus Stuttgart-Vaihingen, 2007, ISBN 3-933761-69-7

166 Freeman, Beau: *Modernization Criteria Assessment for Water Resources Planning; Klamath Irrigation Project, U.S.*, 2008, ISBN 3-933761-70-0

167 Dreher, Thomas: *Selektive Sedimentation von Feinstschwebstoffen in Wechselwirkung mit wandnahen turbulenten Strömungsbedingungen*, 2008, ISBN 3-933761-71-9

168 Yang, Wei: *Discrete-Continuous Downscaling Model for Generating Daily Precipitation Time Series*, 2008, ISBN 3-933761-72-7

169 Kopecki, Ianina: *Calculational Approach to FST-Hemispheres for Multiparametrical Benthos Habitat Modelling,* 2008*,* ISBN 3-933761-73-5

170 Brommundt, Jürgen: *Stochastische Generierung räumlich zusammenhängender Niederschlagszeitreihen*, 2008, ISBN 3-933761-74-3

171 Papafotiou, *Alexandros: Numerical Investigations of the Role of Hysteresis in Heterogeneous Two-Phase Flow Systems*, 2008, ISBN 3-933761-75-1

172 He, Yi: *Application of a Non-Parametric Classification Scheme to Catchment Hydrology*, 2008, ISBN 978-3-933761-76-7

173 Wagner, Sven: *Water Balance in a Poorly Gauged Basin in West Africa Using Atmospheric Modelling and Remote Sensing Information*, 2008, ISBN 978-3-933761-77-4

174 Hrsg.: Braun, Jürgen; Koschitzky, Hans-Peter; Stuhrmann, Matthias; Schrenk, Volker: *VEGAS-Kolloquium 2008 Ressource Fläche III*, Tagungsband zur Veranstaltung am 01. Oktober 2008 an der Universität Stuttgart, Campus Stuttgart-Vaihingen, 2008, ISBN 978-3-933761-78-1

175 Patil, Sachin: *Regionalization of an Event Based Nash Cascade Model for Flood Predictions in Ungauged Basins*, 2008, ISBN 978-3-933761-79-8

176 Assteerawatt, Anongnart: *Flow and Transport Modelling of Fractured Aquifers based on a Geostatistical Approach,* 2008, ISBN 978-3-933761-80-4

177 Karnahl, Joachim Alexander: *2D numerische Modellierung von multifraktionalem Schwebstoff- und Schadstofftransport in Flüssen*, 2008, ISBN 978-3-933761-81-1

178 Hiester, Uwe: *Technologieentwicklung zur In-situ-Sanierung der ungesättigten Bodenzone mit festen Wärmequellen,* 2009, ISBN 978-3-933761-82-8

179 Laux, Patrick: *Statistical Modeling of Precipitation for Agricultural Planning in the Volta Basin of West Africa,* 2009, ISBN 978-3-933761-83-5

180 Ehsan, Saqib: *Evaluation of Life Safety Risks Related to Severe Flooding,* 2009, ISBN 978-3-933761-84-2

181 Prohaska, Sandra: *Development and Application of a 1D Multi-Strip Fine Sediment Transport Model for Regulated Rivers,* 2009, ISBN 978-3-933761-85-9

182 Kopp, Andreas: *Evaluation of CO_2 Injection Processes in Geological Formations for Site Screening,* 2009, ISBN 978-3-933761-86-6

183 Ebigbo, Anozie: *Modelling of biofilm growth and its influence on CO_2 and water (two-phase) flow in porous media,* 2009, ISBN 978-3-933761-87-3

184 Freiboth, Sandra: *A phenomenological model for the numerical simulation of multiphase multicomponent processes considering structural alterations of porous media*, 2009, ISBN 978-3-933761-88-0

185 Zöllner, Frank: *Implementierung und Anwendung netzfreier Methoden im Konstruktiven Wasserbau und in der Hydromechanik*, 2009, ISBN 978-3-933761-89-7

186 Vasin, Milos: *Influence of the soil structure and property contrast on flow and transport in the unsaturated zone*, 2010, ISBN 978-3-933761-90-3

187 Li, Jing: *Application of Copulas as a New Geostatistical Tool*, 2010, ISBN 978-3-933761-91-0

188 AghaKouchak, Amir: *Simulation of Remotely Sensed Rainfall Fields Using Copulas*, 2010, ISBN 978-3-933761-92-7

189 Thapa, Pawan Kumar: *Physically-based spatially distributed rainfall runoff modelling for soil erosion estimation*, 2010, ISBN 978-3-933761-93-4

190 Wurms, Sven: *Numerische Modellierung der Sedimentationsprozesse in Retentionsanlagen zur Steuerung von Stoffströmen bei extremen Hochwasserabflussereignissen*, 2011, ISBN 978-3-933761-94-1

191 Merkel, Uwe: *Unsicherheitsanalyse hydraulischer Einwirkungen auf Hochwasserschutzdeiche und Steigerung der Leistungsfähigkeit durch adaptive Strömungsmodellierung*, 2011, ISBN 978-3-933761-95-8

192 Fritz, Jochen: *A Decoupled Model for Compositional Non-Isothermal Multiphase Flow in Porous Media and Multiphysics Approaches for Two-Phase Flow*, 2010, ISBN 978-3-933761-96-5

193 Weber, Karolin (Hrsg.): *12. Treffen junger WissenschaftlerInnen an Wasserbauinstituten*, 2010, ISBN 978-3-933761-97-2

194 Bliefernicht, Jan-Geert: *Probability Forecasts of Daily Areal Precipitation for Small River Basins,* 2011, ISBN 978-3-933761-98-9

195 Hrsg.: Koschitzky, Hans-Peter; Braun, Jürgen: *VEGAS-Kolloquium 2010 In-situ-Sanierung - Stand und Entwicklung Nano und ISCO -,* Tagungsband zur Veranstaltung am 07. Oktober 2010 an der Universität Stuttgart, Campus Stuttgart-Vaihingen*,* 2010*,* ISBN 978-3-933761-99-6

196 Gafurov, Abror: *Water Balance Modeling Using Remote Sensing Information - Focus on Central Asia,* 2010, ISBN 978-3-942036-00-9

197 Mackenberg, Sylvia: *Die Quellstärke in der Sickerwasserprognose: Möglichkeiten und Grenzen von Labor- und Freilanduntersuchungen,* 2010, ISBN 978-3-942036-01-6

198 Singh, Shailesh Kumar: *Robust Parameter Estimation in Gauged and Ungauged Basins,* 2010, ISBN 978-3-942036-02-3

199 Doğan, Mehmet Onur: *Coupling of porous media flow with pipe flow,* 2011, ISBN 978-3-942036-03-0

200 Liu, Min: *Study of Topographic Effects on Hydrological Patterns and the Implication on Hydrological Modeling and Data Interpolation,* 2011, ISBN 978-3-942036-04-7

201 Geleta, Habtamu Itefa: *Watershed Sediment Yield Modeling for Data Scarce Areas,* 2011, ISBN 978-3-942036-05-4

202 Franke, Jörg: *Einfluss der Überwachung auf die Versagenswahrscheinlichkeit von Staustufen,* 2011, ISBN 978-3-942036-06-1

203 Bakimchandra, Oinam: *Integrated Fuzzy-GIS approach for assessing regional soil erosion risks,* 2011, ISBN 978-3-942036-07-8

204 Alam, Muhammad Mahboob: *Statistical Downscaling of Extremes of Precipitation in Mesoscale Catchments from Different RCMs and Their Effects on Local Hydrology,* 2011, ISBN 978-3-942036-08-5

205 Hrsg.: Koschitzky, Hans-Peter; Braun, Jürgen: *VEGAS-Kolloquium 2011 Flache Geothermie - Perspektiven und Risiken,* Tagungsband zur Veranstaltung am 06. Oktober 2011 an der Universität Stuttgart, Campus Stuttgart-Vaihingen, 2011, ISBN 978-3-933761-09-2

206 Haslauer, Claus: *Analysis of Real-World Spatial Dependence of Subsurface Hydraulic Properties Using Copulas with a Focus on Solute Transport Behaviour,* 2011, ISBN 978-3-942036-10-8

207 Dung, Nguyen Viet: *Multi-objective automatic calibration of hydrodynamic models – development of the concept and an application in the Mekong Delta,* 2011, ISBN 978-3-942036-11-5

208 Hung, Nguyen Nghia: *Sediment dynamics in the floodplain of the Mekong Delta, Vietnam,* 2011, ISBN 978-3-942036-12-2

209 Kuhlmann, Anna: *Influence of soil structure and root water uptake on flow in the unsaturated zone,* 2012, ISBN 978-3-942036-13-9

210 Tuhtan, Jeffrey Andrew: *Including the Second Law Inequality in Aquatic Ecodynamics: A Modeling Approach for Alpine Rivers Impacted by Hydropeaking,* 2012, ISBN 978-3-942036-14-6

211 Tolossa, Habtamu: *Sediment Transport Computation Using a Data-Driven Adaptive Neuro-Fuzzy Modelling Approach,* 2012, ISBN 978-3-942036-15-3

212 Tatomir, Alexandru-Bodgan: *From Discrete to Continuum Concepts of Flow in Fractured Porous Media,* 2012, ISBN 978-3-942036-16-0

213 Erbertseder, Karin: *A Multi-Scale Model for Describing Cancer-Therapeutic Transport in the Human Lung,* 2012, ISBN 978-3-942036-17-7

214 Noack, Markus: *Modelling Approach for Interstitial Sediment Dynamics and Reproduction of Gravel Spawning Fish,* 2012, ISBN 978-3-942036-18-4

215 De Boer, Cjestmir Volkert: *Transport of Nano Sized Zero Valent Iron Colloids during Injection into the Subsurface*, 2012, ISBN 978-3-942036-19-1

216 Pfaff, Thomas: *Processing and Analysis of Weather Radar Data for Use in Hydrology*, 2013, ISBN 978-3-942036-20-7

Die Mitteilungshefte ab der Nr. 134 (Jg. 2005) stehen als pdf-Datei über die Homepage des Instituts: www.iws.uni-stuttgart.de zur Verfügung.